NEW BIOSENSOR APPLICATIONS OF SURFACE PLASMON AND HYDROGEL OPTICAL WAVEGUIDE SPECTROSCOPY

Dissertation
zur Erlangung des Grades
'Doktor der Naturwissenschaft'

am Fachbereich Biologie
der Johannes Gutenberg-Universität
in Mainz

Yi Wang
geb. in Zhejiang, V. R. China

Mainz, November, 2010

Abstract

Rapid and sensitive detection of chemical and biological analytes becomes increasingly important in areas such as medical diagnostics, food control and environmental monitoring. Optical biosensors based on surface plasmon resonance (SPR) and optical waveguide spectroscopy have been extensively pushed forward in these fields. In this study, we combine SPR, surface plasmon-enhanced fluorescence spectroscopy (SPFS) and optical waveguide spectroscopy with hydrogel thin film for highly sensitive detection of molecular analytes.

A novel biosensor based on SPFS which was advanced through the excitation of long range surface plasmons (LRSPs) is reported in this study. LRSPs are special surface plasmon waves propagating along thin metal films with orders of magnitude higher electromagnetic field intensity and lower damping than conventional SPs. Therefore, their excitation on the sensor surface provides further increased fluorescence signal. An inhibition immunoassay based on LRSP-enhanced fluorescence spectroscopy (LRSP-FS) was developed for the detection of aflatoxin M_1 (AFM_1) in milk. The biosensor allowed for the detection of AFM_1 in milk at concentrations as low as 0.6 pg mL^{-1}, which is about two orders of magnitude lower than the maximum AFM_1 residue level in milk stipulated by the European Commission legislation.

In addition, LRSPs probe the medium adjacent to the metallic surface with more extended evanescent field than regular SPs. Therefore, three-dimensional binding matrices with up to micrometer thickness have been proposed for the immobilization of biomolecular recognition elements with large surface density that allows to exploit the whole evanescent field of LRSP. A photocrosslinkable carboxymethyl dextran (PCDM) hydrogel thin film is used as a binding matrix, and it is applied for the detection of free prostate specific antigen (f-PSA) based on the LRSP-FS and sandwich immunoassay. We show that this approach allows for the detection of f-PSA at low femto-molar range, which is approximately four orders of magnitude lower than that for direct detection of f-PSA based on the monitoring of binding-induced refractive index changes.

However, a three dimensional hydrogel binding matrix with micrometer thickness can also serve as an optical waveguide. Based on the measurement of binding-induced refractive index changes, a hydrogel optical waveguide spectroscopy (HOWS) is reported for a label-free biosensor. This biosensor is implemented by using a SPR optical setup in which a carboxylated poly(*N*-isoproprylacrylamide) (PNIPAAm) hydrogel film is attached on a metallic surface and modified by protein catcher molecules. Compared to regular SPR biosensor with thiol self-assembled monolayer (SAM), HOWS provides an order of magnitude improved resolution in the refractive index measurements and enlarged binding capacity owing to its low damping and large swelling ratio, respectively. A model immunoassay experiment revealed that HOWS allowed detection of IgG molecules with a 10 pM limit of detection (LOD) that was five-fold lower than that achieved for SPR with thiol SAM. For the high capacity hydrogel matrix, the affinity binding was mass transport limited.

The mass transport of target molecules to the sensor surface can play as critical a role as the chemical reaction itself. In order to overcome the diffusion-limited mass transfer, magnetic iron oxide nanoparticles were employed. The magnetic nanoparticles (MNPs) can serve both as labels providing enhancement of the refractive index changes, and

“vehicles” for rapidly delivering the analytes from sample solution to an SPR sensor surface with a gradient magnetic field. A model sandwich assay for the detection of β human chorionic gonadotropin (βhCG) has been utilized on a gold sensor surface with metallic diffraction grating structure supporting the excitation of SPs. Various detection formats including a) direct detection, b) sandwich assay, c) MNPs immunoassay without and d) with applied magnetic field were compared. The results show that the highly-sensitive MNPs immunoassay improves the LOD on the detection of βhCG by a factor of 5 orders of magnitude with respect to the direct detection.

Contents

Abbreviations

2D	two-dimensional
3D	three-dimensional
AFM_1	aflatoxin M_1
AFM	atomic force microscopy
ATR	attenuated total reflection
CMD	carboxymethylated dextran
βhCG	β human chorionic gonadotropin
BRE	biomolecular recognition elements
BSA	bovine serum albumin
DMF	Dimethylformamide
DMSO	Dimethylsulfoxid
EDC	1-(3-dimethylaminopropyl)-3-ethylcarbodiimide hydrochloride
ELISA	enzyme-linked immunosorbent assay
f-PSA	free prostate specific antigen
HeNe	Helium-Neon
HOW(S)	hydrogel optical waveguide (spectroscopy)
HPLC	high-performance liquid chromatography
HW	hydrogel-guided waves
IgG	immunoglobulin
LOD	limit of detection
LRSP	long range surface plasmon
LRSP-FS	long range surface plasmon-enhanced fluorescence spectroscopy
MHDA	Mercaptohexadecanoic acid
MNP(s)	Magnetic nanoparticle(s)
MNP-abs	magnetic nanoparticle-antibodies
MRI	magnetic resonance imaging
MUTEG	(11-Mercaptoundecyl)tri(ethylene glycol)
NHS	*N*-hydroxysuccinimide
OWS	optical waveguide spectroscopy
PBS	Phosphate buffered saline

PBST	PBS buffer added with Tween 20
PCMD	photo-crosslinkable carboxymethylated dextran
PDMS	Polydimethylsiloxane
PEG	poly(ethylene glycol)
PNIPAAm	poly(*N*-isoproprylacrylamide)
PMT	Photomultiplier tube
SAM	self-assembled monolayer
SP, SPR	surface plasmon (resonance)
SRSP	short range surface plasmon
SPFS	surface plasmon resonance-enhanced fluorescence spectroscopy
TE	transversal electric
TFPS	Sodium *para*-tetrafluorophenol-sulfonate
TIR	total internal reflection
TLC	thin-layer chromatography
TM	transversal magnetic
TSTU	*N*,*N*,*N*',*N*'-Tetramethyl-*O*-(*N*-succinimidyl)uronium tetrafluoroborate

Chapter 1 Introduction

1.1 Biosensors

A biosensor is an analytical device for the detection of an analyte that combines a biological component with a physicochemical detector component. It consists of three parts (Figure 1.1):

(a) the biological recognition elements (BRE) that specifically interact with target analyte, which are typically biological materials, such as enzymes, antibodies, nucleic acids, cell receptors, organelles, tissue and whole cells, or biomimic materials.

(b) the transducer that transforms the interactions of BRE with analyte into a measureable electrochemical, optical, thermometric, piezoelectric or magnetic signal.

(c) the signal output system that is primarily responsible for the processing and display of sensor output.

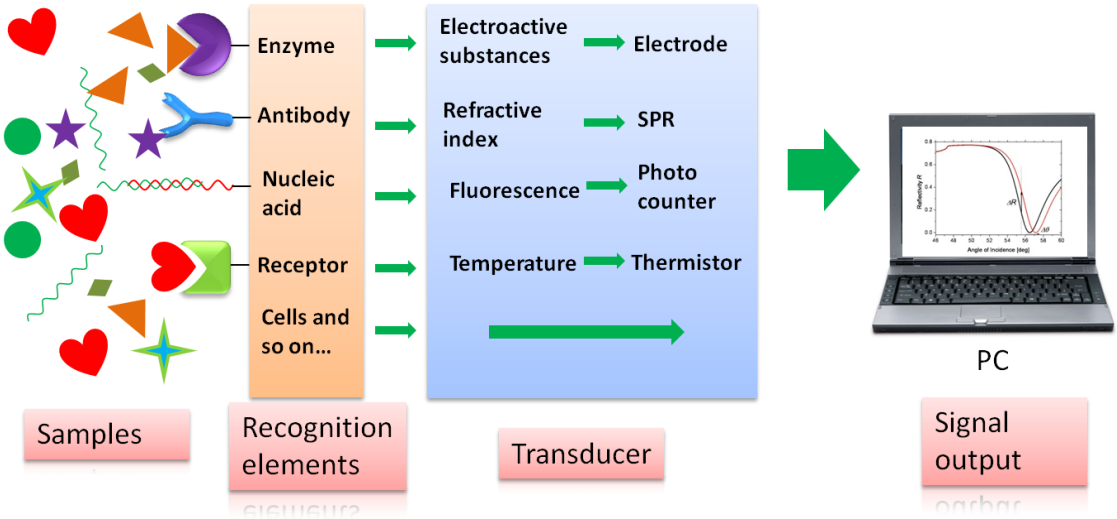

Figure 1.1 Schematic representation of the principle of biosensors

The most usual format of a biosensor is that of a biological recognition elements immobilized on the surface of a transducer. Immobilization offers the advantage of: (a) It enables continuous sensing of analytes in flowing systems such as blood, bioreactor fluids,

or water samples. (b) The biosensor can be reusable or regenerable. (c) It offers the possibility for parallel detection of multiple analytes. In this class of (heterogeneous assay-based) biosensors, biointerface is an important part. Thus the surface chemistry is a serious issue. For instance, a nonfouling layer offers great feasibility to minimize nonspecific absorption of molecules from sample solution onto the sensor surface, thus to distinguish the specific signal from the noise and improve the sensitivity and specificity of the biosensors.

Since the first biosensor was introduced by Clarke in 1962[1], biosensor technologies made considerable progress in order to meet needs in various application areas, including food control, environmental monitoring and medical diagnosis. The potential of biosensor technologies to provide high sensitivity, high specificity and miniaturized devices for rapid and cost effective detection of range of important analytes has generated intense commercial interest. Among these biosensors, the mostly used biosensor schemes are based on electrochemical[2-5] and optical transducers[6, 7].

1.2 Optical biosensors

Optical sensor schemes offer the advantages of high sensitivity, real-time monitoring of molecules interactions, and rapid signal readout. Optical sensors probe the analyte interaction with a change in optical properties that can be observed from variations in absorption, reflectance, emission, fluorescence or interference pattern. For instance, the refractometric biosensors including surface plasmon resonance (SPR), grating-coupled integrated optical waveguide [8, 9], spectroscopy of leaky dielectric waveguides (resonant mirror) [10-12] and integrated optical Mach-Zehnder interferometer [13] measures changes in the refractive index due to a capture of target analyte on the sensor surface.

Since the first demonstration of SPR for the observation of processes at the surface of metal and sensing of gases in the early 1980s, SPR sensors have made vast advances in terms of both development of the technology and its applications. SPR biosensor have become a popular technique for monitoring and quantifying bimolecular interactions in real-time. SPR biosensors allow determining affinity binding constant without the need of molecular labeling. The first commercial SPR instrument was released by Biacore (Sweden) in 1990. Since then, development of SPR biosensors for detection of chemical

and biological analytes has gained considerable momentum. The review articles and books focused on SPR biosensor can be found in the references[14, 15].

Surface plasmon-enhanced fluorescence spectroscopy (SPFS) was firstly reported by Attridge et. al. in 1991[16]. It has been reintroduced for the analysis of oligonucleotides, proteins and other biomolecules by Knoll et al. at later 90s[17, 18]. In SPFS, fluorophore-labeled molecules captured on the sensor surface are excited with surface plasmons (SPs) and the emitted fluorescence light is measured. This approach takes advantages of the enhanced intensity of the electromagnetic field occurring upon the resonant excitation of SPs which greatly increases the strength of the fluorescence signal. Accordingly, SPFS has been proved to offer high sensitivity for the detection of proteins at the concentration down to atomolar (aM)[19], and femtomolar for the detection of oligonucleotides[20]. Furthermore, combination SPR and SPFS for simultaneously monitoring the interfacial refractive index changes and the fluorescence variations offers the possibility to characterize the biological activity and the fluorescence emitting efficiency of proteins and biomolecules.

1.3 Aim of this study

This thesis aims at improving the sensitivity of SPR and SPFS-based biosensor technologies through new schemes that take advantages of long range surface plasmon (LRSP) optics, hydrogel materials and magnetic nanoparticles. In particular, hydrogel polymer networks hold potential for design of biosensor surface architectures with large binding capacity that can efficiently capture target analyte on a sensor surface. The probing of molecular binding events occurring on a sensor surface by optical waves such as LRSPs and hydrogel-guided waves offer possibility for increasing the sensitivity as their characteristics can be tuned for specific needs. Furthermore, magnetic nanoparticles are employed in SPR biosensor in order to serve as “vehicles” for manipulating with the analyte on the sensor surface and as a label that enhances the binding-induced refractive index changes. The developed biosensors schemes are pursued for the analysis of analytes in real samples relevant to important areas of food control and medical diagnostics. The thesis is structured into 7 chapters with the following outline. Chapters 3-7 describe key results achieved in this thesis.

Chapter 2 titled “Theory and Background” describes theory of SP, long range-surface plasmon (LRSP) and planar optical waveguide optics. The implementation of these guided waves to surface plasmon resonance (SPR) and surface plasmon-enhanced fluorescence spectroscopy (SPFS) biosensors is discussed, In addition, models used for interfacial molecules interactions, estimation of the LOD of SPR biosensor and an overview of hydrogel binding matrices applied in evanescent wave biosensors are presented.

Chapter 3 titled as “Methods and Sample Preparation” covers experimental methods used in this thesis and all information about general sample preparations. Used optical and instruments and methods are introduced in this chapter. Protocols used for sample preparation including diffraction grating, deposition of thin films, surface modification with self-assembled monolayer (SAM) and hydrogel thin films and protein labeling with chromophore and magnetic nanoparticles are presented.

Chapter 4 “Long Range Surface Plasmon-Enhanced Fluorescence Spectroscopy for the Detection of Aflatoxin M_1 in Milk” presents the development of biosensor based on LRSP combined with SPFS (LR-SPFS) that was applied for detection aflatoxin M_1 in milk by using inhibition immunoassay. The construction of the sensor and its key performance characteristics are described and compared to those of existing technologies for detection of this dangerous toxin in terms of sensitivity and detection time.

In chapter 5 “Dextran Hydrogel Binding Matrix for Biosensors Based on Long Range Surface Plasmon-Enhanced Fluorescence Spectroscopy”, the LRSP-FS detection method was combined with highly swollen dextran matrix and applied for detection of free-prostate specific antigen (f-PSA) in human serum. The characteristics of around micrometer thick photo-crosslinkable dextran hydrogel matrix that is probed with a LRSP mode exhibiting penetration depth in similar range are determined. The implementation of the sensor platform for detection of target analyte by using sandwich immunoassays is presented.

In chapter 6 “Biosensor Based on Hydrogel Optical Waveguide Spectroscopy” deals with a hydrogel thin film (pNIPAAM)-based binding matrix that serves both as an optical waveguide and a binding matrix. The spectroscopy of hydrogel guided waves is employed for biosensing through assay for detection of IgG. The amount of captured

molecules and the limit of detection on hydrogel optical waveguide biosensor are compared with that on regular SPR biosensor with thiol-based SAM.

Chapter 7 "Magnetic Nanoparticle-Enhanced Surface Plasmon Resonance Biosensor" reports on the investigation of (diffusion driven) mass transfer of analyte to the sensor surface and investigate how it can be overcome by using magnetic nanoparticle assays. Particularly, grating-coupled SPR sensor was developed and combined with magnetic nanoparticle which can be collected by a gradient magnetic field applied through the sensor chip. The functionality of magnetic nanoparticles modified with catcher molecules for a) enhancing of the binding-induced refractive index changes on the sensor surface, b) for manipulating of the sensor surface is carried out by using an immunoassay for detection of (β human chorionic gonadotropin) βhCG.

References

1. Clark, L. C., Jr. and Lyons, C. (1962). Electrode systems for continuous monitoring in cardiovascular surgery, *Ann N Y Acad Sci*, **102**, 29-45.
2. Wang, J. (2008). Electrochemical glucose biosensors, *Chemical Reviews*, **108**, 814-825.
3. Wang, J. (2002). Electrochemical nucleic acid biosensors, *Analytica Chimica Acta*, **469**, 63-71.
4. Wang, J. (2005). Carbon-nanotube based electrochemical biosensors: A review, *Electroanalysis*, **17**, 7-14.
5. Grieshaber, D., MacKenzie, R., Voros, J. and Reimhult, E. (2008). Electrochemical biosensors - Sensor principles and architectures, *Sensors*, **8**, 1400-1458.
6. Cooper, M. A. (2002). Optical biosensors in drug discovery, *Nature Reviews Drug Discovery*, **1**, 515-528.
7. Borisov, S. M. and Wolfbeis, O. S. (2008). Optical biosensors, *Chemical Reviews*, **108**, 423-461.
8. Clerc, D. and Lukosz, W. (1997). Direct immunosensing with an integrated-optical output grating coupler, *Sensors and Actuators B-Chemical*, **40**, 53-58.
9. Tiefenthaler, K. and Lukosz, W. (1989). Sensitivity of Grating Couplers as Integrated-Optical Chemical Sensors, *Journal of the Optical Society of America B-Optical Physics*, **6**, 209-220.
10. Buckle, P. E., Davies, R. J., Kinning, T., Yeung, D., Edwards, P. R., Pollardknight, D. and Lowe, C. R. (1993). The Resonant Mirror - a Novel Optical Sensor for Direct Sensing of Biomolecular Interactions .2. Applications, *Biosensors & Bioelectronics*, **8**, 355-363.
11. Skivesen, N., Horvath, R., Thinggaard, S., Larsen, N. B. and Pedersen, H. C. (2007). Deep-probe metal-clad waveguide biosensors, *Biosensors & Bioelectronics*, **22**, 1282-1288.
12. Zourob, M., Mohr, S., Brown, B. J. T., Fielden, P. R., McDonnell, M. B. and Goddard, N. J. (2005). Bacteria detection using disposable optical leaky waveguide sensors, *Biosensors & Bioelectronics*, **21**, 293-302.
13. Heideman, R. G. and Lambeck, P. V. (1999). Remote opto-chemical sensing with

extreme sensitivity: design, fabrication and performance of a pigtailed integrated optical phase-modulated Mach-Zehnder interferometer system, *Sensors and Actuators B-Chemical*, **61**, 100-127.

14. Homola, J. (2003). Present and future of surface plasmon resonance biosensors, *Analytical and Bioanalytical Chemistry*, **377**, 528-539.
15. Homola, J. (2008). Surface plasmon resonance sensors for detection of chemical and biological species, *Chemical Reviews*, **108**, 462-493.
16. Attridge, J. W., Daniels, P. B., Deacon, J. K., Robinson, G. A. and Davidson, G. P. (1991). Sensitivity Enhancement of Optical Immunosensors by the Use of a Surface-Plasmon Resonance Fluoroimmunoassay, *Biosensors & Bioelectronics*, **6**, 201-214.
17. Liebermann, T. and Knoll, W. (2000). Surface-plasmon field-enhanced fluorescence spectroscopy, *Colloid. Surface. A*, **171**, 115-130.
18. Neumann, T., Johansson, M. L., Kambhampati, D. and Knoll, W. (2002). Surface-plasmon fluorescence spectroscopy, *Adv. Funct. Mater.*, **12**, 575-586.
19. Yu, F., Persson, B., Lofas, S. and Knoll, W. (2004). Attomolar sensitivity in bioassays based on surface plasmon fluorescence spectroscopy, *J. Am. Chem. Soc.*, **126**, 8902-8903.
20. Yao, D. F., Yu, F., Kim, J. Y., Scholz, J., Nielsen, P. E., Sinner, E. K. and Knoll, W. (2004). Surface plasmon field-enhanced fluorescence spectroscopy in PCR product analysis by peptide nucleic acid probes, *Nucleic Acids Research*, **32**, -.

Chapter 2 Theory and Background

2.1 Bound electromagnetic modes

2.1.1 Surface plasmons

Surface plasmons (SPs), also known as surface plasmon polaritons, are surface electromagnetic waves that propagate in a direction parallel to the metal/dielectric (or metal/vacuum) interface. The phenomenon has first been observed in 1902, when Wood[1] illuminated a metallic diffraction grating with polychromatic light and noticed narrow dark bands in the spectrum of the diffracted light, which he referred as to anomalies. The theoretical work by Fano elucidated that these anomalies are associated with the excitation of electromagnetic surface waves on the surface of the diffraction grating. Since then, a considerable amount of work by Otto[2], Kretschmann and Raether[3], Agerwal[4], and Swalen[5] established a convenient method and fundamental theory for the excitation of surface plasmons and their investigation, and introduced surface plasmons into modern optics. In the late 1970s, surface plasmons were firstly employed for the characterization of thin films[6] and the study of processes at metal boundaries[7]. Later, surface plasmon optical has flourished in numerous fields including non-linear optics[8], lasers[9], optical data storage[10], photonic bandgap structures[11-13], sub-diffraction imaging[14], and optical sensors[15, 16].

Surface plasmons originate from collective oscillations of the quasi-free electron gas at an interface between a metal and a dielectric. From Maxwell's equations with standard boundary conditions, there can be shown that an interface between a metal and a dielectric can support SP mode with the propagation constant β as:

$$\beta = k_0 \sqrt{\frac{\varepsilon_d \varepsilon_m}{\varepsilon_d + \varepsilon_m}}, \tag{2.1}$$

where $k_0 = \omega/c = 2\pi/\lambda$ is the wave number of light in vacuum with angular frequency ω, wavelength λ, and speed c. $\varepsilon_m = \varepsilon_m' + i\varepsilon_m''$ and ε_d are the permittivity of metal, and the

semi-infinite dielectric, respectively, and $i=\sqrt{-1}$. Metals such as gold, silver, and aluminum exhibiting a negative real part of permittivity (i.e. $\varepsilon_m' < 0$) can support SPs.

If the real part of the permittivity of the metal is negative and its magnitude is much larger than the imaginary part $|\varepsilon_m'| \gg \varepsilon_m''$, the complex propagation constant of the surface plasmon given by equation (2.1) can be approximated as:

$$\beta = \mathrm{Re}\{\beta\} + i\,\mathrm{Im}\{\beta\} = \frac{\omega}{c}\sqrt{\frac{\varepsilon_d\varepsilon_m'}{\varepsilon_d+\varepsilon_m'}} + i\frac{\varepsilon_m''}{2(\varepsilon_m')^2}\frac{\omega}{c}\left(\frac{\varepsilon_d\varepsilon_m'}{\varepsilon_d+\varepsilon_m'}\right)^{3/2}, \qquad (2.2)$$

where Re{ } and Im{ } denote the real and imaginary part of a complex number, respectively. The imaginary part of the propagation constant is associated with the attenuation of the surface plasmon propagation.

Further, we use geometry depicted in Figure 2.1a with Cartessian coordinate z perpendicular to the metal/dielectric interface. We assume that the metal occupies the region z<0, and the surface plasmon propagates along the x-axis parallel to the interface. Then the electromagnetic field of the surface plasmons (transversal magnetic TM modes) can be expressed as:

$$\vec{E}_m = (E_{xm}, 0, E_{zm})\exp[i(\beta x + k_{zm} z - \omega t)] \text{ for z < 0,} \qquad (2.3)$$

$$\vec{H}_m = (0, H_{ym}, 0)\exp[i(\beta x + k_{zm} z - \omega t)] \text{ for z < 0,} \qquad (2.4)$$

$$\vec{E}_d = (E_{xd}, 0, E_{zd})\exp[i(\beta x - k_{zd} z - \omega t)] \text{ for z > 0,} \qquad (2.5)$$

$$\vec{H}_d = (0, H_{yd}, 0)\exp[i(\beta x - k_{zd} z - \omega t)] \text{ for z > 0,} \qquad (2.6)$$

where $\vec{E}$ and $\vec{H}$ are the electric field and magnetic field, respectively. The component wavevector for the metal (m) and dielectric (d) in z direction k_{zm}, k_{zd} can be expressed as,

$$k_{zj} = \sqrt{\varepsilon_j\left(\frac{\omega}{c}\right)^2 - \beta^2}, \qquad (2.7)$$

where j is d or m.

The electromagnetic field of a surface plasmon reaches its maximum at the metal-dielectric interface and it decays exponentially into the metal and dielectric media, as shown in Figure 2.1b. The field decay in the direction perpendicular to the metal-dielectric interface is characterized by the penetration depth L_p, which is defined as the distance from the interface at which the amplitude of the field decreases by a factor of 1/e. For the metal, the penetration depth expressed as,

$$L_{pm} = 1/\,\mathrm{Im}\{k_{zm}\} = 1/\,\mathrm{Im}\left(\frac{\omega}{c}\frac{\varepsilon_m}{\sqrt{\varepsilon_m + \varepsilon_d}}\right), \tag{2.8}$$

and for the dielectric,

$$L_{pd} = 1/\,\mathrm{Im}\{k_{zd}\} = 1/\,\mathrm{Im}\left(\frac{\omega}{c}\frac{\varepsilon_d}{\sqrt{\varepsilon_m + \varepsilon_d}}\right). \tag{2.9}$$

Surface plasmon propagating along a metal/dielectric interface is damped due to losses in the metal. Finite propagation length L_x of SPs is defined as the distance in the x-direction at which the energy of the surface plasmon decreases by a factor of 1/e:

$$L_x = 1/[2\,\mathrm{Im}\{\beta\}]. \tag{2.10}$$

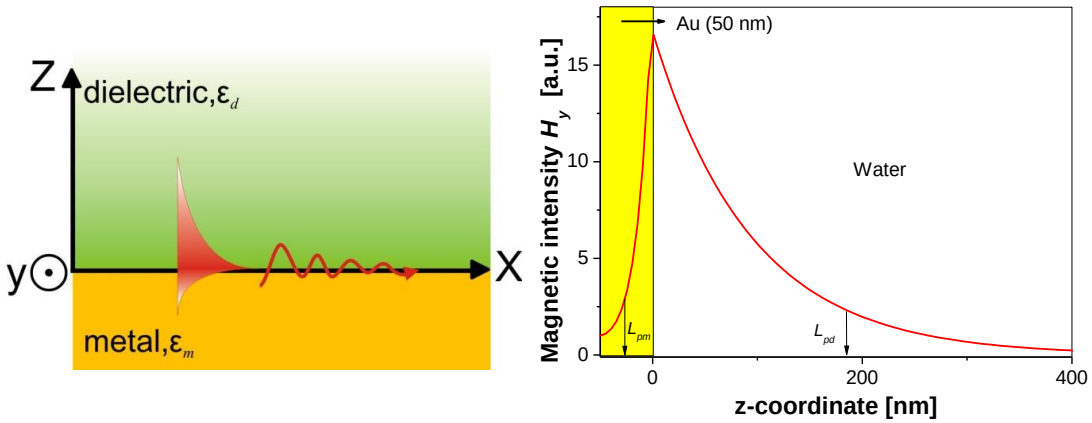

Figure 2.1 a) Schematic presentation of a surface plasmon at the interface between a metal and a dielectric. b) Distribution of magnetic field of a surface plasmon at the interface of gold (ε_m =-12+1.5i) and dielectric (ε_d=1.78), wavelength λ = 633 nm, with the penetration depth L_{pd} = 183 nm, L_{pm} = 27 nm, and propagation length L_x = 7200 nm.

2.1.2 Long range surface plasmons

On a thin metal layer embedded in a dielectric, surface plasmons that are coupled across the metal can be observed, see Figure 2.2. These SP modes were firstly investigated theoretically by Sarid [17], and observed experimentally by Quail et al.[18].

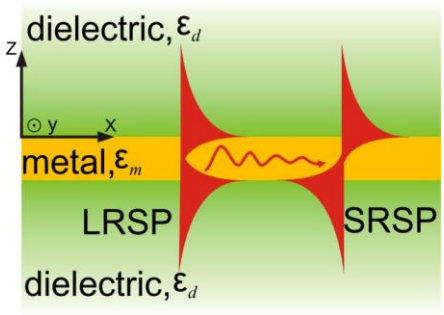

Figure 2.2 Scheme of a LRSP and SRSP, propagated along a thin metal layer sandwiched between two dielectrics.

In general, a metallic film supports two SP modes with propagation constants β that obey the following equation:

$$\tan\left(\kappa d_m\right)=\frac{2\gamma_d\varepsilon_m/\kappa\varepsilon_d}{1-\left(\gamma_d\varepsilon_m/\kappa\varepsilon_d\right)^2}, \tag{2.11}$$

where transverse propagation constants are equal to $\kappa^2=(k_0^2\varepsilon_m-\beta^2)$ and $\gamma^2_d=\beta^2-k_0^2\varepsilon_d$, d_m is the thickness of the metal film, and ε_m, ε_d are the permittivities of metal, and dielectric (Figure 2.2). By solving equation (2.11), there can be shown that Re{β} of the symmetrical mode (refer to the symmetry of the magnetic intensity distribution) is smaller than that of a regular SP (2.1) on an individual interface and it decreases upon decreasing the metal thickness d_m. On the contrary, Re{β} of the anti-symmetric mode is larger than that of a regular SP and it increases when decreasing the thickness d_m, as shown in Figure 2.3a. The propagation length L_x of the symmetric mode is larger and that of anti-symmetric mode is smaller than the one of SP (Figure 2.3b). Therefore, the symmetric and antisymmetric modes are referred to as long range surface plasmon (LRSP) and short range surface plasmon (SRSP), respectively. For thicknesses of the metallic film which are much larger than the penetration depth of SP into the metal $d_m >> L_{pm}$, the coupling across the metal film disappears and thus the propagation constant β of LRSP and SRSP approaches that for the SP on an individual metal-dielectric interface. For small thickness d_m, SPs on opposite interfaces are coupled strongly and the LRSP propagation constant approaches the one of light in the dielectric with permittivity ε_d and the propagation constant of SRSP diverges.

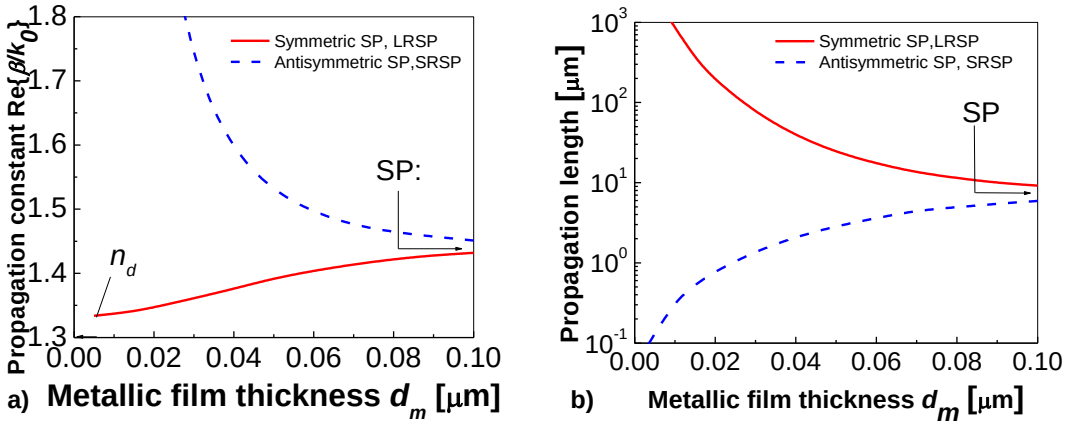

Figure 2.3 Dependence of a) effective index and b) propagation length of LR and SR surface plasmons on the thickness gold metallic film, ε_m=-12.24+0.7i, ε_b=ε_d=1.777, wavelength λ=633 nm.

2.1.3 Optical waveguide modes

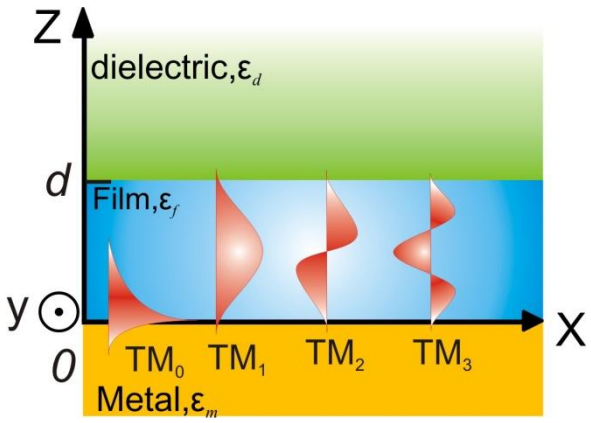

Figure 2.4 Scheme of optical waveguide modes on a structure with metal (ε_m), film (thickness d, ε_f), and dielectric (ε_d).

If a thin dielectric film is attached on a metal surface and its permittivity ε_f is larger than that of adjacent top dielectric medium, additional guided optical waves can be observed as shown in Figure 2.4. We consider a planar structure (Figure 2.4) that comprise dielectric layer (permittivity of ε_f and thickness of d) between a substrate (metal, ε_m) and a superstrate (dielectric, ε_d). The boundary conditions of Maxwell's equations require that the components of the electric and magnetic field intensity vectors parallel to the boundaries of the waveguiding layer are continuous at the boundaries (z=0 and z=d). According to these conditions, one can drive follow dispersion relation of guided waves propagating with distinct propagation constant β in the film:

$$\tan(\kappa d) = \frac{\gamma_d / \kappa + \gamma_m / \kappa}{1 - (\gamma_d / \kappa)(\gamma_m / \kappa)}$$; for the transversal electric (TE) modes, (2.12)

$$\tan(\kappa d) = \frac{\gamma_d \varepsilon_f / \kappa \varepsilon_d + \gamma_m \varepsilon_f / \kappa \varepsilon_m}{1 - (\gamma_d \varepsilon_f / \kappa \varepsilon_d)(\gamma_m \varepsilon_f / \kappa \varepsilon_m)}$$; for the TM modes, (2.13)

where $\kappa^2 = (k_0^2 \varepsilon_f - \beta^2)$, $\gamma^2_m = \beta^2 - k_0^2 \varepsilon_m$ and $\gamma^2_d = \beta^2 - k_0^2 \varepsilon_d$, are the transverse propagation constants in the waveguide film, the metal and dielectric, respectively.

2.1.4 Excitation of surface plasmons

Although surface plasmons can be excited by the bombardment of electrons, optical excitation is more frequently used due to easier experimental implementation. The SP dispersion curve (Figure 2.5c) asymptotically approaches the light line (Figure 2.5a) at low energies, whereas for higher energies it approaches the cutoff angular frequency ω_{max} that is proportional to the metal plasma frequency $\omega_{\max} = \omega_p / \sqrt{1 + \varepsilon_d}$. Considering that the momentum of free photons travelling through a dielectric medium (Figure 2.5a) is always smaller than the propagation constant $\mathrm{Re}\{\beta\}$ of SPs (Figure 2.5c) at the dielectric/metal interface:

$$k_{ph} = \frac{\omega}{c}\sqrt{\varepsilon_d} < \mathrm{Re}\left\{\frac{\omega}{c}\sqrt{\frac{\varepsilon_d \varepsilon_m}{\varepsilon_d + \varepsilon_m}}\right\} = \mathrm{Re}\{\beta\}, \quad (2.14)$$

these two waves cannot be phase-matched along the metal surface due to its insufficient k_{ph}. Therefore direct coupling between them is not possible. In order to optically excite SP, a coupler providing enlargement of the optical wave's momentum needs to be employed. For this purpose, two types of couplers can be used – *prism coupler* employing the attenuated total reflection method (ATR) and *grating coupler* relying on the diffraction of light on periodic modulated metallic surfaces.

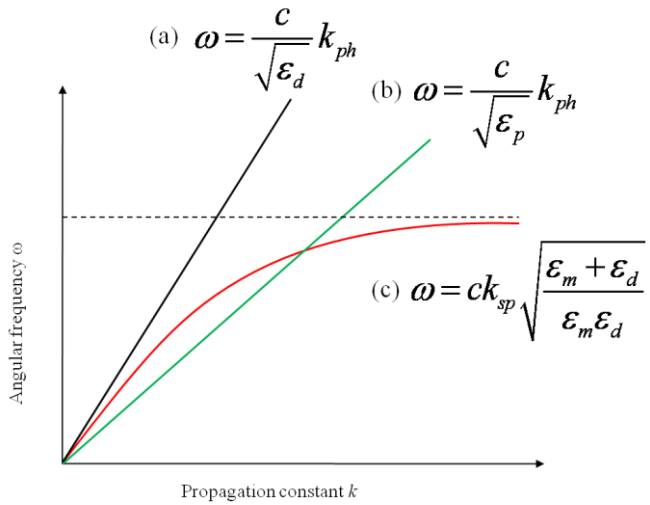

Figure 2.5 The dispersion relation of free photons in a dielectric (a), and in a coupling prism (b) with $\varepsilon_p > \varepsilon_d$, compared to the dispersion relation non-radiative surface plasmons (c) at the metal/dielectric interface.

2.1.4.1 Prism coupler

In a prism coupler, optical excitation of SP is achieved by means of the attenuated total reflection method (ATR). Two implementations of ATR method can be used, which are Otto and Kretschmann geometry. In mostly used Kretschmann geometry of ATR method, an optical beam propagating through the prism with the permittivity ε_p is made incident under an angle of incidence θ on a thin metal layer at the prism base, Figure 2.6a. Upon the incidence, the optical wave totally reflects and its evanescent field penetrates through the thin metal layer. At the interface between the metal and outer dielectric with lower refractive index ($\varepsilon_d < \varepsilon_p$), surface plasmon can be excited as the momentum of the incident optical wave is higher than the one of an optical wave propagating in the outer dielectric, see Figure 2.5b. Excitation of surface plasmon occurs, when the propagation constant of surface plasmon at the interface between the metal and the dielectric with a lower refractive index is matched to the one of the incident optical wave:

$$\frac{\omega}{c}\sqrt{\varepsilon_p}\sin(\theta) = \mathrm{Re}\{\beta\}. \tag{2.15}$$

In ATR method with Kretschmann geometry, the strength of the coupling between an optical wave and surface plasmon wave can be controlled by varying the thickness of the metal layer. The excitation of SP manifests itself as a narrow absorption dip in the

wavelength or angular spectrum of reflectivity (Figure 2.6b). The spectral position of SPR dip can be determined from phase-matching condition (2.15). As follows from this condition, SPR dip position is a function of refractive index ε_d of the dielectric on the metal surface, as:

$$\theta = \arcsin \mathrm{Re}\left\{\sqrt{\frac{\varepsilon_m \varepsilon_d}{(\varepsilon_m + \varepsilon_d)\varepsilon_p}}\right\}. \tag{2.16}$$

The angular spectrum of reflectivity (Figure 2.6b) and field distribution can be calculated based on Fresnel equations and transfer matrix formalism described in literatures[19-24].

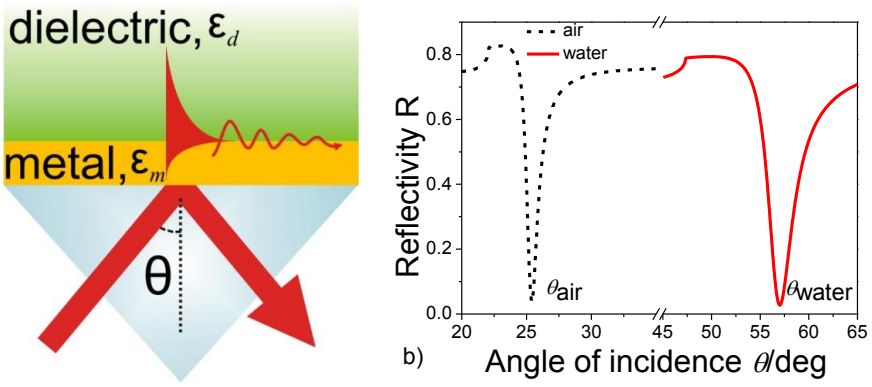

Figure 2.6 Attenuated total reflection method with the Kretschmann geometry for the excitation of surface plasmons, and b) the angular reflectivity spectra for 50 nm Au (ε_{Au} = -12.24+0.7i) on a prism base (ε_p=3.404) in the air ε_d=1 (dots), and water ε_d=1.777 (solid), at wavelength λ=633 nm.

2.1.4.2 Grating coupler

In grating coupler, diffraction on a periodically modulated metallic surface is employed to match propagation constants of an optical wave and SP. As shown in Figure 2.7a, a light beam hits a metallic grating with a period Λ at an incident angle θ. Assuming that the dispersion relation of SPs is only weakly changed by the corrugated surface, the momentum matching condition can be written as:

$$\frac{\omega}{c}\sqrt{\varepsilon_d}\sin(\theta) \pm p\frac{2\pi}{\Lambda} = \mathrm{Re}\{\beta\}, \tag{2.17}$$

where the first term $(\omega/c)\sqrt{\varepsilon_d}\sin(\theta)$ on the left hand side (LHS) represents the component of the propagation constant of the incident light beam that is parallel to the grating surface, and the second LHS term is the contribution due to the diffraction and

integer *p* is the order of diffraction. Similar to ATR coupling, the grating coupled-SPs can be observed as a resonant dip in the spectrum of reflected light (Figure 2.7b). The strength of coupling between an optical wave and a SP is mainly affected by the profile and depth of the modulation of grating surface. Note that the grating constant Λ should be within the same order of magnitude as the wavelength of the incoming light, given the fact that SPR coupling via the first diffraction order (p = ±1) is significantly more efficient than via higher orders. A shallow grating with amplitude of several tens of nanometers is typically sufficient for efficient coupling to SPs. As follows from condition (2.17), the position of SPR dip or peak is a function of permittivity ε_d of the dielectric adjacent to the metal surface.

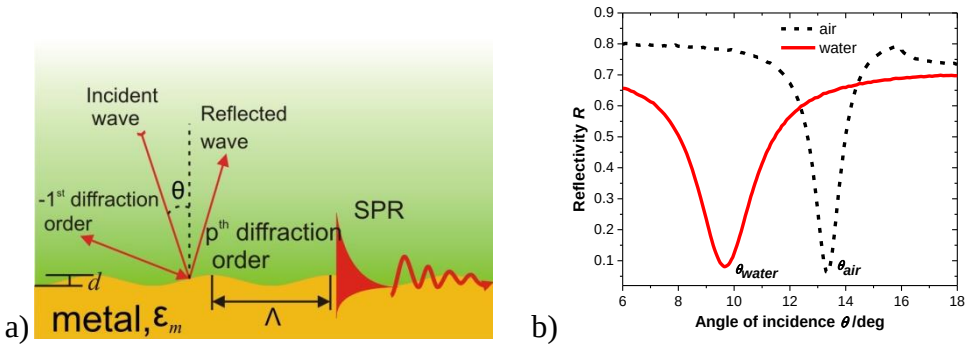

Figure 2.7 (a) Scheme of SPR coupling via a sinusoidal diffraction grating. (b) The SPR angular reflectivity spectra of a diffraction grating with period Λ = ~520 nm, depth d = ~60 nm, and the thickness of Au d_m= 60 nm, measured in (dots) air and (solid) water, at wavelength λ=633 nm.

2.1.4.3 Field enhancement

Upon the coupling of surface plasmon and dielectric waveguide modes, energy of incident wave is accumulated on a surface and the intensity of electromagnetic field is enhanced. The enhancement can be described as factor *K* that is given by the ratio of the magnetic field intensity on the metal surface at the dielectric side divided by the incoming magnetic field intensity of light, i.e. the light intensity at the interface I_S to the incoming light intensity I_0 ($K = I_S/I_0$). For a mere total internal reflection (TIR) geometry, i.e. a glass/water-interface, the reflectivity *R* and enhancement factor *K*, as function of the angle of incidence θ, can be calculated as shown in Figure 2.8a. The enhancement factor of this geometry is maximum of *K*=4 at the critical angle θ_c. However, if the prism base is covered with a thin metal layer to support SPs, then the enhancement factor *K* is improved to 16 for the prism covered with 50 nm of Au layer (Figure 2.8b) due to the contribution of SPs.

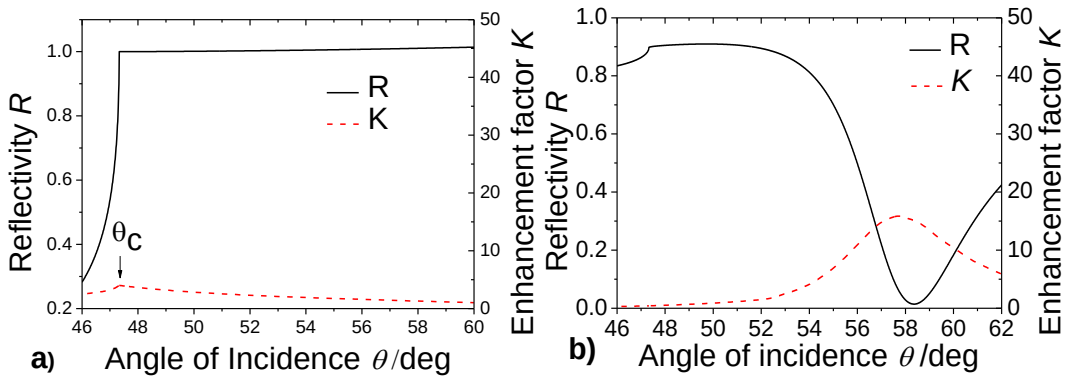

Figure 2.8 Reflectivity R and the intensity enhancement factor K as the function of the angle of incidence θ for a) total internal reflection (TIR) at a glass/water-interface, and b) a plasmon surface polariton excitation at a gold/water-interface (with Au thickness of d_{Au} = 50 nm, n_{Au} = 0.21+ 3.32 i). (Reproduced from[25])

Compared with conventional SPs, the excitation of LRSPs enables to reach higher field enhancement owing to lower damping of these modes. The magnetic field intensity was improved by a factor up to 4 as the excitation of LRSPs on a 20 nm of Au embedded in two dielectrics (900 nm of cytop n_{cytop} = 1.337 and water n_d = 1.333) (Figure 2.9). The evanescent field of LRSP can extend into the medium on top of the gold surface with up to order of magnitude higher depth with respect to conventional SPR (Figure 2.9).

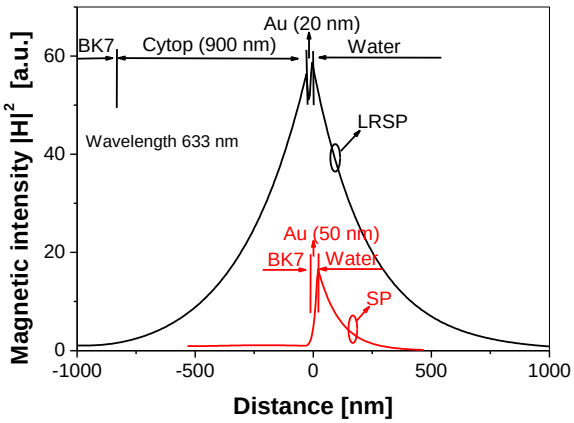

Figure 2.9 Simulated distribution of magnetic intensity across the layer structure upon the excitation of SPs and LRSPs normalized to the intensity of the incident wave in the prism.[26]

2.2 SPR biosensors

2.2.1 Principle of SPR biosensors

In principle, SPR biosensors are thin-film refractometers that measure changes in the refractive index occurring at the surface of a metallic film supporting SPs. SPR biosensors incorporate two key components: a) optical setup for the excitation and interrogation of SPs, and b) biomolecular recognition elements (BRE). The BRE are typically immobilized on the sensor surface or in the sensitive layer (e.g. hydrogel thin layer in this study) probed by evanescent field of resonantly excited SPs. The binding of analyte molecules to the BRE induces a change in the refractive index in the vicinity to the metallic surface δn which produces a change of propagation constant $\delta\beta$ and consequently changes the coupling condition to SPs, as indicated in equations (2.1), (2.15), (2.17). Therefore, the molecular binding events can be detected by measuring variations of the characteristics of the light wave coupled to the SP. In SPR biosensor with angular modulation (employed in this study), a monochromatic light wave is used to excite an SP. Thus the molecular binding events are monitored as a shift in the angular SPR reflectivity dip $\Delta\theta$, or the reflectivity changes ΔR at an angle set to the vicinity to the resonance.

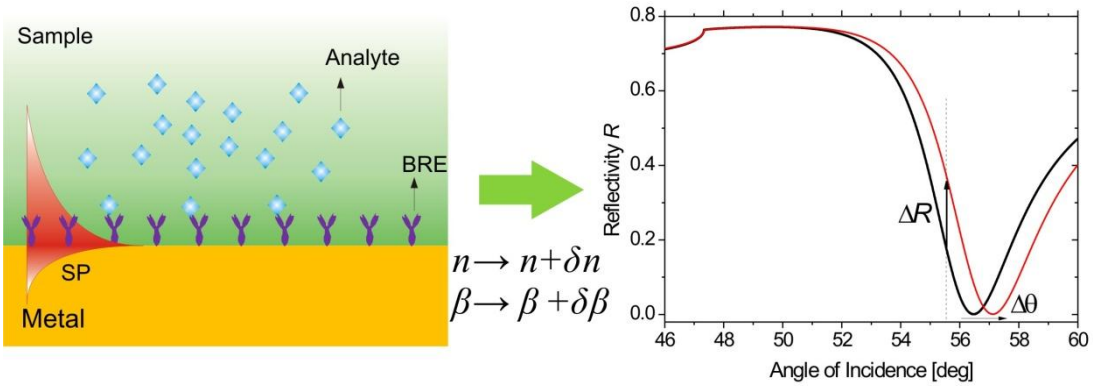

Figure 2.10 principle of operation of SPR biosensors measuring the binding-induced refractive index changes as a shit in the SPR resonant angle $\Delta\theta$, or the changes of reflectivity ΔR.

2.2.2 Interfacial molecular interactions

The capture/release of biomolecules at a surface of an SPR biosensor is controlled by various mechanisms that result in variety of temporal profiles of the SPR biosensor response. The binding kinetics provides information on interaction of molecules on a surface and their analyses allow to assess important parameters such as affinity binding rate constants. This is commonly considered one of the greatest advantages of the SPR biosensor technique.

2.2.2.1 Langmuir adsorption model

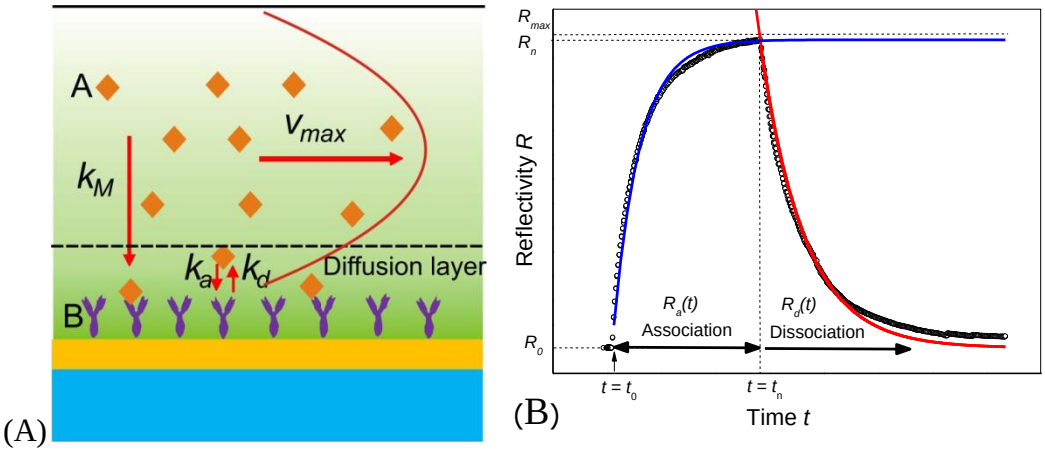

Figure 2.11 (A) Schematic presenting the basic interactions of biomolecules on the surface. (B) An examples of a typical interaction analysis and fitting involving an association and a dissociation process.

The basic theory that can describe SPR binding kinetics has been carried out in detail by Christensen[27], and is briefly summarized here. The physical system is composed of a sensor surface bearing a specific ligand, and a ligand-binding analyte in a soluble phase, which is flowed over the surface. In a two-compartment model (Figure 2.11A), the interaction between the analyte and the ligand can be described by the following two-step process,

$$A_{bulk} \underset{k_m}{\overset{k_m}{\rightleftarrows}} A_{surface} + B \underset{k_d}{\overset{k_a}{\rightleftarrows}} AB \,, \tag{2.18}$$

where the first step describes the mass transport of the analyte, A, between the bulk flow and the surface. The second step describes the chemical interaction leading to the formation of a complex between A and the ligand B, at the sensor surface. In equation

(2.18), k_m is the mass transport coefficient, k_a is the association rate constant, and k_d is the dissociation rate constant. Experimentally, the conditions where the mass transport and affinity binding are decoupled are difficult to reach. Thus, under most circumstances both steps have to be considered as described by the following equations:

$$\frac{d[A_{surface}]}{dt} = \frac{k_m([A_{bulk}]-[A_{surface}]) - k_a[A_{surface}][B] + k_d[AB]}{h_{diff}}, \tag{2.19}$$

and

$$\frac{d[AB]}{dt} = k_a[A_{surface}][B] - k_d[AB], \tag{2.20}$$

where

$$h_{diff} = \left(\frac{Dh^2wL}{v_{\max}} \right)^{1/3}, \tag{2.21}$$

is a characteristic height of the diffusion layer (i.e. the layer where the solution is unstirred) that links the change in concentration expressed per surface area ([*AB*]) and per volume ([$A_{surface}$]). The diffusion coefficient of the analyte is denoted *D*, while v_{max} is the bulk flow velocity in the center of the flow-cell, *h*, *w* and *L* are the height, width, and length of the flow chamber, respectively. If the diffusion coefficient is not known, it can be estimated from the molecular mass of the analyte, utilizing Stoke's law together with the Einstein-Sutherland equation,

$$D = \frac{k_B T}{6\pi r \eta}, \tag{2.22}$$

where k_B is the Boltzman constant, *T* is the absolute temperature, η is the viscosity of the fluid and *r* is the radius of the sphere approximating the molecule size.

If quasi-steady state conditions are assumed, i.e., $d[A_{surface}]/dt=0$, and with rearrangement of equation (2.19), the following expression for the analyte concentration at the surface is obtained,

$$[A_{surface}] = \frac{k_m[A_{bulk}] + k_d[AB]}{k_m + k_a[B]}, \tag{2.23}$$

where

$$k_m \approx 1.378\left(\frac{\nu_{\max} D^2}{hL}\right)^{1/3}. \tag{2.24}$$

Insertion of equation (2.23) into equation (2.20) gives

$$\frac{d[AB]}{dt} = k_a\left(\frac{k_m[A_{bulk}] + k_d[AB]}{k_m + k_a[B]}\right)[B] - k_d[AB], \tag{2.25}$$

which describes the formation of a 1:1 complex between *A* and *B* under partially limiting mass transport conditions.

2.2.2.2 Mass transfer-controlled kinetics

The mass transport effect can be quantified by using a Damköhler number in the following form:

$$Da = \frac{k_a[B]}{k_m} = k_a[B]\left(\frac{\nu_{\max} D^2}{hL}\right)^{-1/3}, \tag{2.26}$$

where the numerical constant is excluded. For large Damköhler number $Da >> 1$, i.e. $k_m << k_a[B]$, the sensorgram profile is completely controlled by the diffusion mass transfer. Thus equation (2.25) leads to

$$\frac{d[AB]}{dt} = k_m[A_{bulk}]. \tag{2.27}$$

Therefore, the complex [*AB*] forming rate is solely dependent on the bulk concentration of *A*, and the binding signal increases linearly with time with slope of k_m.

2.2.2.3 Interaction controlled kinetics

If Damköhler number $Da << 1$, i.e. $k_m >> k_a[B]$, the mass transport is much faster than the surface reaction itself and therefore the mass transport effect may be ignored. Thus, the concentration of analyte on the sensor surface is equal to the bulk concentration, i.e. $[A_{surface}] = [A_{bulk}]$. From equation (2.20), the binding rate can be rewritten as

$$\frac{d[AB]}{dt} = k_a[A_{bulk}][B] - k_d[AB]. \tag{2.28}$$

Since the surface concentration [*B*] is the function of time *t*, which is the difference between the concentration of complex at saturation and the current complex concentration,

$$[B] = [AB_{\max}] - [AB]. \tag{2.29}$$

Considering that the response R scales linearly with the complex concentration [*AB*], i.e., $R=M_wG[AB]$, where M_w is the molecular mass of the analyte and G is a factor converting the concentration to R values. Inserting (2.29) into (2.28), one gets,

$$\frac{dR}{dt} = k_a \alpha (R_{\max} - R) - k_d R , \tag{2.30}$$

where α is the concentration of analyte, R_{max} is the saturation signal (i.e. a theoretical maximum value of R) when all the immobilized ligand B has been fully bound into a complex, i.e., [*AB*]=[*B*]. The equation (2.30) may be solved by integration, giving the solution

$$R_a(t) = \left(R_{\max} - R_0\right)\left(1 - e^{-(k_a\alpha + k_d)(t-t_0)}\right) + R_0 , \tag{2.31}$$

where R_0 is the reflectivity R at the time $t=t_0$.

At the dissociation phase, $\alpha = 0$, thus,

$$\frac{dR}{dt} = -k_d R . \tag{2.32}$$

The solution becomes

$$R_d(t) = (R_n - R_0)e^{-k_d(t-t_n)} + R_0 , \tag{2.33}$$

where R_n is the reflectivity R at the time $t=t_n$, when the dissociation process starts. Equation (2.31) and (2.33) can be used to yield k_a and k_d from a single set of association/dissociation data using non-linear curve fitting, as shown in Figure 2.11B.

2.2.2.4 Equilibrium analysis

Upon dynamic equilibrium, the net effect of the association and dissociation process is zero, i.e.

$$\frac{d[AB]}{dt} = k_a[A_{bulk}]([AB_{\max}] - [AB]) - k_d[AB] = 0 . \tag{2.34}$$

Thus, the amount of complex [AB] can be expressed as,

$$[AB] = \frac{k_a[A_{bulk}][AB_{\max}]}{k_a[A_{bulk}] + k_d} , \tag{2.35}$$

or expressed as the SPR response R_{eq},

$$R_{eq} = \frac{k_a \alpha R_{\max}}{k_a \alpha + k_d} = \frac{\alpha R_{\max}}{\alpha + K_D}, \tag{2.36}$$

where $K_D=k_d/k_a$. Upon application of an analyte concentration of $\alpha=K_D$, R_{eq} is half of the saturation response R_{max}. The time to reach equilibrium can be calculated by the following equation deduced from (2.31):

$$t = \frac{-Ln(1 - R / R_{eq})}{k_a \alpha + k_d}. \tag{2.37}$$

For instance, at $\alpha=K_D$, it takes ~$1/k_d$ period of time to reach 90% association equilibrium.

2.2.3 Characteristics of SPR biosensors

The main performance characteristics of SPR biosensors include sensitivity, resolution, reproducibility, dynamic range, and limit of detection.

2.2.3.1 Sensitivity and resolution

In the angular modulation the sensitivity $S_{\theta b}$ to the bulk refractive index changes δn_b can be expressed as:

$$S_{\theta b} = \frac{\delta \theta_r}{\delta n_b}, \tag{2.38}$$

where θ_r is the resonant angle at which the reflectivity is minimum. For SPR affinity biosensors, the molecular binding events induced changes in the refractive index typical occurs only within a very short distance d from the sensor surface. Assuming $d << L_{pd}$ (the penetration depth of SP), thus an effective bulk refractive index change that is seen by a SP mode can be expressed as

$$\delta n_b = \delta n_s \frac{2d}{L_{pd}}, \tag{2.39}$$

where δn_s is the refractive index change in a thin film with the thickness of d. The sensitivity to the surface refractive index changes δn_s can be written as

$$S_{\theta s} = \frac{\delta \theta_r}{\delta n_s} = 2 S_{\theta b} \frac{d}{L_{pd}}. \tag{2.40}$$

This equation suggests that the surface refractive index sensitivity $S_{\theta s}$ is proportional to the bulk refractive index sensitivity $S_{\theta b}$ and the thickness of the binding layer d, and inversely proportional to the penetration depth L_{pd} of SP.

In the intensity modulation, one typically monitors the reflectivity changes at an angle $\theta<\theta_r$ (resonant angle) where ratio $\Delta R/\Delta\theta$ is linear with a slope $S_{R\theta} = \left|\Delta R/\Delta\theta\right|$ (see Figure 2.10). Thus the reflectivity sensitivity of SPR biosensors to the bulk refractive index changes can be deduced from equation (2.38) as:

$$S_{Rb} = \frac{\delta R}{\delta n_b} = \frac{\delta\theta_r}{\delta n_b} S_{R\theta} = S_{\theta b} S_{R\theta}, \tag{2.41}$$

and the reflectivity sensitivity of SPR biosensors to the molecular binding-induced surface refractive index changes δn_s within the layer of a thickness of $d << L_{pd}$ can be expressed as

$$S_{Rs} = \frac{\delta R}{\delta n_s} = 2 S_{Rb} \frac{d}{L_{pd}}. \tag{2.42}$$

The resolution of an SPR sensor is defined as the smallest change in the bulk refractive index that produces a detectable change in the sensor output. The magnitude of sensor output change that can be detected depends on the level of uncertainty of the sensor outputs-the output noise. In this study, intensity modulation is used for monitoring the refractive index changes. Therefore, the resolution of an SPR sensor, r_R, is typically expressed in terms of the standard deviation of the reflectivity, σ_R, translated to the refractive index of bulk medium,

$$r_R = \sigma_R / S_{Rb}. \tag{2.43}$$

2.2.3.2 Limit of detection (LOD)

The limit of detection (LOD) is usually defined as the concentration of analyte that produces sensor output corresponding to 3 standard deviations σ of sensor output measured for a blank sample. The ultimate LOD can be predicted when the smallest detectable surface mass changes of the biosensors and the parameters of the interaction between the analyte and BRE and mass transport to the sensor surface are known.

The surface mass changes ΔΓ (mass/area) of captured molecule on the sensor surface can be expressed as,

$$\Delta\Gamma = \frac{\delta n_s \times d}{\partial n / \partial c} = \frac{\delta R \times d}{S_{Rs}(\partial n / \partial c)} = \frac{\delta\theta \times d}{S_{\theta s}(\partial n / \partial c)} \tag{2.44}$$

where $\partial n_h/\partial c$ denotes the volume refractive index increment of the molecular concentration (typically 0.1~ 0.3 $mm^3\ mg^{-1}$, and ~0.2 $mm^3\ mg^{-1}$ for IgG[28]).

When the molecule binding thickness $d << L_{pd}$, e.g. SPR biosensors based on 2D SAM, inserting equation (2.42) into (2.44), one gets

$$\Delta\Gamma\Big|_{d<<L_{pd}} = \frac{\delta R \times L_{pd}}{2S_{Rb}(\partial n / \partial c)} = \frac{\delta\theta \times L_{pd}}{2S_{\theta b}(\partial n / \partial c)}. \tag{2.45}$$

Therefore, the minimum detectable surface mass changes σ_Γ is determined by the minimum detectable reflectivity changes, which is defined as 3 times of the standard deviations of reflectivity measured for a blank sample, i.e. $3\sigma_R$. Thus from equations (2.43) and (2.45), we can deduce the minimum detectable surface mass changes σ_Γ as,

$$\sigma_\Gamma = \frac{3r_R \times L_{pd}}{2(\partial n / \partial c)}. \tag{2.46}$$

This equation indicated that the minimum detectable surface mass or LOD is decreased with the decrease of the penetration depth L_{pd} of SP and the resolution r_R.

The bound amount of analyte on a sensor surface is dependent on the bulk concentration of analyte α, the affinity binding rate constant and the mass transport of analyte to the surface, which was discussed before. Further, two cases are assumed to estimate the LOD, **a)** the analyte binding is mass transfer-controlled (see section 2.2.2.2), and **b)** the binding is interaction controlled (see section 2.2.2.3).

For **a)** the mass transfer-controlled (MTC) kinetics (i.e. $Da>>1$), the minimum detectable concentration (i.e. LOD) α_{LOD_MTC} can be estimated according to equation (2.27), i.e.

$$\alpha_{LOD\_MTC} = \frac{\sigma_\Gamma}{k_m \Delta t}, \tag{2.47}$$

where k_m is the diffusion rate and Δt is the reaction time. Insert equation (2.46) into(2.47), one gets

$$\alpha_{LOD\_MTC} = \frac{3r_R \times L_{pd}}{2k_m \Delta t(\partial n / \partial c)}. \tag{2.48}$$

For an SPR biosensor operating at the wavelength of λ=632.8 nm with the L_{pd} = 180 nm, the resolution of r_R = 1×10^{-5} RIU^{-1}, a typical analyte with a refractive index increment $\partial n_h/\partial c$= 0.2 mm^3 mg^{-1}, and the k_m = 3×10^{-3} mm s^{-1}, detection time of Δt=30 min, the equations (2.46) and (2.48) give the minimum detectable mass changes σ_Γ = 13.5 pg mm^{-2}, and the LOD α_{LOD_MTC}= 2.5 ng ml^{-1} (i.e. 17 pM for 150kDa of IgG), respectively.

For **b)** the affinity interaction-controlled (AIC) kinetics, according to equation (2.28), we determined the minimum detectable mass changes as function of LOD α_{LOD_AIC}, i.e.

$$\sigma_\Gamma = \frac{k_a \alpha_{LOD\_AIC} \Gamma_{BRE}}{k_a \alpha_{LOD\_AIC} + k_d}(1 - e^{-(k_a \alpha_{LOD\_AIC} + k_d)\Delta t}), \tag{2.49}$$

where Γ_{BRE} is the surface coverage of the biomolecular recognition element (BRE) immobilized on the sensor surface, k_a and k_d is the association and dissociation rate constant, respectively, and Δt is the detection time. Then the LOD α_{LOD_AIC} can be solved according to the equation (2.49), when the other parameters are known. The equation (2.49) tells that the LOD can be improved (smaller) if the surface coverage of BRE Γ_{BRE} is increased (larger) and/or the affinity interaction between analyte and BRE is stronger, i.e. k_a is larger, k_d is smaller.

2.2.4 SPR and hydrogel optical waveguide

A hydrogel film that is attached to a metal surface can support guided light waves if its refractive index and the thickness are sufficiently large (see 2.1.3). For the prism coupler, the propagation constant β should fulfill equation (2.15). The SP and hydrogel optical waveguide (HOW) can be excited on a same substrate, thus the interaction between a monochromatic light-beam and guided waves on the surface is manifested as series of resonant dips in the angular reflectivity spectrum R(θ) located at angles for which each modes hold the conditions (2.15) and (2.13), see Figure 2.12.

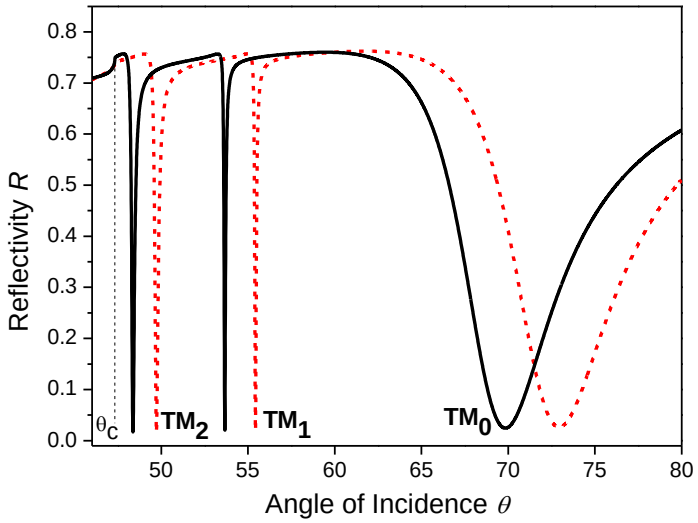

Figure 2.12 (a) Angular reflectivity spectra for the excitation (prism coupler, n_{prism}=1.845) of HOW (TM_1 and TM_2) and SP (TM_0) on an Au surface (n_{Au}= 0.2+3.5i, d_{Au}=50 nm) with a hydrogel thin layer (n_h=1.42, d_h=1200 nm) in water (n_{water}=1.333), before (solid) and after (dash) the immobilization of ligand which changes the refractive index of hydrogel layer to be n_h=1.43.

Spectroscopy of surface plasmon and hydrogel waveguide waves provides a powerful technique for *in situ* observation of hydrogel films. It allows real-time monitoring of changes in their characteristics such as thickness d_h and refractive index n_h that are associated with variations in optical properties. These parameters can be obtained by fitting a Fresnel reflectivity for a multilayer (e.g., based on transfer matrix formalism) to the measured reflectivity spectra *R(θ)* in which the hydrogel density is approximated by using a "box model". In this model, the dependence of the refractive index perpendicular to the surface *n(x)* is assumed to be the following function of the distance from the surface:

$$n(x) = n_d + (n_h - n_d)H(d_h - x), \tag{2.50}$$

where x is the axis perpendicular to the sensor surface (x=0 is the position at the interface between the metal and hydrogel) and H is the Heaviside step function. For small refractive index n_h of a hydrogel, its surface mass density Γ can be calculated as:

$$\Gamma = (n_h - n_d) \times d_h \times \frac{\partial c}{\partial n_h}, \tag{2.51}$$

where the coefficient $\partial n_h/\partial c \sim 0.2$ mm^3 mg^{-1} relates changes in the refractive index and concentration of organic materials in the gel (e.g., polymer or proteins). From effective medium theory follows that polymer volume fraction *f* of a swollen hydrogel is equal to:

$$f = \frac{(n_h{}^2 - n_d{}^2)(n_{h-dry}{}^2 + 2n_d{}^2)}{(n_h{}^2 + 2n_d{}^2)(n_{h-dry}{}^2 - n_d{}^2)}, \quad (2.52)$$

where $n_{h\text{-}dry}$ is the refractive index of hydrogel in dry state.

2.3 Surface plasmon field-enhanced fluorescence spectroscopy

Fluorescence techniques have been widely applied for chemical, physical, biological and clinical purposes. In general, fluorescence detection offers high sensitivity that allows detection of even single molecules. Surface plasmon resonance spectroscopy has been combined with fluorescence spectroscopy, as referred to surface plasmon field-enhanced fluorescence spectroscopy (SPFS), which uses greatly enhanced electromagnetic field obtained at the surface plasmon resonance to excite the fluorescent dyes in the vicinity of the metal/dielectric interface. Most of the intriguing features of fluorescence, such as high-sensitivity, multiplexing detection, can be directly inherited by SPFS. Thus it has become a very powerful tool for detection and quantitative evaluation of interfacial binding reactions.

2.3.1 Fluorescence process

Fluorescence is a phenomenon accompanied with absorption of a photon and its re-emission at higher wavelength. It is a result of a three-stage spontaneous process that occurs in certain molecules (generally polyaromatics hydrocarbons or heterocycles) called fluorophores (e.g. quantum dots or organic dyes). Fluorophores often exhibit strongly delocalized electrons in conjugated double bonds or aromatic systems. The molecular processes during absorption and emission of photons are illustrated by the schematic Jablonski energy level diagram shown in Figure 2.13.

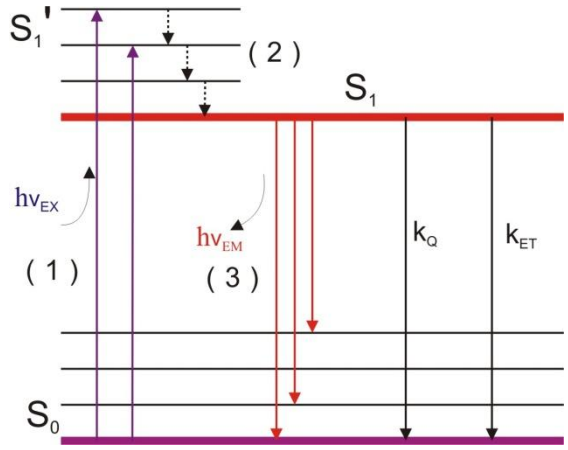

Figure 2.13 Jablonski diagram illustrating the electronic and vibrational states of a fluorophore and processes during photon adsorption and fluorescence emission (Reproduced from[29]).

Stage 1: Excitation

A photon of energy hv_{EX} is supplied by an external source such as an incandescent lamp or a laser and absorbed by the fluorophore, creating an excited electronic singlet state (S_1').

Stage 2: Excited-State Lifetime

The excited state exists for a finite time (typically 1–10 nanoseconds). During this time, the fluorophore undergoes conformational changes and is also subject to a multitude of possible interactions with its molecular environment. In this processes the energy of S_1' is partially dissipated, yielding a relaxed singlet excited state (S_1) from which fluorescence emission originates. Furthermore, the energy of S_1 may also be depopulated by the other processes such as collisional quenching (k_Q), fluorescence resonance energy transfer (FRET, k_{ET}) and intersystem crossing (k_{IC}). They all influence the fluorescence quantum yield Φ, which is the ratio of the number of fluorescence photon emitted to the number of photon absorbed.

$$\Phi = \frac{k_F}{k_F + k_D}, \tag{2.53}$$

where k_F, $k_D = k_Q + k_{ET} + k_{IC}$ is the rate constant of the fluorescence process, and the depopulation process, respectively.

Stage 3: Fluorescence Emission

A photon of energy $h\nu_{EM}$ is emitted, returning the fluorophore to its ground state S_0. Due to energy dissipation during the excited-state lifetime (stage 2), the energy of this emitted photon is lower, and therefore of longer wavelength, than the excitation photon $h\nu_{EX}$. The difference in energy or wavelength represented by ($h\nu_{EX}$-$h\nu_{EM}$) is called the Stokes shift. The Stokes shift is fundamental to the sensitivity of fluorescence techniques because it allows emission photons to be detected against a low background, isolated from the excitation photons.

2.3.2 Photobleaching

A typical fluorophore can undergo a finite number of excitation-relaxation cycles prior to photochemical destruction. This process is often referred to as photobleaching, photofading or photodestruction. For a photostable fluorophore, e.g. tetramethylrhodamin, photobleaching occurs after about 10^5 cycles. In contrast, fluorescein photobleaches very easily. Generally speaking, the photobleaching involves the generation of reactive oxygen molecules, thus it is sometimes useful to introduce antioxidants or to use anoxic conditions. On the other hand, the rate of the photobleaching is often proportional to the intensity of illumination. Therefore, a simple practical way to overcome this is to reduce the time or the intensity of the excitation radiation.

2.3.3 Fluorescence at the metal-dielectric interface

In this work, the evanescent field of surface plasmon is used for the excitation of fluorescence on the metal-dielectric interface, i.e. SPFS, thus it is very important to understand the behavior of fluorophores in the vicinity of metals. A fluorophore close to a surface can be excited by the evanescent wave. For that, the fluorophores should be placed within the decay length of the evanescent field for excitation, which is typically hundreds of nanometers for surface plasmon (Figure 2.14a). On the other hand, metals can also act as generic quenchers. The excited state of the fluorophore can couple to the broad band of electronic states in bulk metal and relax by essentially heating up the metal slightly. The mathematical simulation as shown in Figure 2.14a, depicts the excitation and de-excitation situation of a fluorophore within the surface plasmon evanescent field.

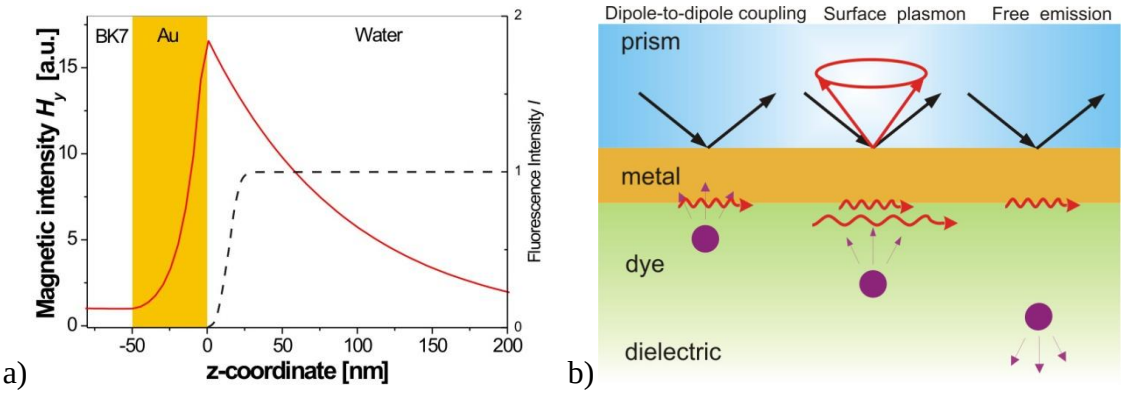

Figure 2.14 (a) Scheme of a fluorophore positioned close to a metal-dielectric interface. Different fluorescence decay channels take place at different fluorophore/metal separation distances. (b) Distribution of magnetic field of a surface plasmon at the interface of gold-water interface (see Figure 2.1 a) Schematic presentation of a surface plasmon at the interface between a metal and a dielectric.) (solid line), and the fluorescence intensity profile of a fluorophore near a (quenching) metal surface (dashed line), reproduced from reference[30].

If a dye is positioned at a distance within 10 nm to the metal surface, the non-radiative decay of fluorescence is the dominating process. The excitation is assumed to be dipole-to-dipole, if it is due to the excitation of an electron-hole pair (exciton) in the metal. The standard Föster model gives an R^{-6} dependence of the transfer rate to the separation distance (Figure 2.14b), due to the co-effect from both near fields of the donor molecule and the acceptor molecule. However, the distance dependence of energy transfers involving a dye and a surface (could be rough) can be greatly compromised to be $R^{-3} \sim R^{-4}$ dependent due to the integration over the enlarged number of effective acceptor sites. The transferred energy dissipated by the metal is converted into heat.

At an intermediate-distance regime (e.g. 10-20 nm), a significant fraction of excited fluorescence couples back to SPs, by fulfilling momentum matching conditions. Unless SP modes can be converted again into photons by a coupling prism or a grating, which allows for the monitoring of SP decay channel, it represents a significant loss of fluorescence yield.

At sufficient separation distances (>20 nm), free emission of the dyes dominates. However, the fluorescence yield cannot be directly obtained unless two effects are considered. Firstly, the fluorescence emission oscillates as the distance increases, since

the metal reflects the fluorescence field and introduces light interference. Secondly, the excitation source, i.e., the evanescent field weakens as the distance increases.

2.4 Hydrogel film for evanescent filed biosensors: an overview

Hydrogels are insoluble, cross-linked water-swollen polymer networks of hydrophilic homopolymers or copolymers. Owing to their highly open structure and large inner surface, hydrogels can accommodate large amounts of molecules with specific functions. Hydrogels become irreplaceable materials in numerous important areas ranging from pharmaceutical applications (e.g., drug delivery or tissue engineering) [31-36] to biosensor technologies for detection of chemical or biological analytes[37-42]. In biosensor applications, hydrogel materials are employed at an interface between an analyzed aqueous sample and a transducer. Typically, the hydrogel interface is modified with biomolecular recognition elements (BREs) such as antibodies, enzymes or with biomimetic molecular imprinted moieties in order to specifically recognize target analytes, see Figure 2.15. Compared to other types of biointerfaces (e.g., based on self assembled monolayers-SAM), hydrogels can accommodate orders of magnitude larger amounts of recognition elements [43], provide more natural microenvironment for biomolecules that increases their stability [44] and offer routes for implementing of additional functionalities (e.g. separation of target analyte from other molecules in a sample [45]). In addition, the class of "smart" gels that respond to external stimuli become of increasing interest in biosensor research. For instance, a miniature holographic hydrogel elements based on these materials were integrated in a contact lens for the real-time analysis of glucose in a tear fluid [46].

In this section, optical biosensors in which hydrogel films with thickness up to several micrometers serve as a binding matrix were overviewed. The key performance characteristics of crosslinked hydrogel binding matrices, their characterization and implementations were discussed here. In particular, methods that rely on probing of hydrogel structures by an evanescent field of surface plasmon and optical waveguide waves for the observation of changes in hydrogel films and detection of molecular analytes are introduced. Biosensors with thinner polymer brushes (structures in which polymer chains are not crosslinked and are individually anchored to a surface) are not discussed here.

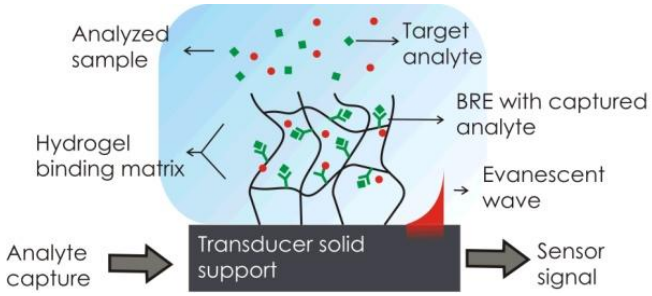

Figure 2.15 Scheme of a hydrogel-based biointerface on top of a biosensor surface for detection of molecular analytes.

2.4.1 Key characteristics of hydrogel binding matrices

Various organic polymers were synthesized and applied for hydrogel biointerface architectures as reported in literature. These include alginate [47], chitosan [48], dextran [43], poly(vinylalcohol) (PVA) [49], 2-hydroxyethyl methacrylate (HEMA) [50, 51], poly(2-vinylpyridine) (P2VP) [52, 53], poly(ethylene glycol) (PEG) [54] and poly(N-isopropylacrylamide) (PNIPAAm) [55, 56]. In addition, sol-gels that are formed by the polymerization of silicate monomers were applied for development of micro-porous matrices in which analyte-sensitive species can be entrapped with large densities [57]. Compared to inorganic porous films that were explored for a construction of binding matrices (e.g. porous silicon [58], aluminum oxides [59, 60], silicon dioxide [61], titanium oxide [62]), soft organic hydrogel matrices provide a platform offering the advantage of better biocompatibility, larger variety of functionalization methods and responsive properties. In the following section, we discuss characteristics of hydrogels that are essential for their successful implementation to a biosensor binding matrix.

2.4.1.1 Diffusion of target analyte

In order to reach fast detection times, target analytes have to rapidly diffuse through the hydrogel binding matrix and react with incorporated recognition elements. The mesh size ξ and the molecule hydrodynamic radius r_h are the key parameters affecting the diffusion-driven mass transport in gels in which the diffusion coefficient scales as $D_g \sim \exp(-r_h/\xi)$. In highly swollen gels with $r_h << \xi$, D_g of mobile target molecules is close to that in water and the recognition elements in hydrogels are easily accessible for the binding. However, diffusion is dramatically hindered by steric and hydrodynamic interactions when the size of the mobile molecules is comparable to the mesh size $r_h \sim \xi$.

The distance between polymer crosslinks provides a measure for the mesh size ξ and it is related to the hydrogel swelling ratio Q defined as the ratio of the thickness in swollen (hydrated) and collapsed (dry) state. The swelling ratio Q is inversely proportional to the polymer volume fraction f. These parameters can be controlled through the gel composition and cross-linking density.

For instance, PNIPAAm and dextran-based hydrogel binding matrices were successfully applied in evanescent wave biosensors for detection of protein molecules [43, 56]. For a functionalized PNIPAAm-based hydrogel with f ~ 0.1, Huang et al. estimated that the diffusion coefficient D_g of IgG (hydrodynamic radius r_h = 6 nm [63]) was close to 10^{-6} mm^2 s^{-1} [64] which is more than order of magnitude lower than in a water ($D_s=3\times10^{-5}$ mm^2s^{-1}). Raccis et al. measured a diffusion coefficient of $D_g\sim10^{-5}$ mm^2 s^{-1} for green fluorescence protein (GFP, hydrodynamic radius r_h = 2.3 nm [65]) in a similar PNIPAAm gel with the polymer volume content f ~ 0.05 by fluorescence correlation spectroscopy (FCS) [66]. A special class of "smart" responsive hydrogels can change its swelling characteristics through applied external stimulus such as a change in temperature or pH. Hydrogels can be sensitized to other types of stimuli such as light irradiation (through incorporation of metallic nanoparticles supporting localized surface plasmon [67]) or magnetic field (through their modification by magnetic nanoparticles [68, 69]). The characteristic time of the hydrogel response to the stimuli scales with its size Δx and diffusion coefficient D of the network as $\sim\Delta x^2/D$, where D is in the order of 10^{-4}-10^{-6} mm^2s^{-1} for most common gels [40].

2.4.1.2 Antifouling properties

The development of polymer films that are resistant against fouling by molecular, cellular and other species present in complex samples (e.g. blood, sea water) is a major challenge in the field of biomaterials research. In biosensor applications, the antifouling properties of a biointerface determine the capability of whole biosensor system to selectively detect target molecules present in an analyzed sample. Although general physical and chemical properties of antifouling surfaces are still under research, following conditions were identified to be necessary for good resistance against non-specific sorption: (i) zero net charge, (ii) hydrophilic nature, and presence of groups that are (iii) hydrogen bond acceptors but (iv) not hydrogen bound donors [70-73]. Furthermore, the permeability of hydrogel layer may also affect the antifouling properties of hydrogel, since the low

porosity of hydrogel may hinder the large biomolecules interactions. Traditionally, PEG-based polymers are employed for design of surfaces that exhibit good resistance against non-specific sorption. Recently, improved antifouling properties were reported for polymer surfaces with nanometer-scale homogenous mixtures of zwitterionic or charged groups [74].

For instance, Jiang group observed that ultra-low nonspecific adsorption (<3 pg/mm^2) from blood plasma occurred on films composed of poly(sulfobetaine) and poly(carboxybetaine) polymers with a thickness of several tens of nanometers [75, 76]. Liedberg group investigated non-specific sorption on a surface with mixed polyelectrolyte gradient prepared by free-radical grafting of the anionic polyelectrolyte poly(2-carboxyethyl acrylate) (PCEA) and cationic polyelectrolyte in a layer consisting of poly(2-aminoethyl methacrylate)(PAEMA). For the optimum composition with balanced charge and thickness around 40 nm, adsorption of about 80 pg/mm^2 from plasma was reported [77]. Tabrizian group has developed a composite cross-linked hydrogel with the thickness of few nanometers consisting of carboxymethyl cellulose (CMC), polyethyleneimine (PEI) and poly(ethylene glycol) (PEG). They showed that on a thin CMC-PEG-PEI hydrogel nonspecific sorption of 1.1 ng/mm^2 occurred from 25% serum [78]. Masson et al. investigated non-specific sorption in three-dimensional open structures of carboxymethylated (CM) dextran [79]. Their results indicated that the non-specific sorption from bovine serum increases with the molecular weight of CM dextran chains. For the CM dextran molecular weight between 2 and 5000 kDa, the mass of non-specifically adsorbed molecules between 2 and 23 ng/mm^2 was reported. In addition, they showed several-fold improvement of the non-specific interactions by using other biocompatible polymer derivatives such as CM hyaluronic acid. Dostalek group studied anti-fouling properties of crosslinked dextran and PNIPAAm-based hydrogels with a thickness of 1-2 μm that exhibited open structure in which analyte can diffuse. Non-specific sorption from blood serum lead to a surface mass density change of around 5 ng/mm^2 [43, 80]. In general, the surface mass density of nonspecifically bound molecules in open three-dimensional gels is orders of magnitude higher compared to dense thinner films due to the higher surface area.

2.4.2 Biosensor implementations

In this section, an overview of implementations of evanescent wave biosensors with hydrogel binding matrix is presented. Selected examples of different biosensor schemes with molecular imprinted hydrogels, responsive gels modified with enzymes and biosensors relying on nucleic acids and immunoassays are introduced and their performance characteristics discussed.

2.4.2.1 Molecular imprinted hydrogel-based biosensors

Molecular imprinted hydrogels have attracted a great deal of attention over the last decade [81, 82]. In biosensor area, we witnessed numerous implementations of such materials for refractometric-based detection of low molecular weight analytes relevant to medical diagnostics and environmental monitoring. Hydrogel-based imprinted matrices with responsive properties were shown to allow enhancing the sensitivity through binding-induced collapse or swelling that is associated with stronger refractive index changes and thus can be detected more accurately.

Willner et al. [83] developed a molecular-imprinted acrylamide-acrylamidophenylboronic acid copolymer (AMPBA-AA) hydrogel for detection of β-nicotinamide adenine dinucleotide (NAD^+), β-nicotinamide adenine dinucleotide phosphate ($NADP^+$), and their reduced forms (NADH and NADPH), see Figure 2.16. SPR was employed for the detection of molecular binding events and the sensor system took advantage of enhanced the refractive index changes associated with the binding-induced swelling of the imprinted gel. Detection of $NAD(P)^+$ and NAD(P)H in the concentration range of 1 μM to 1 mM was reported.

In order to provide stronger binding-induced refractive index changes, gold nanoparticles were incorporated into molecular imprinted hydrogels [84, 85]. In such materials, higher sensor response can be observed for swelling and collapse of a gel owing to distance-dependent interaction between Au nanoparticles. For instance, a SPR sensor for detection of dopamine (important neurotransmitter) was developed by using imprinted hydrogel which consisted of acrylic acid (AA), N-isopropylacrylamide (NIPAAm), N,N'-methylenbisacrylamide (MBS) [85].

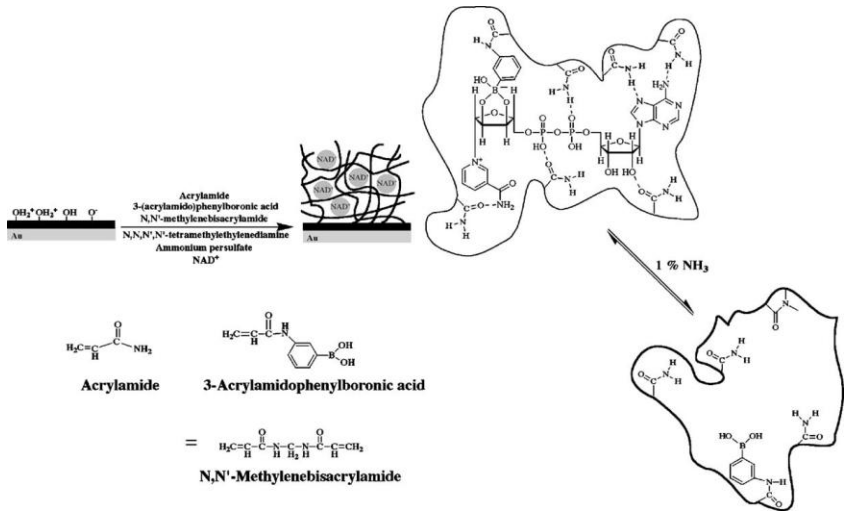

Figure 2.16 $NAD(P)^+$/NAD(P)H cofactors-imprinted acrylamide-acrylamidophenylboronic acid copolymer on an Au-coated glass for SPR-based detection. (Reproduced from [83]).

Besides continuous hydrogel films, swellable molecular imprinted hydrogel particles were used for a construction of a binding matrix which offers faster diffusion of analyte to the polymer. Lavine et al. employed such surface architecture for the detection of theophylline [86]. On a gold surface, polyN-(N-propyl)acrylamide (polyNNPA) nanoparticles with a diameter of 300 nm were attached in this work. The binding of theophylline was associated with increasing hydrophilicity of the hydrogel which resulted in swelling of the gel particles. The associated decrease in the refractive index due to the theophylline capture was subsequently detected by SPR. The sensor was capable of specific detection of theophilline at concentrations above 10 μM.

2.4.2.2 Enzyme-based biosensors

Enzyme recognition elements are available for detection of range of analytes related to medical diagnostics. When immobilized into responsive hydrogels, their interaction with target analyte leads to a catalytic reaction which changes their environment characteristics such as pH. The enzyme reaction-induced collapse or swelling of a gel can be subsequently converted to a sensor signal providing sensitive means for detecting of target molecules.

Bagal et al. developed a sucrose biosensor based on a agarose-guar gum binding matrix with acid invertase and glucose oxidase [57]. This film was attached with the thickness of 12 μm to a single mode optical waveguide. Based on the detection of the refractive index changes ascribed to the specific binding of sucrose in the waveguide

layer, the monitoring of the attenuation of the waveguide provided rapid detection time of 110 s and limit of detection as low of 25 pM.

A waveguide structure with a 1 μm thick sol-gel matrix was employed for the absorption and fluorescence spectroscopy-based detection of glucose by Zourob et al. [87]. The sol-gel matrix was immobilized with glucose oxidase and a fluorescent ruthenium complex which is sensitive to pH. The sensing scheme was based on the measuring of ruthenium complex quenching due to the protonation of the excited state of the complex when gluconic acid is released by the bio-oxidation of glucose. The sensor demonstrated the limit of detection of 3 μM.

Various biosensors based on "smart" hydrogel/nanoparticles composites and enzyme reaction was reported by Minko group [88, 89]. They relied on the molecular binding-induced swelling and a distance-dependent interaction of metal nanoparticles incorporated in a gel, see Figure 2.17. Through variations in the swelling/collapse of the hydrogel host, the interaction strength of embedded nanoparticles changes leading to a modulation of resonance absorption spectra. For instance, 20-25 nm thick alginate-gelatin film with encapsulated silver nanoparticles was deposited on a solid surface with silver islands. This scheme was demonstrated to respond to pH changes that were caused by the biocatalytic reaction of glucose oxidase (GOx) in the gel. Through the observation absorption spectra changes, detection of glucose at concentration down to 0.1 mM was reported. Endo et al. [90] developed a responsive hydrogel composed of acrylamide (AAm), bisacrylamide (bis-AAm) and PVP-coated silver nanoparticles for a glucose biosensor. The mechanism of the sensor was based on the formation of a reduced flavin adenine dinucleotide (FAD) anion, gluconic acid and hydrogen peroxide upon glucose turnover that resulted in the swelling of hydrogel and degradation of silver nanoparticles [90]. Based on this mechanism, enzyme biosensor for detection of glucose at as low as 10 pM concentration was demonstrated.

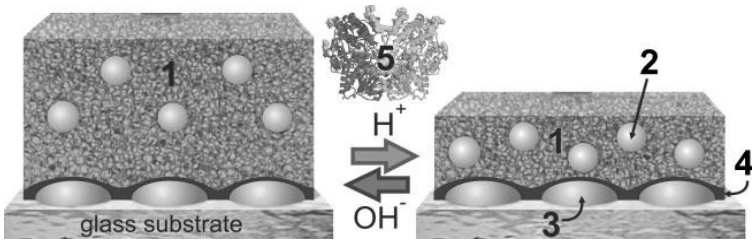

Figure 2.17 Plasmonic sensing device consisting of an ultrathin alginate-gelatin gel film (1) with silver nanoparticles (2) immobilized on silver nanoislands (3) via a PGMA layer (4). The film undergoes a reversible swelling transition in response to pH changes caused by the biocatalytic reaction of GOx (5) and glucose. (Reproduced from[88]).

2.4.2.3 Nucleic acids-based biosensors

Hydrogel matrices with oligonucleotide probes were implemented for the detection of nucleic acids by using SPR and fluorescence spectroscopy.

In Nilsson's group, a water-soluble polythiophene polymer composed of poly (3-[(S)-5-amino-5-carboxyl-3-oxapentyl]-2,5-thiophenylene hydrochloride) (POWT) with zwitterionic peptide-like side chains was used for the coupling of probe DNA via electrostatic and hydrogen bonding [91, 92]. As Figure 2.18a shows, the zwitterionic side-chains carry serine carboxylic groups with a p*Ka* of 2.19 and an amino group with a p*Ka* of 9.21 which are responsible for pH-dependent conformational transitions in the gel [93]. POWT undergoes aggregation accompanied with a transition to a denser and straightened structure (rod-shaped polymer backbone) upon the binding of single-stranded negatively charged oligonucleotide (ssDNA) which can be translated to a sensor signal by SPR.

In addition, the POWT can emit fluorescence light and the emission wavelength and intensity is sensitive to electrostatic interaction of polymer chains. Nilsson et al. have shown that the emission band of POWT polymer shifts to longer wavelengths as the net charge of the polymer side-chains become more negative [93]. A negatively charged ssDNA can interact with the positive amino groups of the polymer chain, and subsequently form hydrogen bonds with the amino and carboxyl groups of a nearby polymer chain which leads to a red shift of the fluorescence wavelength (Figure 2.18b). A hybridization of DNA in such gel is accompanied with disruption of hydrogen bonds between polymer chains and ssDNA which leads to a separation of polymer chains, see Figure 2.18b. Upon the DNA hybridization, the intensity of the emitted fluorescence light is increased and blue shifted [92]. This method allowed detection of DNA at the concentration as low as 6.7 nM.

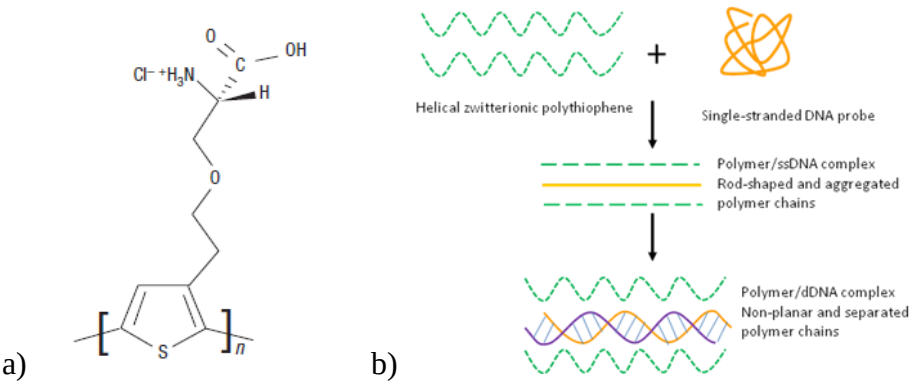

Figure 2.18 a) The repeated unit of POWT. B) The formation of POWT/DNA complexes. Geometrical changes of POWT (dotted lines) on addition of ssDNA (solid lines) and dsDNA (helical structure). (Reproduced from [92]).

Another type of nucleic acids-based biosensor based on aptamer cross-linked polyacrylamide (PAA) hydrogels were developed in Tan's group for the detection of small molecules, such as adenosine [94] and cocaine [95]. Used hydrogels were modified by two DNA strands that were crosslinked by an aptamer linker. A competitive binding of the target to the aptamer resulted in a reduction of cross-linking density that caused gel dissolution and subsequent release of AuNPs or enzyme. The released AuNPs or the enzyme activity can be observed by absorption spectroscopy in visible part of spectrum and allowed detection of cocaine at the concentrations lower than 1 μM within 10 min [95].

2.4.2.4 Immunoassay-based biosensors

Immunoassays present an established and most popular method for detection of chemical and biological analytes owing to a wide range of antibodies commercial available, their versatility and high affinity. Biosensor schemes with antibodies immobilized in hydrogel films take advantage of increased binding capacity and lower steric hindrance offered by their open (three-dimensional) structure. Three representative examples of biosensors developed for immunoassays-based detection of target molecules by label-free techniques relying on the monitoring of binding-induced refractive index changes and by using fluorescence spectroscopy are discussed in following section.

Liedberg et al. employed SPRi biosensor for the investigation of gradient hydrogel matrix composed of poly(ethylene glycol) methacrylate ($PEG_{10}MA$) and 2-hydroxyethyl methacrylate (HEMA) [45]. Biospecific interaction of serum albumin (HSA)/anti-HSA

antibody and calmodulin (CaM)/calmodulin binding domain (CBD) pairs was studied as a function of thickness and composition of the matrix. CaM with low molecular weight was shown to diffuse and interact throughout entire hydrogel matrix. However, HSA diffusion was hindered by the low porosity of hydrogel matrix and thus it reacted only on the top of the gel. The sensitivity for the detection of CaM was dependent on the thickness of hydrogel, and the highest sensitivity for detection of this analyte was achieved for the thickness of $PEG_{10}MA$/HEMA hydrogel matrix of 70 nm.

In this study, we will introduce an immunosensor for detection of free prostate specific antigen (f-PSA) supported by a highly swollen 1 μm thick photo-crosslinked carboxymethyl dextran (PCMD) hydrogel binding matrix (see Chapter 5), and a highly swollen PNIPAAm hydrogel with a thickness around 2 μm for a construction a label-free immunosensor based on hydrogel optical waveguide spectroscopy (HOWS) (see Chapter 6).

Table 2.1 Overview of hydrogel biosensors based on evanescent wave optics

Recognition element	Material	Detection method	Thickness d_h	Analyte	LOD (sample)	Ref.
MIP	P2VP-AuNPs	LSPR	31 nm	cholesterol	n.a. (chloroform)	[53]
	AMPBA-AA	SPR	22 nm	$NAD(P)^+$ NAD(P)H	1 μM (buffer)	[83]
	AA-NIPAAm-MBS-AuNPs	SPR	~6 μm (dry)	dopamine	1 nM (water)	[85]
	polyNNPA	SPR	~300 nm	Theophylline	10 μM (buffer)	[86]
	MAA-EGDMA-AIBN-AuNPs	SPR	251nm	atrazine	5 pM (acetonitrile)	[96]
Enzyme	agaros-guar gum polysaccharide	OWS	12 μm	sucrose	25 pM (buffer)	[57]
	agarose co-polymer	OWS	1 μm	paraoxon	6 nM (buffer)	[87]
	agarose co-polymer	OWS-Fluorescence	1 μm	glucose	3 μM (buffer)	[87]
	alginate-gelatin-AgNPs	LSPR	20 nm (dry)	glucose	0.1 mM (buffer)	[88]
	AAm-bisAAm-AgNPs	LSPR	~1 mm	glucose	10 pM (buffer)	[90]

Nucleic acid	POWT	SPR	8 nm (dry)	DNA	n.a. (buffer)	[91]
	aptamer-PAA	LSPR	n.a.	adenosine	n.a. (buffer)	[94]
	aptamer-PAA	LSPR	n.a.	cocanie	n.a. (buffer)	[95]
Immuno-assay	CMD	LR-SPR	~1 µm	f-PSA	0.68 nM (buffer)	Chap 5[43]
	CMD	LRSP-FS	~1 µm	f-PSA	34 fM (buffer) 330 fM (human serum)	Chap 5[43]
	PNIPAAm	HOWS	~2 µm	IgG	10 pM (buffer)	Chap 6[56]
	$PEG_{10}MA$-HEMA	SPRi	5-45 nm	HSA and calmodulin	n.a. (buffer)	[45]

2.4.3 Conclusion and outlook

Hydrogel materials allowed impressively advancing the performance of biosensors and helped to push these technologies towards applications in important areas such as medical diagnostics and environmental monitoring. Particularly, we witnessed development of new hydrogel materials with excellent resistance against nonspecific sorption from complex samples as well as advances in their recognition characteristics through incorporation of specific moieties by molecular imprinting or coupling of biomolecular recognition elements. As illustrated in this chapter, evanescent wave optics provides valuable tools for the observation of thin hydrogel films and their implementation in biosensor devices. We expect that future biosensor technologies will increasingly take advantage of "smart" hydrogels with responsive properties which enables increasing their sensitivity and implementing new simplified detection schemes. In addition, recognition of target analytes based on molecular imprinting will surely play prominent role in future biosensor technologies. In conjunction with optical biosensors, advances in molecular imprinted large binding capacity-materials hold potential to deliver urgently needed tools for direct label-free detection of low molecular weight molecules such as drugs in medical diagnostics or pollutants in environmental monitoring. For such analytes, currently established technologies including immunoassay-based SPR lack the sensitivity and long-term stability.

References

1. Wood, R. W. (1902). On a Remarkable Case of Uneven Distribution of Light in a Diffraction Grating Spectrum, *Philosophical Magazine*, **4**, 396.
2. Otto, A. (1968). Excitation of Nonradiative Surface Plasma Waves in Silver by Method of Frustrated Total Reflection, *Zeitschrift fur Physik*, **216**, 398.
3. Kretschmann, E. and Raether, H. (1968). Radiative Decay of Non Radiative Surface Plasmons Excited by Light, *Zeitschrift fur Naturforschung Part A-Astrophysik Physik und Physikalische Chemie A*, **23**, 2135.
4. Agarwal, G. S. (1973). New Method in Theory of Surface Polaritons, *Physical Review B*, **8**, 4768-4779.
5. Swalen, J. D. (1986). Optical Properties of Langmuir-Blodgett Films, *Journal of Molecular Electronics*, **2**, 155-181.
6. Pockrand, I., Swalen, J. D., Gordon, J. G. and Philpott, M. R. (1978). Surface plasmon spectroscopy of organic monolayer assemblies, *Surface Science*, **74**, 237-244.
7. Gordon Ii, J. G. and Ernst, S. (1980). Surface plasmons as a probe of the electrochemical interface, *Surface Science*, **101**, 499-506.
8. Nazvanov, V. F. and Kovalenko, D. I. (1998). Phase optical bistability in structures with surface plasmons, *Technical Physics Letters*, **24**, 650-651.
9. Colombelli, R., Srinivasan, K., Troccoli, M., Painter, O., Gmachl, C. F., Tennant, D. M., Sergent, A. M., Sivco, D. L., Cho, A. Y. and Capasso, F. (2003). Quantum cascade surface-emitting photonic crystal laser, *Science*, **302**, 1374-1377.
10. Ditlbacher, H., Krenn, J. R., Lamprecht, B., Leitner, A. and Aussenegg, F. R. (2000). Spectrally coded optical data storage by metal nanoparticles, *Optics Letters*, **25**, 563-565.
11. Barnes, W. L., Preist, T. W., Kitson, S. C., Sambles, J. R., Cotter, N. P. K. and Nash, D. J. (1995). Photonic Gaps in the Dispersion of Surface-Plasmons on Gratings, *Physical Review B*, **51**, 11164-11167.
12. Bergmair, M., Huber, M. and Hingerl, K. (2006). Band structure, Wiener bounds, and coupled surface plasmons in one dimensional photonic crystals, *Applied Physics Letters*, **89**, -.
13. Barnes, W. L., Preist, T. W., Kitson, S. C. and Sambles, J. R. (1996). Physical origin of photonic energy gaps in the propagation of surface plasmons on gratings, *Physical Review B*, **54**, 6227-6244.
14. Fang, N., Lee, H., Sun, C. and Zhang, X. (2005). Sub-diffraction-limited optical imaging with a silver superlens, *Science*, **308**, 534-537.
15. Homola, J. (2003). Present and future of surface plasmon resonance biosensors, *Analytical and Bioanalytical Chemistry*, **377**, 528-539.
16. Homola, J. (2009). Surface plasmon resonance biosensors, *Febs Journal*, **276**, 63-63.
17. Sarid, D. (1981). Long-range surface-plasma waves on vary thin metal films, *Phys. Rev. Lett.*, **47**, 1927-1930.
18. Quail, J. C., Rako, J. G. and Simon, H. J. (1983). Long-range surface-plasmon modes in silver and aluminum films, *Opt Lett*, **8**, 377-9.
19. Kurihara, K. and Suzuki, K. (2002). Theoretical understanding of an absorption-based surface plasmon resonance sensor based on Kretchmann's theory, *Analytical Chemistry*, **74**, 696-701.
20. Ekgasit, S., Thammacharoen, C. and Knoll, W. (2004). Surface plasmon resonance spectroscopy based on evanescent field treatment, *Analytical Chemistry*, **76**, 561-568.
21. Ekgasit, S., Thammacharoen, C., Yu, F. and Knoll, W. (2004). Evanescent field in surface plasmon resonance and surface plasmon field-enhanced fluorescence spectroscopies, *Analytical Chemistry*, **76**, 2210-2219.
22. Hansen, W. N. (1968). Electric Fields Produced by the Propagation of Plane Coherent Electromagnetic Radiation in a Stratified Medium, *J. Opt. Soc. Am.*, **58**, 380-388.
23. Davis, T. J. (2009). Surface plasmon modes in multi-layer thin-films, *Optics*

Communications, **282**, 135-140.
24. Shalabney, A. and Abdulhalim, I. (2010). Electromagnetic fields distribution in multilayer thin film structures and the origin of sensitivity enhancement in surface plasmon resonance sensors, *Sensors and Actuators a-Physical*, **159**, 24-32.
25. Liebermann, T. and Knoll, W. (2000). Surface-plasmon field-enhanced fluorescence spectroscopy, *Colloid. Surface. A*, **171**, 115-130.
26. Dostalek, J., Kasry, A. and Knoll, W. (2007). Long range surface plasmons for observation of biomolecular binding events at metallic surfaces, *Plasmonics*, **2**, 97-106.
27. Christensen, L. L. H. (1997). Theoretical analysis of protein concentration determination using biosensor technology under conditions of partial mass transport limitation, *Analytical Biochemistry*, **249**, 153-164.
28. Homola, J. (2008). Surface plasmon resonance sensors for detection of chemical and biological species, *Chemical Reviews*, **108**, 462-493.
29. Valeur, B., *Molecular Fluorescence Principles and Applications*. 2002, Wiley-VCH: Weingeim.
30. Neumann, T., Johansson, M. L., Kambhampati, D. and Knoll, W. (2002). Surface-plasmon fluorescence spectroscopy, *Adv. Funct. Mater.*, **12**, 575-586.
31. Nicodemus, G. D. and Bryant, S. J. (2008). Cell encapsulation in biodegradable hydrogels for tissue engineering applications, *Tissue Eng. Part B-Rev.*, **14**, 149-165.
32. Shoichet, M. S. (2010). Polymer scaffolds for biomaterials applications, *Macromolecules*, **43**, 581-591.
33. Slaughter, B. V., Khurshid, S. S., Fisher, O. Z., Khademhosseini, A. and Peppas, N. A. (2009). Hydrogels in regenerative medicine, *Adv. Mater.*, **21**, 3307-3329.
34. Hamidi, M., Azadi, A. and Rafiei, P. (2008). Hydrogel nanoparticles in drug delivery, *Adv. Drug Deliver. Rev.*, **60**, 1638-1649.
35. Hoare, T. R. and Kohane, D. S. (2008). Hydrogels in drug delivery: Progress and challenges, *Polymer*, **49**, 1993-2007.
36. Bajpai, A. K., Shukla, S. K., Bhanu, S. and Kankane, S. (2008). Responsive polymers in controlled drug delivery, *Prog. Polym. Sci.*, **33**, 1088-1118.
37. Gerlach, M. G. a. G. (2009) *Hydrogels for chemical sensors*, in *Hydrogel sensors and actuators*, G.A. Urban, Editor. Springer: Heidelberg. p. 165.
38. Richter, A., Paschew, G., Klatt, S., Lienig, J., Arndt, K. F. and Adler, H. J. P. (2008). Review on hydrogel-based pH sensors and microsensors, *Sensors*, **8**, 561-581.
39. Weiss, G. A. U. a. T. (2009) *Hydrogels for biosensors*, in *Hydrogel sensors and actuators*, G.A. Urban, Editor. Springer: Heidelberg. p. 197.
40. Tokarev, I. and Minko, S. (2009). Stimulli-responsive hydrogel thin films, *Soft Matter*, **5**, 511-524.
41. Davies, M. L., Murphy, S. M., Hamilton, C. J. and Tighe, B. J. (1992). Polymer membranes in clinical sensor applications. 3. Hydrogels as reactive matrix membranes in fiber optic sensors, *Biomaterials*, **13**, 991-999.
42. Murphy, S. M., Hamilton, C. J., Davies, M. L. and Tighe, B. J. (1992). Polymer mbranes in clinical sensor applications. .2. The design and fabrication of permselective hydrogels for electrochemical devices, *Biomaterials*, **13**, 979-990.
43. Wang, Y., Brunsen, A., Jonas, U., Dostalek, J. and Knoll, W. (2009). Prostate specific antigen biosensor based on long range surface plasmon-enhanced fluorescence spectroscopy and dextran hydrogel binding matrix, *Anal. Chem.*, **81**, 9625-9632.
44. Gerhke, S. H., Uhden, L. H. and McBride, J. F. (1998). Enhanced loading and activity retention of bioactive proteins in hydrogel delivery systems, *J. Controlled Release*, **55**, 21-33.
45. Andersson, O., Larsson, A., Ekbald, T. and Liedberg, B. (2009). Gradient hydrogel matrix for microarray and biosensor applications: an imaging SPR study, *Biomacromolecules*, **10**, 142-148.
46. Yang, X. P., Pan, X. H., Blyth, J. and Lowe, C. R. (2008). Towards the real-time monitoring of glucose in tear fluid: Holographic glucose sensors with reduced

interference from lactate and pH, *Biosens. Bioelectron.*, **23**, 899-905.
47. Ladet, S., David, L. and Domard, A. (2008). Multi-membrane hydrogels, *Nature*, **452**, 76-U6.
48. Berger, J., Reist, M., Mayer, J. M., Felt, O., Peppas, N. A. and Gurny, R. (2004). Structure and interactions in covalently and ionically crosslinked chitosan hydrogels for biomedical applications, *Eur. J.Pharm. Biopharm.*, **57**, 19-34.
49. Li, N., Liu, Z. Z. and Xu, S. G. (2000). Dynamically formed poly (vinyl alcohol) ultrafiltration membranes with good anti-fouling characteristics, *J. Membrane Sci.*, **169**, 17-28.
50. Bakshi, A., Fisher, O., Dagci, T., Himes, B. T., Fischer, I. and Lowman, A. (2004). Mechanically engineered hydrogel scaffolds for axonal growth and angiogenesis after transplantation in spinal cord injury, *J. Neurosurg.-Spine*, **1**, 322-329.
51. Guvendiren, M., Yang, S. and Burdick, J. A. (2009). Swelling-induced surface patterns in hydrogels with gradient crosslinking density, *Adv. Funct. Mater.*, **19**, 3038-3045.
52. Tokarev, I., Tokareva, I. and Minko, S. (2008). Gold-nanoparticle-enhanced plasmonic effects in a responsive polymer gel, *Adv. Mater.*, **20**, 2730-2734.
53. Tokareva, I., Tokarev, I., Minko, S., Hutter, E. and Fendler, J. H. (2006). Ultrathin molecularly imprinted polymer sensors employing enhanced transmission surface plasmon resonance spectroscopy, *Chem. Commun.*, 3343-3345.
54. Ishihara, K., Kobayashi, M., Ishimaru, N. and Shinohara, I. (1984). Glucose induced permeation control of insulin through complexmembrane consisting of immobilized glucose oxidase and a poly(amine), *Polym. J.*, **16**,
55. Beines, P. W., Klosterkamp, I., Menges, B., Jonas, U. and Knoll, W. (2007). Responsive thin hydrogel layers from photo-cross-linkable poly(N-isopropylacrylamide) terpolymers, *Langmuir*, **23**, 2231-2238.
56. Wang, Y., Huang, C. J., Jonas, U., Wei, T. X., Dostalek, J. and Knoll, W. (2010). Biosensor based on hydrogel optical waveguide spectroscopy, *Biosens. Bioelectron.*, **25**, 1663-1668.
57. Bagal, D. S., Vijayan, A., Aiyer, R. C., Karekar, R. N. and Karve, M. S. (2007). Fabrication of sucrose biosensor based on single mode planar optical waveguide using co-immobilized plant invertase and GOD, *Biosens. Bioelectron.*, **22**, 3072-3079.
58. Janshoff, A., Dancil, K. P. S., Steinem, C., Greiner, D. P., Lin, V. S. Y., Gurtner, C., Motesharei, K., Sailor, M. J. and Ghadiri, M. R. (1998). Macroporous p-type silicon Fabry-Perot layers. Fabrication, characterization, and applications in biosensing, *J. Am. Chem. Soc.*, **120**, 12108-12116.
59. Lau, K. H. A., Tan, L. S., Tamada, K., Sander, M. S. and Knoll, W. (2004). Highly sensitive detection of processes occurring inside nanoporous anodic alumina templates: A waveguide optical study, *J. Phys. Chem. B*, **108**, 10812-10818.
60. Feng, C. L., Zhong, X. H., Steinhart, M., Caminade, A. M., Majoral, J. P. and Knoll, W. (2007). Graded-bandgap quantum-dot-modified nanotubes: A sensitive biosensor for enhanced detection of DNA hybridization, *Adv. Mater.*, **19**, 1933-+.
61. Kambhampati, D. K., Jakob, T. A. M., Robertson, J. W., Cai, M., Pemberton, J. E. and Knoll, W. (2001). Novel silicon dioxide sol-gel films for potential sensor applications: A surface plasmon resonance study, *Langmuir*, **17**, 1169-1175.
62. Cameron, P. J., Jenkins, A. T. A., Knoll, W., Marken, F., Milsom, E. V. and Williams, T. L. (2008). Optical waveguide spectroscopy study of the transport and binding of cytochrome c in mesoporous titanium dioxide electrodes, *J. Mater. Chem.*, **18**, 4304-4310.
63. Jossang, T., Feder, J. and Rosenqvist, E. (1988). Photon correlation spectroscopy of human IgG, *J. Proten. Chem.*, **7**, 1573-4943.
64. Huang, C. J., Dostalek, J. and Knoll, W. (2010). Evanescent wave optical affinity biosensor with 3D hydrogel binding matrix: on the role of mass transport *Biosens. Bioelectron.*, **In Press**,
65. Hink, M. A., Griep, R. A., Borst, J. W., van Hoek, A., Eppink, M. H. M., Schots, A. and Visser, A. J. W. G. (2000). Structural dynamics of green fluorescent protein alone and

fused with a single chain Fv protein, *J. Biol. Chem.*, **275**, 17556-17560.
66. Raccis, R. (personal communication).
67. Sershen, S. R., Mensing, G. A., Ng, M., Halas, N. J., Beebe, D. J. and West, J. L. (2005). Independent opical control of microfluidic valves formed from optomechanicaly responsive nanocomposite hydrogels, *Adv. Mater.*, **17**,
68. Satarkar, N. S., Zhang, W. L., Eitel, R. E. and Hilt, J. Z. (2009). Magnetic hydrogel nanocomposites as remote controlled microfluidic valves, *Lab Chip*, **9**, 1773-1779.
69. Fuhrer, R., Athanassiou, E. K., Luechinger, N. A. and Stark, W. J. (2009). Crosslinking metal nanoparticles into the polymer backbone of hydrogels enables preparation of soft, magnetic field-driven actuators with muscle-like flexibility, *Small*, **5**, 383-388.
70. Ostuni, E., Chapman, R. G., Liang, M. N., Meluleni, G., Pier, G., Ingber, D. E. and Whitesides, G. M. (2001). Self-assembled monolayers that resist the adsorption of proteins and the adhesion of bacterial and mammalian cells, *Langmuir*, **17**, 6336-6343.
71. Ostuni, E., Chapman, R. G., Holmlin, R. E., Takayama, S. and Whitesides, G. M. (2001). A survey of structure-property relationships of surfaces that resist the adsorption of protein, *Langmuir*, **17**, 5605-5620.
72. Holmlin, R. E., Chen, X. X., Chapman, R. G., Takayama, S. and Whitesides, G. M. (2001). Zwitterionic SAMs that resist nonspecific adsorption of protein from aqueous buffer, *Langmuir*, **17**, 2841-2850.
73. Prime, K. L. and Whitesides, G. M. (1991). Self-assembled organic monolayers-model systems for studying adsorption of proteins at surfaces, *Science*, **252**, 1164-1167.
74. Chen, S. F., Zheng, J., Li, L. Y. and Jiang, S. Y. (2005). Strong resistance of phosphorylcholine self-assembled monolayers to protein adsorption: Insights into nonfouling properties of zwitterionic materials, *J. Am. Chem. Soc.*, **127**, 14473-14478.
75. Zhang, Z., Chen, S. F., Chang, Y. and Jiang, S. Y. (2006). Surface grafted sulfobetaine polymers via atom transfer radical polymerization as superlow fouling coatings, *J. Phys. Chem. B*, **110**, 10799-10804.
76. Vaisocherova, H., Yang, W., Zhang, Z., Cao, Z. Q., Cheng, G., Piliarik, M., Homola, J. and Jiang, S. Y. (2008). Ultralow fouling and functionalizable surface chemistry based on a zwitterionic polymer enabling sensitive and specific protein detection in undiluted blood plasma, *Anal. Chem.*, **80**, 7894-7901.
77. Ekbald, T., Andersson, O., Tai, F.-I., Ederth, T. and Liedberg, B. (2009). Lateral control of protein adsorption on charged polymer gradients, *Langmuir*, **25**, 3755-3762.
78. Carrigan, S. D. and Tabrizian, M. (2005). Reducing nonspecific adhesion on cross-linked hydrogel platforms for real-time immunoassay in serum, *Langmuir*, **21**, 12320-12326.
79. Masson, J. F., Battaglia, T. M., Davidson, M. J., Kim, Y. C., Prakash, A. M. C., Beaudoin, S. and Booksh, K. S. (2005). Biocompatible polymers for antibody support on gold surfaces, *Talanta*, **67**, 918-925.
80. Aulasevich, A., Roskamp, R. F., Jonas, U., Menges, B., Dostalek, J. and Knoll, W. (2009). Optical waveguide spectroscopy for the investigation of protein-funcionalized hydrogel films, *Macromol. Rapid Comm.*, **30**, 872-877.
81. Byrne, M. E., Park, K. and Peppas, N. A. (2002). Molecular imprinting within hydrogels, *Adv. Drug Deliver. Rev.*, **54**, 149-161.
82. Byrne, M. E. and Salian, V. (2008). Molecular imprinting within hydrogels II: Progress and analysis of the field, *International Journal of Pharmaceutics*, **364**, 188-212.
83. Raitman, O. A., Chegel, V. I., Kharitonov, A. B., Zayats, M., Katz, E. and Willner, I. (2004). Analysis of NAD(P)(+) and NAD(P)H cofactors by means of imprinted polymers associated with Au surfaces: A surface plasmon resonance study, *Anal. Chim. Acta*, **504**, 101-111.
84. Matsui, J., Akamatsu, K., Nishiguchi, S., Miyoshi, D., Nawafune, H., Tamaki, K. and Sugimoto, N. (2004). Composite of Au nanoparticles and molecularly imprinted polymer as a sensing material, *Anal. Chem.*, **76**, 1310-1315.
85. Matsui, J., Akamatsu, K., Hara, N., Miyoshi, D., Nawafune, H., Tamaki, K. and Sugimoto, N. (2005). SPR sensor chip for detection of small molecules using molecularly imprinted

polymer with embedded gold nanoparticles, *Anal. Chem.*, **77**, 4282-4285.

86. Lavine, B. K., Westover, D. J., Kaval, N., Mirjankar, N., Oxenford, L. and Mwangi, G. K. (2007). Swellable molecularly imprinted polyN-(N-propyl)acrylamide particles for detection of emerging organic contaminants using surface plasmon resonance spectroscopy, *Talanta*, **72**, 1042-1048.
87. Zourob, M. and Goddard, N. J. (2005). Metal clad leaky waveguides for chemical and biosensing applications, *Biosens. Bioelectron.*, **20**, 1718-1727.
88. Tokarev, I., Tokareva, I., Gopishetty, V., Katz, E. and Minko, S. (2010). Specific biochemical-to-optical signal transduction by responsive thin hydrogel films loaded with noble metal nanoparticles, *Adv. Mater.*, **22**, 1412-1416.
89. Stuart, M. A. C., Huck, W. T. S., Genzer, J., Muller, M., Ober, C., Stamm, M., Sukhorukov, G. B., Szleifer, I., Tsukruk, V. V., Urban, M., Winnik, F., Zauscher, S., Luzinov, I. and Minko, S. (2010). Emerging applications of stimuli-responsive polymer materials, *Nat. Mater.*, **9**, 101-113.
90. Endo, T., Ikeda, R., Yanagida, Y. and Hatsuzawa, T. (2008). Stimuli-responsive hydrogel-silver nanoparticles composite for development of localized surface plasmon resonance-based optical biosensor, *Anal. Chim. Acta*, **611**, 205-211.
91. Bjork, P., Persson, N. K., Peter, K., Nilsson, R., Asberg, P. and Inganas, O. (2005). Dynamics of complex formation between biological and luminescent conjugated polyelectrolytes - a surface plasmon resonance study, *Biosens. Bioelectron.*, **20**, 1764-1771.
92. Nilsson, K. P. R. and Inganas, O. (2003). Chip and solution detection of DNA hybridization using a luminescent zwitterionic polythiophene derivative, *Nat. Mater.*, **2**, 419-U10.
93. Nilsson, K. P. R., Andersson, M. R. and Inganas, O. (2002). Conformational transitions of a free amino-acid-functionalized polythiophene induced by different buffer systems, *J. Phys.-Condens. Mat.*, **14**, 10011-10020.
94. Yang, H. H., Liu, H. P., Kang, H. Z. and Tan, W. H. (2008). Engineering target-responsive hydrogels based on aptamer - Target interactions, *J. Am. Chem. Soc.*, **130**, 6320-+.
95. Zhu, Z., Wu, C. C., Liu, H. P., Zou, Y., Zhang, X. L., Kang, H. Z., Yang, C. J. and Tan, W. H. (2010). An aptamer cross-linked hydrogel as a colorimetric platform for visual detection, *Angew. Chem. Int. Edit.*, **49**, 1052-1056.
96. Matsui, J., Takayose, M., Akamatsu, K., Nawafune, H., Tamaki, K. and Sugimoto, N. (2009). Molecularly imprinted nanocomposites for highly sensitive SPR detection of a non-aqueous atrazine sample, *Analyst*, **134**, 80-86.

Chapter 3 Methods and Sample Preparation

3.1 Optical instruments

3.1.1 Prism-coupled SPR and SPFS spectroscopy

A home-built surface plasmon resonance (SPR) instrument in the Kretschmann configuration was used for optical SPR studies. As shown in Figure 3.1, an attenuated total reflection (ATR) method was used for the excitation of prism-coupled SPs on a sensor surface. The beam of a Helium-Neon (HeNe) laser (Uniphase, 5 mW, λ = 632.8 nm) passes through a chopper (frequency = 1331 Hz) that is connected to a lock-in amplifier (EG&G, Model 5210). The modulated beam then passes through two polarizers (Glan-Thompson), by which the intensity and the plane of polarization of the laser can be adjusted. The beam is then reflected off the base of the coupling prism (Schott, LASFN9, n=1.85 @ 633 nm) and is focused by a lens (f = 50 mm, Owis) onto a collection lens and a photo-diode detector, connected to the lock-in amplifier (Model 5210, Princeton Applied Research, USA, integration time 3 seconds). The prism/sample and the photo-detector are mounted on two co-axial goniometers (2-circle 414 with the precision 10^{-3} deg, from Huber AG, Germany) respectively, enabling an independent tuning of respective angular positions. For the prism-coupled SPR measurement, an Au layer on a glass substrate (BK7 or LASFN9) is mounted onto the prism with a drop of matching oil (refractive index n= 1.700, Cargille Laboratories Inc, USA) in between. For the long range surface plasmon resonance (LRSPR), a sensor chip with a layer structure consisted of a low refractive index film (Cytop CTL-809M obtained from ASAHI, Japan) and a gold film with the thicknesses of ~770 nm and ~ 20 nm, respectively, was prepared as described previously.[1]

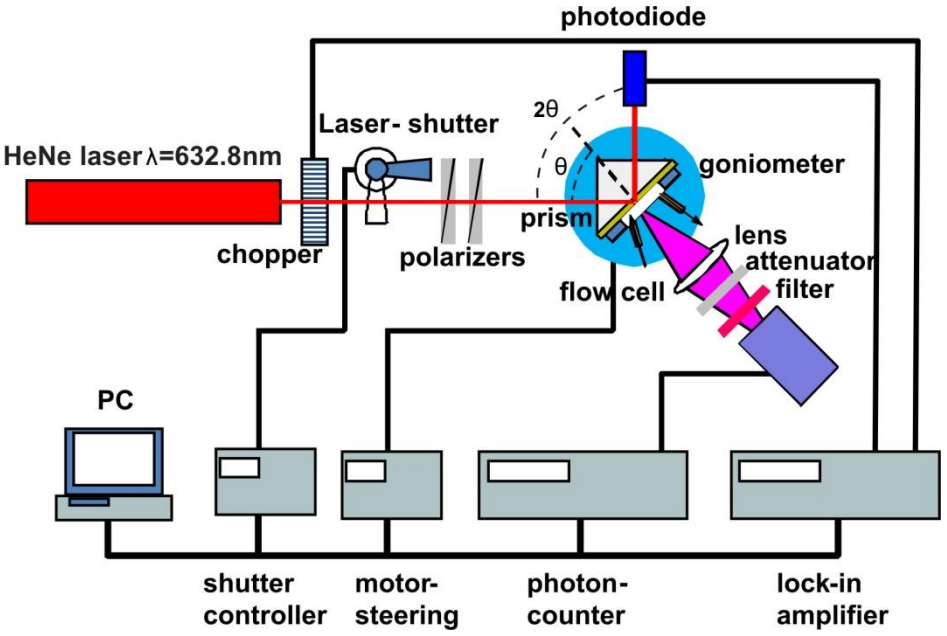

Figure 3.1 Scheme of the SPR and SPFS setup, reproduced from reference [2].

For the SPFS measurement, the fluorescence light emitted from the sensor surface was collected through the flow-cell by a lens (numerical aperture NA = 0.3), passed through a band-pass filter (transmission wavelength of λ = 670 nm) and its intensity was detected by a photomultiplier tube (PMT) from Hamamatsu (H6240-01, Japan), which is connected with a photo counter and the computer. A programmable shutter is installed such as to constantly block the laser (typically 5s on and 60s off for the shutter, when kinetic measurement was employed), thus minimizing the photo-bleaching effect of the fluorescent dyes.

A flow-cell made of PDMS spacer with a volume of approximately 12 µL was mounted against the sensor surface. Aqueous samples (with a refractive index close to n_d = 1.333) were pumped through the flow-cell using a peristaltic pump. The analyzed samples circulated in the fluidic system with a total volume of 800 µL. Tubings with innerdiameter of 0.76 mm (Tygon R3607) were connected with the flow-cell.

For the kinetic measurement, the monitoring of reflectivity changes R at an angle of incidence θ set to the maximum slope of the dip associated with the resonant excitation of SPs, as shown in Figure 3.2. The reflectivity increases with the resonant angle shifting to high angle. The electronics supporting the sensor system was controlled by using the software Wasplas developed at the Max Planck Institute for Polymer Research in Mainz (Germany). The measured reflectivity curves were fitted by the transfer matrix-based

model implemented in the software Winspall developed at the Max Planck Institute for Polymer Research in Mainz (Germany). By using this model, the thickness *d* and the refractive index *n* of the binding layers were determined by fitting the resonant angles for the excitation of SPs.

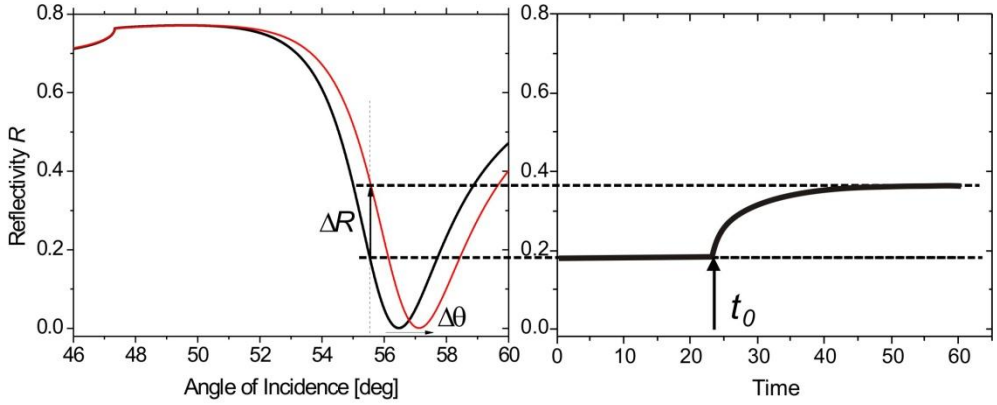

Figure 3.2 SPR angular spectra associated with kinetic measurement.

3.1.2 Grating-coupled SPR for magnetic nanoparticle immunoassay

The grating-coupled SPR was employed in this study for the magnetic nanoparticles immunoassay. The optical setup was the same as the one for prism-coupled SPR described above. In this setup a sample holder was modified as indicated in Figure 3.3. The laser was incident directly on the grating sensor surface at the incident angle θ. In order to apply a magnetic field on the sensor surface, a magnet was placed under the substrate at the distance around 2-3 mm away from the sensor surface.

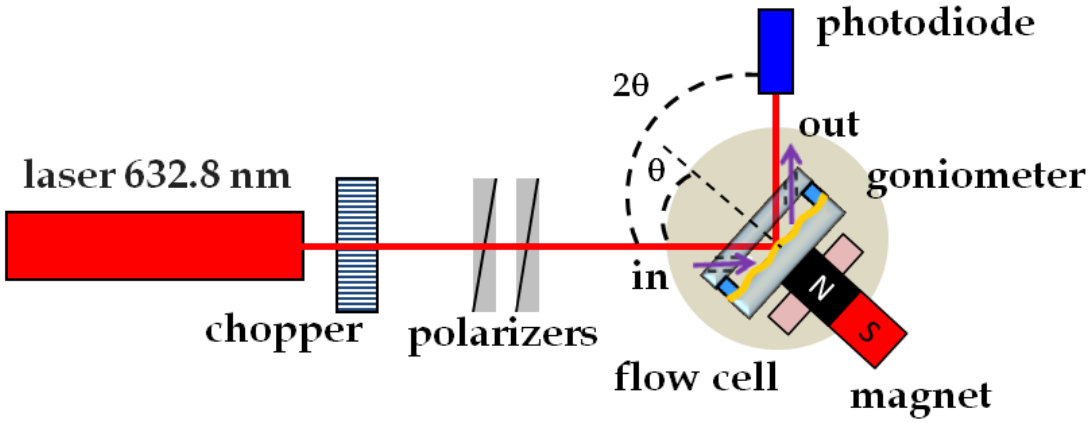

Figure 3.3 Schematic setup for the grating-coupled SPR with applied magnet.

3.2 Substrates preparation

3.2.1 Preparation of grating

3.2.1.1 Preparation of grating master

In this work, we used grating masters prepared by holographic method by Raquel Chuli á-Jordan in the clean room in Max-Planck Institute for Polymer Research in Mainz, Germany. A substrate with a photoresist layer was mounted in the optical setup that is depicted in Figure 3.4. The beam of a TE-polarized He-Cd laser (λ_{HeCd} = 442 nm, Optilas) is passing through a spatial filter which produces a parallel beam which does not show significant variation in intensity in the vicinity of the optical axis over an area of a few cm^2. While one half of the beam is incident directly on the substrate, the other half is reflected by a mirror. Depending on the phase difference between these two possible paths, either constructive or destructive interference occurs on the substrate surface. The intensity distribution on the grating surface is sinusoidal with a period Λ that is determined by the tilt angle α between the optical axis and the surface normal:

$$\Lambda = \frac{\lambda_{HeCd}}{2\sin(\alpha)}. \tag{3.1}$$

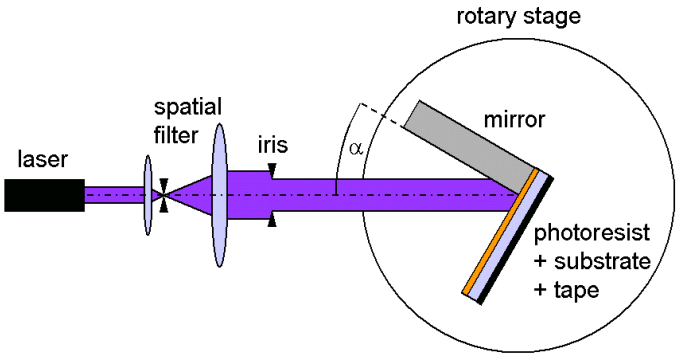

Figure 3.4 Holographic grating manufacture. Gratings were manufactured from a photoresist film by exposure to an interference pattern generated from the superposition of a HeCd laser beam and its reflection off a mirror.

An exposure of a positive photoresist to the laser light induces a photochemical reaction in the photoresist that promotes solubility in the developer solution. The remaining unilluminated material remains insoluble. According to the sinusoidal intensity profile of the interference pattern, solubility was periodically introduced in the film.

Immersion in the developer reagent translates the solubility contrast into a surface grating by solving the illuminated regions. Excess developer was removed by rinsing with purified water. The remaining photoresist regions were cured by heating which activates a thermoinitiator in the material, facilitating cross-linking.

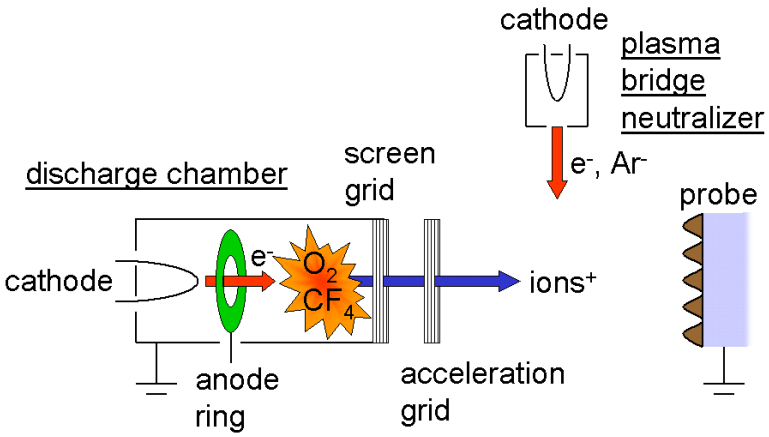

Figure 3.5 Scheme of reactive ion beam etching.

The grating structure was then transferred into the hard silicon substrate by using reactive ion beam etching (RIBE). The working principle of the RIBE system (RR-I SQ76, Roth & Rau) is sketched in Figure 3.5. Electrons are ejected from the cathode and collided with gas molecules of O_2 and CF_4, and the cathode beam strips them of electrons and ionizes them. Positive ions pass through the grid and hit the sample perpendicularly as a parallel beam with a diameter of about 7 cm. The plasma etches into the sample in two ways: first, the pure bombardment of ions ablates the material. Additionally, radicals from the plasma chemically decompose both photoresist and glass. The difference in etching rates between photoresist and glass is about a ratio of 2:1.

3.2.1.2 Soft lithography for replication of grating master

In order to reuse the master as many times as possible, the grating masters were replicated by soft lithography as shown in Figure 3.6. PDMS (Dow-Corning Corporation, Sylgard 184) solution was poured and cured at 60 ℃ overnight on the silica grating master surface. The elastomeric PDMS stamp is then peeled off from the master surface. UV curable polymer (NOA 72, Norland Inc. USA) was dropped on a glass or silica substrate, the PDMS stamp was placed on its top, and the NOA 72 polymer was cured through UV light at 90 mW for 90 min. Afterwards, the PDMS stamp was released from the surface. The substrate was then ready for the coating with metal layers such as gold.

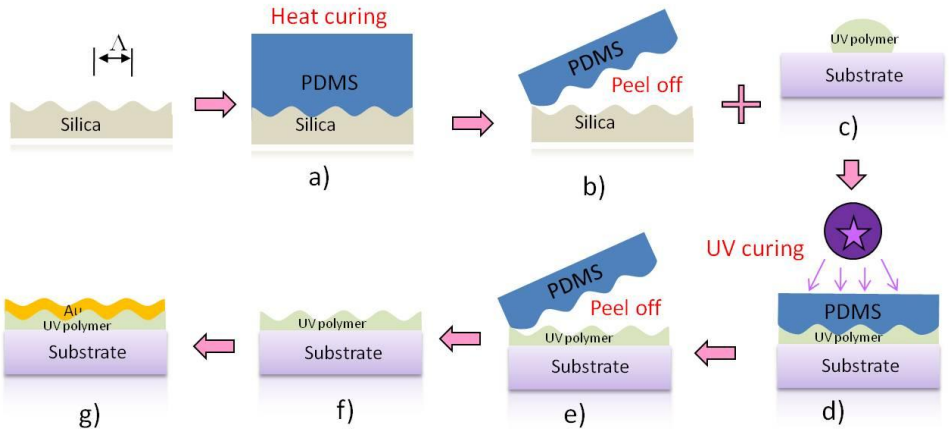

Figure 3.6 Scheme of replication of grating master, a) heat curing of PDMS, b) peel off PDMS to get replication of grating on PDMS surface, c) drop UV curable polymer (such as NOA72) solution on a glass or silica substrate, d) place PDMS grating onto UV polymer surface and cured by UV light, e) peel off PDMS, f) replica of grating on UV polymer surface, g) Au surface was deposited on the polymer surface.

3.2.2 Metallic film deposition

The deposition of metallic layers was performed by using the magnetron sputtering (UNIVEX 450C from Leybold Systems, Germany). It relies on physical vapor deposition (PVD) based on sputtering of a material from a "target" to a "substrate". The sputtering process in principle works as shown in the Figure 3.7. Typically, a substrate is placed in a vacuum chamber opposite to a target. The chamber is evacuated and then backfilled with a process gas (Argon) that is ionized. The positive charged ions are strongly attracted to the target, which carries a negative charge. As the relatively large argon ions impact the target, atoms/molecules of target material are physically removed and land on the substrate. Magnetron sputtering cathodes use powerful magnets to confine the plasma to the region closest to the 'target'. This condenses the ion-space ratio, increases the collision rate, and thus improves deposition rate.

BK7 or LaSFN9 glass substrates were cleaned by sonication in 1% Hellmanx solution, followed by ethanol and dried with air gun. The thickness of the metallic layer was controlled by the sputtering time. All of the metallic layers were sputtered on a static stage under 20 W of power, ~ 300 V of voltage, 2 μbar of pressure and 6 sccm of argon

flow rate. The parameters including the sputtering time and voltage were summarized in Table 3.1.

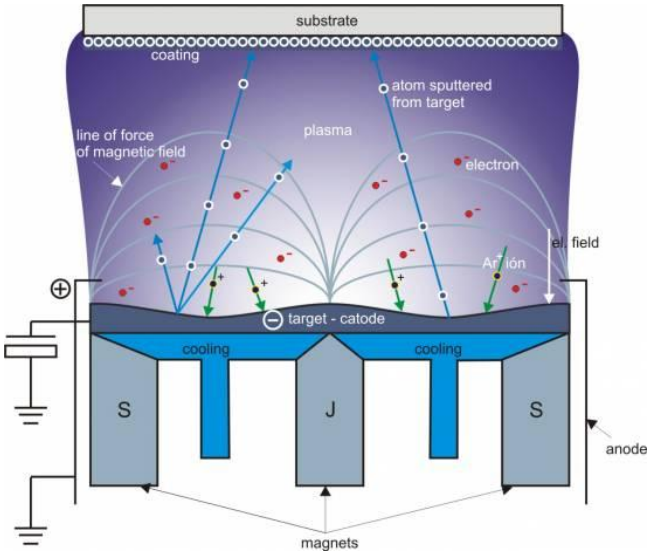

Figure 3.7 Principle of magnetron sputtering [3].

Table 3.1 The thickness of metallic layers and used parameters for preparation of samples for the excitation of surface plasmon modes.

		Metallic layer	Thickness	Sputtering power (W)	Sputtering time	Sputtering speed
Prism-coupled SPR	BK7 glass	1. Ta	0.67 nm	20/20	10 s	~0.067 nm/s
		2. Au	45-50 nm	21/23	150 s	~0.305 nm/s
	LaSFN9 glass	Au	45-50 nm	21/23	150 s	~0.305 nm/s
Grating-coupled SPR		Au	60 nm	21/23	196 s	~0.305 nm/s
Long range SPR		Au	16-20 nm	21/23	65 s	N&A

3.3 Surface functionalization

3.3.1 Self-assembled monolayer

Self-assembled monolayers (SAMs) are organic layers which are formed when surfactant molecules spontaneously adsorb and assemble on a surface. These molecules consist of three different parts: the headgroup (linking group), the backbone (main chain),

and the specific terminal (active) group, as shown in Figure 3.8. The headgroup guides the self-assembly process on each type of substrate, linking the hydrocarbon chain (of variable length) to the metal surface through a strong bond. The interactions among backbone hydrocarbon chains (involving van der Waals and hydrophobic forces) ensure an efficient packing of the monolayer and stabilization of the structures. The terminal group confers specific properties to the surface (hydrophilic, hydrophobic), and can also be used to anchor different molecules, biomolecules, or nanostructures by weak interactions or covalent bonds. There are a number of headgroups that bind to specific metals, metal oxides, and semiconductors. The most extensively studied class of SAMs is derived from the adsorption of alkanethiols on gold[4-6],silver[7],copper[7], palladium[8] and so on.

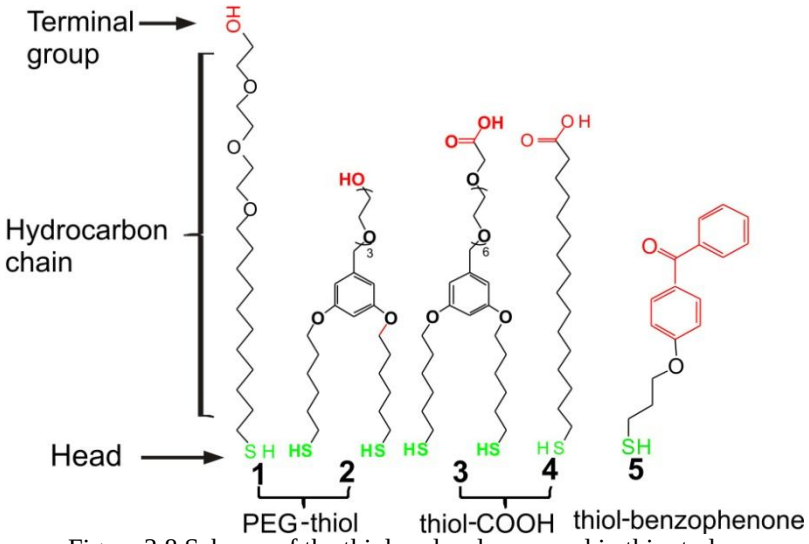

Figure 3.8 Scheme of the thiol molecules as used in this study.

In this study, various thiol molecules with different terminal groups (Figure 3.8), including PEG thiol (**1**, **2**), thiol-COOH (**3**, **4**) and thiol-benzophenone (**5**), were used. Typically, the SAM was prepared by immersing fresh prepared Au substrates in a mixed thiol solution at 1 mM total concentration in ethanol (e.g. 0.09 mM PEG thiol and 0.01 mM thiol-COOH) for at least 24 h. The substrates modified with SAM were than dried with air and stored in Ar. The study on the stability of SAM shows that the mixed SAMs stored in air or N_2 are stable and retain their biosensor properties for at least 30 days, while ethanol appeared to be the worst storage medium due to partial oxidation of the thiol headgroup[9].

3.3.2 Hydrogel thin layer

In this study, there were used PNIPAAm and dextran hydrogel that were synthesized by Alena Aulasevich and Annette Brunsen, respectively (at Max-Planck Institute for Polymer Research, Mainz). These hydrogel polymers were synthesized to carry two functional groups: i) the benzophenone groups which offers the photo-crosslinking function, ii) the carboxylic groups which serve the chemical immobilizations of proteins and ligands (Figure 3.9). Photo-crosslinked hydrogel thin film with thicknesses from hundreds nanometers to several micrometers was prepared. Typically, an Au substrate was immersed into a thiol-benzophenone (**5** in Figure 3.8**)** ethanol solution at the concentration of 1 mM overnight to form a functionalized thiol SAM terminated with a cross-linker group, as shown in Figure 3.9. After dried in N_2 stream, the polymer (i.e. poly(*N*-isopropylacrylamide) (PNIPAAm), dextran-based copolymers) at concentration 5-40 mg/ml (dissolved in ethanol for PNIPAAm and water for dextran-based copolymer) was spin-coated on the substrates. Then, the films were dried in oven at 45 ℃ for 5 h and irradiated by UV-light. The density and thickness of the hydrogel was controlled by the spin-coating rate, the concentration of polymer used in spin-coating and UV-light irradiation dose. During the irradiation of UV-light at wavelength λ=254 nm (power of 2 mW/cm^2), the C=O bonds of benzophenone were broken up and inserted into C-H group, as shown in Figure 3.9.

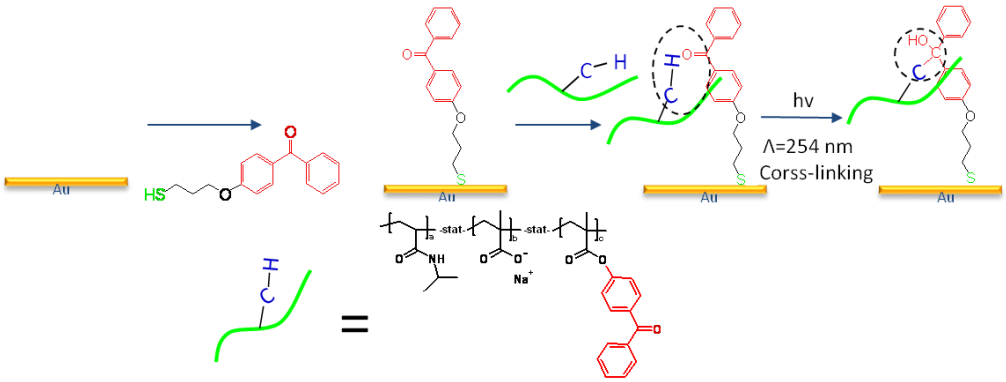

Figure 3.9 Scheme of surface modification of gold with PNIPAAm hydrogel.

3.3.3 Immobilization of ligands and proteins

There are several methods used to immobilize proteins and ligands on functionalized surfaces, including those based on the coupling of -NH_2 groups of proteins to the -COOH

group on a surface, the -SH/-SH covalent binding, and via the -COOH group of proteins with the -NH_2 groups on the sensor surface. In this study, the EDC/NHS coupling chemistry was used to couple the -NH_2 groups of proteins with the -COOH groups on a SAM surface or in a hydrogel thin film. For the PNIPAAM hydrogel, the coupling chemistry EDC/TFPS (Sodium *para*-tetrafluorophenol-sulfonate) was used as shown in Figure 3.10.

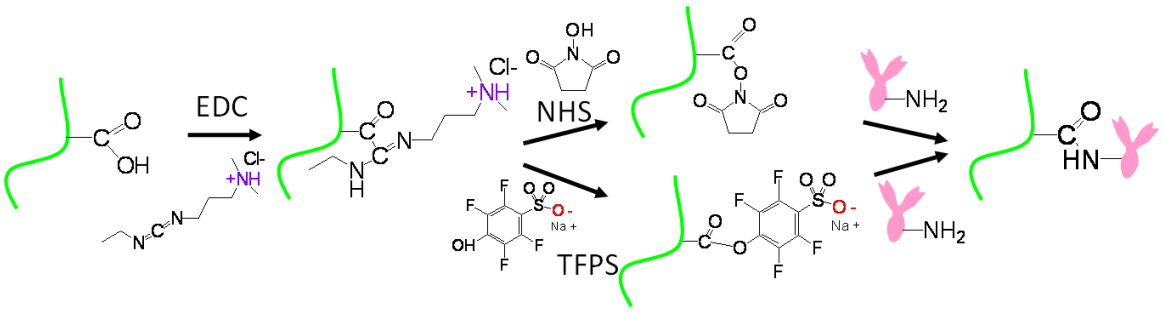

Figure 3.10 Scheme of the amine coupling of ligands by EDC/NHS and EDC/TFPS esters.

3.4 Protein labeling

3.4.1 Chromophore labeling

Basically, three steps are required in the protein labeling procedure: 1) Reaction with dyes carrying reactive group, usually a succinimidyl ester (amine-reactive) or maleimide (thiol-reactive), as shown in Figure 3.11. 2) Purification of the labeled protein, usually by a gel-filtration column or dialysis. 3) Determination of the degree of labeling by UV absorbance of proteins and dyes, respectively.

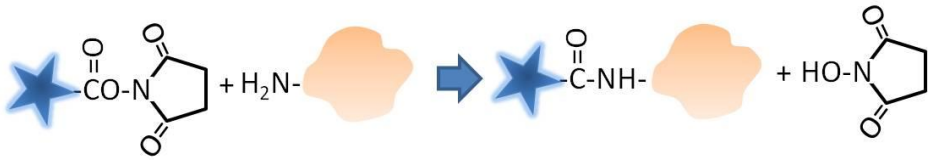

Figure 3.11 Scheme of the labeling of protein with Alexa Fluor 647 dye with a succinimidyl ester moiety.

For our experimental conditions (e.g. using the wavelength @ 633 nm as the excitation source), the commercial Alexa Fluor 647 dye (abbreviated as AF 647, A-20186, from Molecular Probes, Inc.) was used taking advantage of its high fluorescence yield. The

commercial labeling kit contains things needed to perform labeling reactions as well as to purify the resulting conjugates. In the kit, the AF 647 dye contains a succinimidyl ester moiety that reacts efficiently with primary amines of the protein to form stable dye-protein conjugates at pH 7.5-8.5. The experimental protocol for labeling 100 μg monoclonal antibody is as the following:

1) Prepare 1 mg mL^{-1} antibody solution with sodium bicarbonate buffer (100 mM, pH 8.3)

2) Transfer 100 μL of the antibody solution to the vial of reactive dye. Cap the vial and gently invert it a few times to fully dissolve the dye. Incubate the solution for 1 hour at room temperature. Every 10-15 minutes, gently agitate the vial several times to mix the two reactants and increase the labeling efficiency.

3) Prepare the spin column by adding the resin (30 kDa size exclusion) suspension into the column and allow it to settle, until the bed volume reaches 1.5 mL.

4) Centrifuge the column for 3 minutes at 1100 × g using a swinging bucket rotor. To convert revolutions per minute (rpm) into relative centrifugal force (g-force), use the following equation:

$$\text{Relative centrifugal force} = (1.12 \times 10^{-5})\,(\text{rpm})^2\,(\text{radius}), \tag{3.2}$$

where radius in centimeters is measured from the center of the centrifuge spindle to the bottom of the rotor bucket.

5) Load the 100 μL reaction volume dropwise onto the center of the column, allowing the solution to adsorb into the gel bed.

6) Place the column into a collection tube and centrifuge for 5 minutes at 1100 × g. The collection tube then contains labeled protein in ca. 100-150 μL of PBS, pH 7.2, with 2 mM sodium azide.

7) Dilute a small amount of the purified conjugate into suitable buffer and measure the absorbance in a cuvette with a 1 cm pathlength at both 280 nm (A_{280}) and 650 nm (A_{650}).

$$\textbf{The protein concentration } (\mathbf{M}) = \frac{(A_{280} - (A_{650} \times 0.03)) \times dilution\_factor}{203{,}000}, \tag{3.3}$$

where 203,000 is the molar extinction coefficient in $cm^{-1}M^{-1}$ of a typical IgG at 280 nm and 0.03 is a correction factor for the contribution of the fluorophore to the absorbance at 280 nm. The degree of labeling, i.e., dye-to-protein ratio (abbreviated as D/P ratio) is:

$$D/P = \frac{A650 \times dilution\_factor}{239,000 \times protein\_concentration(M)}, \tag{3.4}$$

where 239,000 $cm^{-1}M^{-1}$ is the approximate molar extinction coefficient of the Alexa Fluor 674 dye at 650 nm.

3.4.2 Magnetic nanoparticles labeling

Magnetic nanoparticles (fluidMAG-ARA, from Chemicell Corp., Berlin, Germany) coated with polysaccharide (Figure 3.12) with diameter of 200 nm were modified with antibodies against to βhCG, based on the EDC/NHS coupling chemistry as shown in Figure 3.10, according to the protocol from Chemicell Corp. with some modifications.

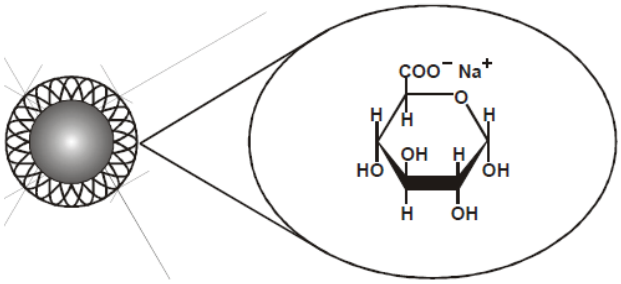

Figure 3.12 Scheme of fluidMAG-ARA magnetic nanoparticle

1) Wash the fluidMAG-ARA particles (20 mg) 2 × with 1 ml MES buffer by using cylindrical NdBFe magnet (diameter of 20 mm, length of 45 mm). The 0.1 M 2-(N-Morpholino)ethanesulfonic acid (MES) buffer (195.2 mg dissolved in 10 ml miliQ water), pH 5.0 was adjusted by adding NaOH.

2) After the second wash step, resuspend the magnetic particles in 0.3 ml MES buffer.

3) Dissolve 11 mg EDC and 11 mg NHS in 0.5 ml MES buffer. Add freshly prepared EDC/NHS to the particles and mixed gently for 10 minutes at room temperature.

4) After incubation, wash the particles 2 × with 1 ml MES buffer and resuspend the activated particles in 0.3 ml MES buffer.

5) Add proteins (e.g.100 μg protein) to the activated particles and mixed the suspension gently for two hours at room temperature.

6) Wash the particles 3 × with 1 ml PBST buffer (PBS buffer with 0.05% Tween 20).

7) Deactivate the particles by incubating the particles in 1 ml 1M ethanolamine, pH 8 .5 for 10 min.

8) Wash the particles 2 × with 1 ml PBST buffer, and resuspend in 0.5 ml PBST.

References

1. Dostalek, J., Kasry, A. and Knoll, W. (2007). Long range surface plasmons for observation of biomolecular binding events at metallic surfaces, *Plasmonics*, **2**, 97-106.
2. Yu, F., Yao, D. F. and Knoll, W. (2003). Surface plasmon field-enhanced fluorescence spectroscopy studies of the interaction between an antibody and its surface-coupled antigen, *Analytical Chemistry*, **75**, 2610-2617.
3. [cited 2010]; Available from: http://www.umms.sav.sk/index.php?ID=415.
4. Poirier, G. E. and Pylant, E. D. (1996). The self-assembly mechanism of alkanethiols on Au(111), *Science*, **272**, 1145-1148.
5. Dubois, L. H. and Nuzzo, R. G. (1992). Synthesis, Structure, and Properties of Model Organic-Surfaces, *Annual Review of Physical Chemistry*, **43**, 437-463.
6. Hara, M., Sasabe, H. and Knoll, W. (1996). Ordered nucleation of a self-assembled monolayer on Au(111) studied by scanning tunneling microscopy, *Thin Solid Films*, **273**, 66-69.
7. Laibinis, P. E., Whitesides, G. M., Allara, D. L., Tao, Y. T., Parikh, A. N. and Nuzzo, R. G. (1991). Comparison of the Structures and Wetting Properties of Self-Assembled Monolayers of Normal-Alkanethiols on the Coinage Metal-Surfaces, Cu, Ag, Au, *Journal of the American Chemical Society*, **113**, 7152-7167.
8. Love, J. C., Wolfe, D. B., Haasch, R., Chabinyc, M. L., Paul, K. E., Whitesides, G. M. and Nuzzo, R. G. (2003). Formation and structure of self-assembled monolayers of alkanethiolates on palladium, *Journal of the American Chemical Society*, **125**, 2597-2609.
9. Jans, K., Bonroy, K., De Palma, R., Reekmans, G., Jans, H., Laureyn, W., Smet, M., Borghs, G. and Maes, G. (2008). Stability of mixed PEO-thiol SAMs for biosensing applications, *Langmuir*, **24**, 3949-3954.

Chapter 4 Long Range Surface Plasmon-Enhanced Fluorescence Spectroscopy for the Detection of Aflatoxin M_1 in Milk

Abstract

A novel biosensor for the highly sensitive detection of aflatoxin M_1 (AFM_1) in milk was developed. This biosensor is based on surface plasmon-enhanced fluorescence spectroscopy (SPFS) which was advanced through the excitation of long range surface plasmons (LRSPs). In SPFS, the binding of fluorophore-labeled molecules to the sensor surface is probed with surface plasmons (SPs) and the emitted fluorescence light is detected. This approach takes advantages of the enhanced intensity of electromagnetic field occurring upon the resonant excitation of SPs which directly increases the fluorescence signal. LRSPs are special surface plasmon waves propagating along thin metal films with orders of magnitude lower damping than conventional SPs. Therefore, their excitation on the sensor surface provides a larger field intensity enhancement and provides further increased fluorescence signal. For the detection of AFM_1, LRSP-enhanced fluorescence spectroscopy was combined with an inhibition immunoassay in which a derivative of AFM_1 was immobilized on the sensor surface and antibodies against AFM_1 were used as recognition elements. The developed biosensor allowed for the detection of AFM_1 in milk within 53 min at concentrations as low as 0.6 pg mL^{-1}. The achieved limit of detection was about two orders of magnitude lower than the maximum AFM_1 residue level in milk stipulated by the European Commission legislation.

4.1 Introduction

Aflatoxins are a class of mycotoxins produced mainly by *Aspergillus flavus* and *Aspergillus parasiticus* which grow in a number of agricultural products. Aflatoxin M_1 (AFM_1) is the hydroxylated metabolite of aflatoxin B_1 (AFB_1) and can be found in urine, blood, milk, and internal organs of animals that have ingested AFB_1-contaminated feed.

Due to its hepatotoxic and carcinogenic effects [1] and the relative stability during pasteurization or other thermal treatments [2], control measurements were established. For instance, the European Commission stipulates the maximum level of 50 pg mL^{-1} for AFM_1 in milk (Commission Regulation, 2001).

Currently, routine analysis of aflatoxin-contaminated samples is mostly performed by high-performance liquid chromatography (HPLC) [3], thin-layer chromatography (TLC) [4], and enzyme-linked immunosorbent assay (ELISA) [5]. However, these techniques require highly-trained personnel in specialized laboratories, extensive preparation steps and they are time-consuming. Therefore, research has been carried out to simplify and expedite the detection of aflatoxins over the last years. The majority of novel approaches relies on immunoassays combined with electrochemical [6, 7], scanning densitometry [8], colorimetric [9], chemiluminescent [10], fluorescence [11] and surface plasmon resonance [12, 13] transducers.

Biosensors based on surface plasmon resonance (SPR) are gaining increasing popularity for the detection of chemicals and biological species [14]. In these devices, the specific capture of target molecules contained in a liquid sample by biomolecular recognition elements anchored to the metallic sensor surface is probed with surface plasmon waves. The binding of target molecules induces an increase in the refractive index on the sensor surface which can be directly measured by spectroscopy of SPR. However, for the detection of extremely low analyte concentrations or small molecules, the induced refractive index changes are too low to be measured directly. Therefore, SPR biosensors have been combined with fluorescence spectroscopy in a new method referred as to surface plasmon-enhanced fluorescence spectroscopy (SPFS) [15]. In SPFS, fluorophore-labeled molecules captured on the sensor surface are excited with surface plasmons (SPs) and the emitted fluorescence light is measured. This approach takes advantages of the enhanced intensity of the electromagnetic field occurring upon the resonant excitation of SPs which greatly increases the strength of the fluorescence signal.

Recently, long range surface plasmons (LRSPs) were introduced to SPR-based biosensors [16-20]. LRSPs are special surface plasmon modes which propagate along a thin metal film suspended between two dielectrics with similar refractive indices [21]. Compared to conventional SPs, LRSPs exhibit a greatly reduced damping and thus their excitation is accompanied with a stronger enhancement of the electromagnetic field intensity. This feature enables to further increase the fluorescence signal in SPFS-based detection [17, 20].

In this chapter, we report the implementation of LRSP-enhanced fluorescence spectroscopy in an immunoassay-based biosensor for the highly sensitive detection of AFM_1 in milk samples.

4.2 Materials and Methods

4.2.1 Materials

All reagents were used as received without further purification. 16-Mercaptohexadecanoic acid (MHDA, 90%), (11-Mercaptoundecyl)tri(ethylene glycol) (MUTEG, 95%), *N*,*N*,*N*',*N*'-Tetramethyl-*O*-(*N*-succinimidyl)uronium tetrafluoroborate (TSTU, ≥98.0%), *N*,*N*-Dimethylformamide (DMF, 99.8%), aflatoxin M_1 (AFM_1), and the conjugate of AFM_1 with bovine serum albumin (AFM_1-BSA) were purchased from Sigma-Aldrich (Steinheim, Germany). The monoclonal rat antibody against AFM_1 (a-AFM_1, class IgG2b) and Cy5-labeled goat anti-rat antibody (Cy5-GaR, approximately 10.2 dyes per antibody) were obtained from Acris Antibodies Gmbh (Herford, Germany). Glycine buffer with a pH of 1.5 and ethanolamine were purchased from Biacore (Freiburg, Germany). Tween 20 was purchased from Serva GmbH (Heidelberg, Germany). The experiments were performed in phosphate-buffered saline at pH 7.4 containing 0.05% Tween 20 (PBS-T). Samples were prepared by dissolving a milk powder (fat content of 30%) in deionized water at the concentration of 0.1 g mL^{-1}.

4.2.2 Sensor implementation

In the experiment, we used a sensor instrument for the excitation of LRSPs and for the detection of fluorescence light as described in the section 3.1.1. The instrument utilizes the angular spectroscopy of LRSPs in the total attenuated reflection (ATR) method of the Kretschmann configuration, as shown in Figure 4.1. This layer structure consisted of a low refractive index buffer layer (Cytop, refractive index and thickness of n = 1.340 and d = 800 nm, respectively) and a gold film on the top (thickness of d = 20 nm). To the sensor chip, a transparent flow-cell with the volume of approximately 12 μL was fixed. Aqueous samples (with a refractive index close to n = 1.333) were pumped through the flow-cell

using a peristaltic pump at the flow rate of 0.5 mL min^{-1}. The volume of analyzed samples which circulated within the fluidic system was V = 800 μL.

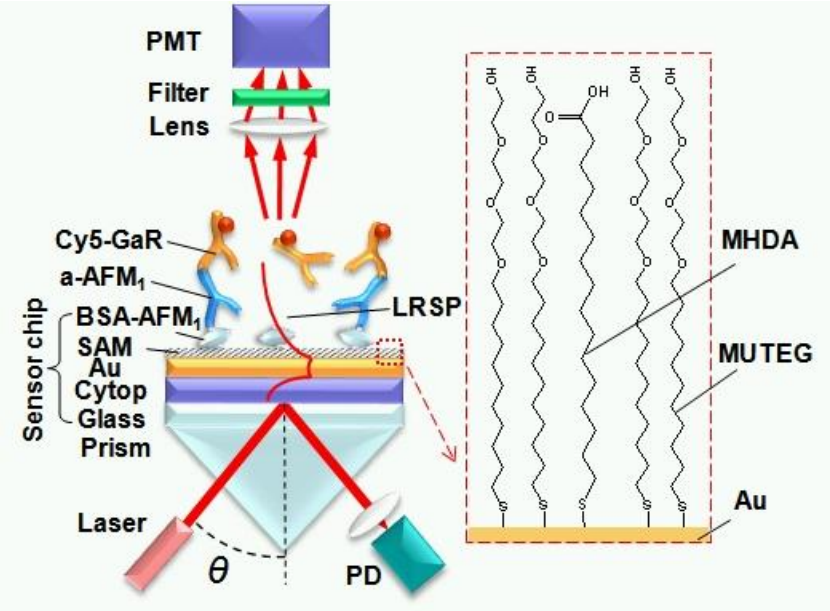

Figure 4.1 The schematic drawing of the setup utilizing LRSP-enhanced fluorescence spectroscopy and the interfacial molecular architecture for the detection of AFM_1 by an inhibition immunoassay.

4.2.3 Sensor chip functionalization

As the Figure 4.1 shows, the gold surface of the sensor chip was modified with a mixed thiol self assembled monolayer (SAM) to which the AFM_1-BSA conjugate was coupled. Firstly, the sensor chip was immersed in a 9:1 mixture of MUTEG and MHDA dissolved in ethanol (net thiol concentration of 1 mM) overnight at room temperature. Subsequently, the sensor chip was successively rinsed with ethanol and water and dried in a stream of nitrogen. The MHDA carboxylic groups were used to anchor AFM_1-BSA conjugates and tri(ethylene glycol) groups of MUTEG chains provided a non-fouling background [22]. The carboxylic terminal groups were activated by immersing the chip in TSTU dissolved in DMF (1 mg mL^{-1}) for 2 hours (Figure 4.2). Afterwards, the chip was rinsed with water and dried in a nitrogen stream. Then, AFM_1-BSA conjugate (1 mg mL^{-1} in PBS) was dropped on the surface, covered with a glass side and incubated overnight at the temperature of 4 ℃. Finally, the sensor chip was rinsed with water, dried in the nitrogen stream and stored at 4 ℃. Prior the use, the unreacted active ester groups were blocked by 3-min incubation in ethanolamine (1 mM and pH = 8.5).

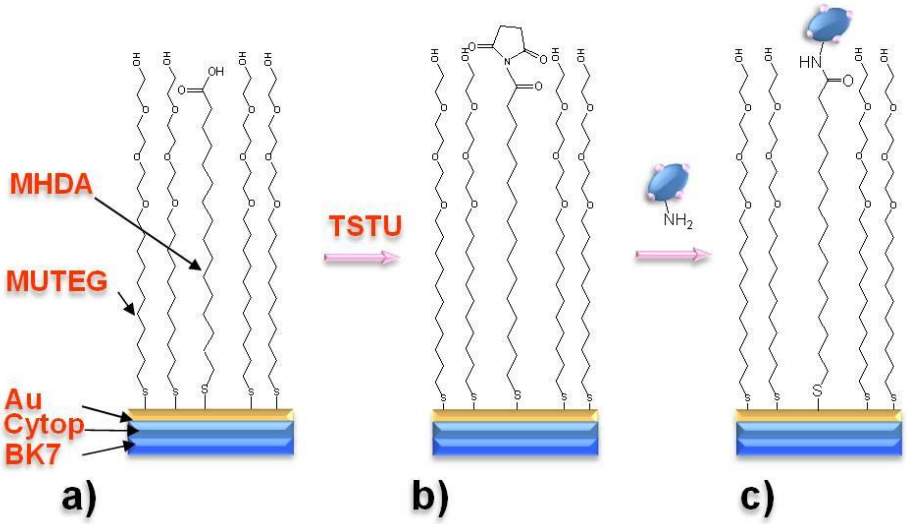

Figure 4.2 Modification of Au sensor surface with a) mixed thiol SAM consisting of thiol-EG and carboxyl group terminated (ratio 9:1), b) activation of carboxyl groups, c) coupling of the conjugate of BSA and AFM1 via its amino groups.

4.2.4 Detection format

For the detection of AFM_1, an inhibition immunoassay was used. In this assay, the analyzed samples were incubated with a-AFM_1 antibody (concentration of 100 ng mL^{-1}) for 15 min followed by the detection of the amount of unreacted a-AFM_1 antibody. The mixture a-AFM_1 antibody with a sample was pumped through the sensor instrument for 10 min to let the free a-AFM_1 bind the surface with immobilized BSA-AFM_1 conjugate. Afterwards, the sensor surface was washed with PBS-T buffer for 3 min and the labeled Cy5-GaR antibody (at a concentration of 1 µg mL^{-1}) was pumped through the sensor for 10 min. Finally, the sensor surface was washed for 5 min with PBS-T buffer and the fluorescence signal owing to the binding of Cy5-GaR to the captured a-AFM_1 was measured. The concentrations of a-AFM_1 and Cy5-GaR antibodies were chosen so as to provide the fluorescence signal for a blank sample (not spiked with AFM_1) of about 5×10^4 counts per second (cps) which was about 400 times higher than the standard deviation of the background signal. After each detection cycle, the sensor surface was regenerated by 5-min incubation in glycine buffer (pH = 1.5) followed by 20-min incubation in 100 mM sodium hydroxide.

For the calibration of the developed biosensor, a series of samples (in milk and PBS-T buffer) with concentrations of AFM_1 ranging from 10^{-2} to 10^4 pg mL^{-1} were prepared by spiking from a AFM_1 stock solution (AFM_1 was dissolved at a concentration of 10 μg mL^{-1} in a mixture 90:10 (v/v) of PBS and methanol). Milk samples containing AFM_1 were centrifuged at 5000 rpm for 10 min at the temperature of 4 ℃, the upper fat layer was removed and the obtained supernatant was used for the further analysis.

4.3 Results and Discussion

Figure 4.3A shows the angular reflectivity and fluorescence spectra measured before and after the analysis of a PBS-T buffer sample spiked with AFM_1 at a concentration of 1 pg mL^{-1}. It reveals that the excitation of LRSPs is manifested as a resonant dip in the angular reflectivity spectrum and that the fluorescence light reaches its maximum intensity at the virtually identical angle for which LRSPs are resonantly excited. At this angle of incidence, the maximum enhancement of the electromagnetic field intensity occurs and thus the strongest excitation of captured chromophores is seen. In further experiments, the angle of incidence was fixed in the vicinity if the resonance (θ = 48.9 deg) and the fluorescence signal F was measured as a function of time. Figure 4.3B shows the typical time evolution of the fluorescence signals measured upon the analysis of milk samples spiked with AFM_1 at concentrations of 0, 1, 10, 10^2 and 10^3 pg mL^{-1}. Samples incubated with a-AFM_1 were pumped through the sensor (t = 0-10 min) followed by the washing step with buffer (t = 10-13 min), flow of labeled antibody Cy5-GaR (t = 13-23 min) and the washing with buffer (t = 23-28 min). The sensor response ΔF was determined as the difference between the fluorescence signal before the sample injection (t = 0) and after the final washing step with the buffer (t = 28 min). The measurements were performed in cycles and after each analysis the sensor surface was regenerated. We found that after 30 detection cycles measured over 4 days no significant changes in the sensor response occurred.

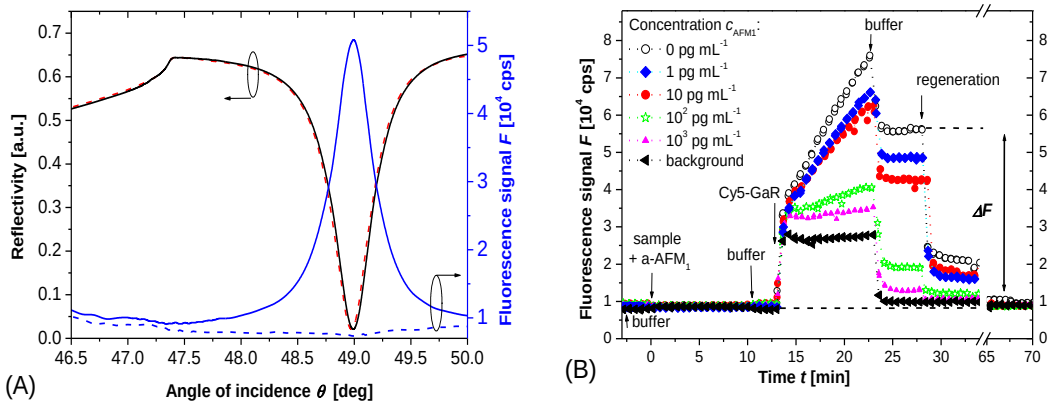

Figure 4.3 (A) Angular spectra of reflected intensity (wavelength of λ = 632.8 nm) and fluorescence intensity (wavelength λ = 670 nm) measured before (dashed line) and after (solid line) the analysis of a buffer sample spiked with AFM_1 at a concentration of 1 pg mL^{-1} AFM_1. (B) Time evolution of the maximum fluorescence intensity *F* upon the analysis of a series of milk samples with AFM_1 at concentrations from 0 to 10^3 pg mL^{-1} (concentration indicated in the graph). In addition, the response due to nonspecific binding of Cy5-GaR antibody to the surface without a-AFM_1 antibody is shown (noted as background).The sensor response was measured for series of buffer and milk samples spiked with AFM_1 at concentrations ranging from 10^{-2} to 10^4 pg mL^{-1}.

Figure 4.4 shows the obtained calibration curves normalized with the sensor response for the blank samples (not spiked with AFM_1). It shows that the sensor response ΔF gradually decreased when increasing the concentration of AFM_1 in the sample attributed to the blocking of a-AFM_1 binding sites. For each concentration, the sensor response was measured in triplicate and the standard deviation was determined (shown as the error bar). The standard deviation of the sensor response measured for blank samples was 3%. The background response due to non-specific binding of Cy5-GaR to the surface was 1.8% and 6.2% for buffer and milk samples, respectively. The approximately three fold higher background response observed in milk samples was probably due to the non-specific adsorption of milk compounds to the surface. The measured calibration curves were fitted with a sigmoidal function and the limit of detection (LOD) was determined as the concentration for which the normalized sensor response decreases by three times the standard deviation (9%) with respect to that for blank samples. For the buffer and milk samples, the LOD was determined as 0.4 pg mL^{-1} and 0.6 pg mL^{-1}, respectively. The maximum detectable concentration (MDC) was 1.8×10^3 pg mL^{-1} (for milk samples) and

1×10^4 pg mL^{-1} (for buffer samples), calculated as the concentration for which the measured signal reaches three times the standard deviation above the background signal.

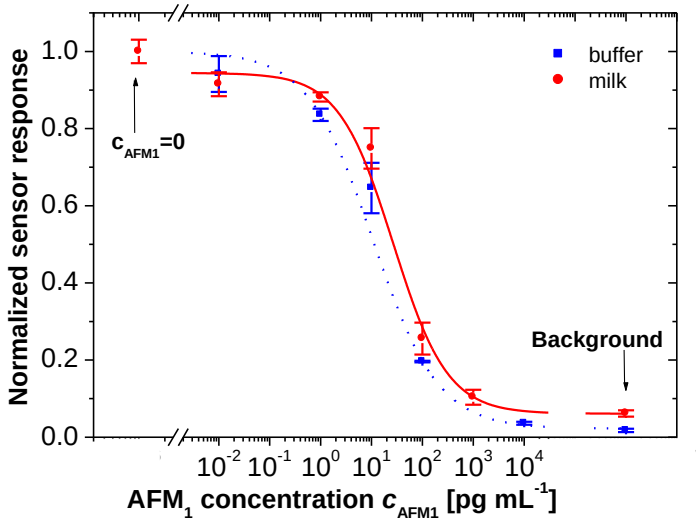

Figure 4.4 Normalized calibration curves for the detection of AFM_1 in buffer (squares) and milk (circles) samples.

The presented biosensor provides several orders of magnitude higher sensitivity with respect to other reported methods for the detection of aflatoxins including SPR biosensors (LOD = 3 ng mL^{-1}) [13], an electrochemical immunoassay (LOD = 25 pg mL^{-1}) [23], HPLC (LOD = 5 pg mL^{-1}) [10] or ELISA (LOD~10 pg mL^{-1}) [24]. Compared to the chemiluminescent immunoassay for detection of aflatoxin M_1 reported by Magliulo et al. (LOD = 0.25 pg mL^{-1}) [10], the developed biosensor offers a similar limit of detection and shorter detection time of 53 min.

4.4 Conclusion

A biosensor for the highly sensitive detection of aflatoxin M_1 (AFM_1) in milk was developed. This biosensor combined long range surface plasmon-enhanced fluorescence spectroscopy with an inhibition immunoassay and it allowed for the detection of AFM_1 at sub pg mL^{-1} levels within 53 min including the centrifuging of the milk sample, incubation of the sample with the antibody against AFM_1 and the detection of the level of unreacted antibody. The sensor could be regenerated more than 30 times without a change in its performance. The demonstrated limit of detection was about two orders of magnitude lower than the maximum residue level required by the European Commission. Such highly sensitive devices can be, for instance, used for early detection of rising AFM_1

concentration in milk products prior to it reaches levels for which the whole production has to be discarded. Future research will be aimed at further optimization of the biosensor assay in order to shorten the detection time, the implementation of an array detection format for the simultaneous analysis of multiple harmful compounds and the development of a compact sensor instrument capable of the operation in field.

References

1. Badea, M., Micheli, L., Messia, M. C., Candigliota, T., Marconi, E., Mottram, T., Velasco-Garcia, M., Moscone, D. and Palleschi, G. (2004). Aflatoxin M1 determination in raw milk using a flow-injection immunoassay system, *Anal. Chim. Acta*, **520**, 141-148.
2. Govaris, A., Roussi, V., Koidis, P. A. and Botsoglou, N. A. (2001). Distribution and stability of aflatoxin M-1 during processing, ripening and storage of Telemes cheese, *Food Addit. Contam.*, **18**, 437-443.
3. Bognanno, M., La Fauci, L., Ritieni, A., Tafuri, A., De Lorenzo, A., Micari, P., Di Renzo, L., Ciappellano, S., Sarullo, V. and Galvano, F. (2006). Survey of the occurrence of Aflatoxin M1 in ovine milk by HPLC and its confirmation by MS, *Mol. Nutr. Food Res.*, **50**, 300-305.
4. Kamkar, A. (2006). A study on the occurrence of aflatoxin M-1 in Iranian Feta cheese, *Food Control*, **17**, 768-775.
5. Rastogi, S., Dwivedi, P. D., Khanna, S. K. and Das, M. (2004). Detection of Aflatoxin M1 contamination in milk and infant milk products from Indian markets by ELISA, *Food Control*, **15**, 287-290.
6. Ammida, N. H. S., Micheli, L. and Palleschi, G. (2004). Electrochemical immunosensor for determination of aflatoxin B-1 in barley, *Anal. Chim. Acta*, **520**, 159-164.
7. Piermarini, S., Micheli, L., Ammida, N. H. S., Palleschi, G. and Moscone, D. (2007). Electrochemical immunosensor array using a 96-well screen-printed microplate for aflatoxin B-1 detection, *Biosens. Bioelectron.*, **22**, 1434-1440.
8. Ho, J. A. A. and Wauchope, R. D. (2002). A strip liposome immunoassay for aflatoxin B-1, *Anal. Chem.*, **74**, 1493-1496.
9. Garden, S. R. and Strachan, N. J. C. (2001). Novel colorimetric immunoassay for the detection of aflatoxin B-1, *Anal. Chim. Acta*, **444**, 187-191.
10. Magliulo, M., Mirasoli, M., Simoni, P., Lelli, R., Portanti, O. and Roda, A. (2005). Development and validation of an ultrasensitive chemiluminescent enzyme immunoassay for aflatoxin M-1 in milk, *J. Agr. Food Chem.*, **53**, 3300-3305.
11. Sapsford, K. E., Taitt, C. R., Fertig, S., Moore, M. H., Lassman, M. E., Maragos, C. A. and Shriver-Lake, L. C. (2006). Indirect competitive immunoassay for detection of aflatoxin B-1 in corn and nut products using the array biosensor, *Biosens. Bioelectron.*, **21**, 2298-2305.
12. Dunne, L., Daly, S., Baxter, A., Haughey, S. and O'Kennedy, R. (2005). Surface plasmon resonance-based inummoassay for the detection of affatoxin B-1 using single-chain antibody fragments, *Spectrosc. Lett.*, **38**, 229-245.
13. Daly, S. J., Keating, G. J., Dillon, P. P., Manning, B. M., O'Kennedy, R., Lee, H. A. and Morgan, M. R. A. (2000). Development of surface plasmon resonance-based immunoassay for aflatoxin B-1, *J. Agr. Food Chem.*, **48**, 5097-5104.
14. Homola, J. (2008). Surface plasmon resonance sensors for detection of chemical and biological species, *Chem.Rev.*, **108**, 462-493.
15. Liebermann, T. and Knoll, W. (2000). Surface-plasmon field-enhanced fluorescence spectroscopy, *Colloid. Surface. A*, **171**, 115-130.

16. Nenninger, G. G., Tobiska, P., Homola, J. and Yee, S. S. (2001). Long-range surface plasmons for high-resolution surface plasmon resonance sensors, *Sens. Actuator. B*, **74**, 145-151.
17. Kasry, A. and Knoll, W. (2006). Long range surface plasmon fluorescence spectroscopy, *Appl. Phys. Lett.*, **89**, 101106.
18. Slavik, R., Homola, J. and Vaisocherova, H. (2006). Advanced biosensing using simultaneous excitation of short and long range surface plasmons, *Meas. Sci. Technol.*, **17**, 932-938.
19. Wark, A. W., Lee, H. J. and Corn, R. M. (2005). Long-range surface plasmon resonance imaging for bioaffinity sensors, *Anal. Chem.*, **77**, 3904-3907.
20. Dostalek, J., Kasry, A. and Knoll, W. (2007). Long range surface plasmons for observation of biomolecular binding events at metallic surfaces, *Plasmonics*, **2**, 97-106.
21. Sarid, D. (1981). Long-range surface-plasma waves on very thin metal-films, *Phys. Rev. Lett.*, **47**, 1927–1930.
22. Zheng, M., Davidson, F. and Huang, X. Y. (2003). Ethylene glycol monolayer protected nanoparticles for eliminating nonspecific binding with biological molecules, *J. Am. Chem. Soc.*, **125**, 7790-7791.
23. Micheli, L., Grecco, R., Badea, M., Moscone, D. and Palleschi, G. (2005). An electrochemical immunosensor for aflatoxin M1 determination in milk using screen-printed electrodes, *Biosens. Bioelectron.*, **21**, 588-596.
24. Velasco, M. L. R., Delso, M. M. C. and Escudero, D. O. (2003). ELISA and HPLC determination of the occurrence of aflatoxin M-1 in raw cow's milk, *Food Addit. Contam.*, **20**, 276-280.

Chapter 5 Dextran Hydrogel Binding Matrix for Biosensors Based on Long Range Surface Plasmon-Enhanced Fluorescence Spectroscopy

Abstract

A new biosensor based on surface plasmon-enhanced fluorescence spectroscopy (SPFS), which employs long range surface plasmons (LRSP) and a photocrosslinkable carboxymethyl dextran (PCDM) hydrogel binding matrix, is reported. LRSPs are surface plasmon modes that propagate along a thin metallic film with orders of magnitude lower damping compared to regular surface plasmons. Therefore, their excitation provides strong enhancement of the intensity of the electromagnetic field and a greatly increased fluorescence signal measured upon binding of fluorophore-labeled molecules on the sensor surface. In addition, these modes exhibit highly extended evanescent fields penetrating up to micrometers in distance from the metallic sensor surface. Therefore, a PCDM hydrogel with approximately micrometer thickness was anchored on the sensor surface to serve as the binding matrix. We show that this approach provides large binding capacity and allows for the ultra-sensitive detection. In a model experiment, the developed biosensor platform was applied for the detection of free prostate specific antigen (f-PSA) in buffer and human serum by using a sandwich immunoassay. The limit of detection at low femto-molar range was achieved, which is approximately four orders of magnitude lower than that for direct detection of f-PSA based on the monitoring of binding-induced refractive index changes.

5.1 Introduction

Surface plasmon resonance (SPR) biosensors become an important technology that is pushed forward for rapid and sensitive detection of chemical and biological species.[1] In this method, the analyzed liquid sample is flowed over a metallic sensor surface with attached biomolecular recognition elements. The capture of target molecules on a sensor surface is probed by resonantly excited surface plasmons (SPs) and the binding-induced changes in the refractive index are detected. SPR biosensors offer the advantage of direct detection of biomolecular binding events. For medium size proteins such as prostate specific antigen (PSA), SPR biosensors were shown to allow the direct detection at concentrations in the nano-molar range for which the molecular binding induces sufficiently large refractive index changes.[2, 3] However, such sensitivity is often not sufficient in many applications and thus approaches for enhancing the refractive index changes were investigated. These include the assays with metallic nanoparticle[4-7] and enzyme[8] labels which were demonstrated to improve the limit of detection (LOD) by several orders of magnitude. In addition, an approach for advancing the sensitivity through the combining of SPR biosensors with fluorescence spectroscopy was developed.[9, 10] In this method referred as to surface plasmon-enhanced fluorescence spectroscopy (SPFS), the capture of molecules labeled with fluorophores is observed through the detection of the intensity of the fluorescence light emitted from the sensor surface. This technique takes advantage of the strong intensity of the electromagnetic field accompanied with the resonant excitation of surface plasmons. The interaction of fluorophores with the evanescent field of surface plasmons allows for enhancing the excitation rate[11] of molecules adhered to the metallic surface as well as for the efficient collecting the fluorescence light.[12] SPFS biosensors that relies on immunoassays were shown to enable the detection of protein molecules below femto-molar concentrations.[13]

Recently, long-range surface plasmons (LRSPs) were exploited for SPFS biosensing.[14-16] These optical waves originate from the coupling of surface plasmons on opposite surfaces of a thin metallic film that is embedded between dielectrics with similar refractive indices. LRSPs exhibit orders of magnitude lower damping compared to regular surface plasmons on an individual metallic surface.[17] Therefore, their excitation provides larger enhancement of the electromagnetic field intensity and thus allows for stronger increasing the fluorescence signal in SPFS sensors. In addition, LRSPs probe the medium

adjacent to the metallic surface with more extended evanescent field than regular surface plasmons.[15] Therefore, three-dimensional binding matrices with up to micrometer thickness have been proposed for the immobilization of biomolecular recognition elements with large surface density that allows to exploit the whole evanescent field of LRSP.[18] Currently, new hydrogels materials based on NIPAAM [N-(isopropylacrylamide)] and dextran polymers were developed in our laboratory and they were demonstrated to be suitable for the construction of such surface architectures.[19-21]

We report a new ultra sensitive biosensor exploiting LRSP-enhanced fluorescence spectroscopy with photocrosslinkable carboxymethyl dextran (PCMD) hydrogel binding matrix for the detection of prostate specific antigen (PSA) in human serum. PSA is a 33-34kDa single-chain glycoprotein which has been used for the diagnosis of prostate cancer.[22] The analyte is present in blood serum in the form of free PSA (f-PSA) and PSA bound to antichymotrypsin (PSA-ACT). Currently, clinically relevant levels of this analyte in blood serum are below 0.3 nM (corresponding to 10 ng mL^{-1}) and they are routinely analyzed in specialized laboratories by *e.g.* enzyme-linked immunosorbent assays (ELISA).[23] Biosensors for rapid detection of PSA at orders of magnitude lower concentrations are expected to provide a valuable tool for point-of-care diagnosis (POC) of female breast cancer,[24] early identification of prostate cancer relapse[25] and in forensic applications.[26] Research in novel methods for ultra-sensitive and simplified analysis of PSA was carried out including immuno-PCR (LOD of 6 fM and analysis time >150 min),[27] bio barcode-based detection (LOD of 30 aM and analysis time of 80 min),[28] gold nanoparticle sandwich immunoassay combined with surface-enhanced Raman scattering (SERS) (LOD of 30 fM and analysis time of ~ 550 min)[29] and SPR (LOD of 30 pM)[3] and SPFS with sandwich immunoassay (LOD of 80 fM and analysis time of 40 min).[30]

5.2 Materials and methods

5.2.1 Chemicals and biochemicals

All reagents were used as received without further purification. f-PSA (>95% pure from human seminal fluid, A32874H), a monoclonal mouse IgG_1 antibody recognizing the PSA epitope 4 used as a capture antibody (c-Ab, M86599M) and a monoclonal mouse IgG_{2a} antibody specific for the PSA epitope 6 used as a detection antibody (d-Ab, M86506M) were obtained from Biodesign (Biosite, Sweden). HBS-EP buffer (degassed

10 mM HEPES buffer saline, pH 7.4, 150 mM NaCl, 3 mM EDTA, 0.005% (v/v) surfactant P-20), acetate buffer (10 mM, pH 5.0), glycine buffer (10 mM, pH 1.7) were obtained from Biacore (Sweden). The d-Ab was labeled by using Alexa Fluor 647 labeling kit from Molecular Probes Inc. (USA). The dye-to-protein molar ratio was determined by an UV-visible spectrometer as 5. Single donor female serum was obtained from Innovative Research (USA). The novel photocrosslinkable carboxymethyl dextran (PCMD) was synthesized as described in detail by Brunsen et al.[31] Briefly, 10 g of dextran (MR~2000000 from Sigma Aldrich, USA) was dissolved in 150 mL distilled water followed by the addition of 20 g (0.21 mol) sodium chloroacetate (Acros Organics). In order to initiate the reaction, 50 mL of 8 M sodium hydroxide solution was added and the reaction was carried out for 1 hour at the temperature of 62 ℃. After cooling down for 10 minutes, the reaction was terminated by neutralizing with 6 M hydrochloric acid. The carboxymethylated dextran (CMD) was precipitated in ice cold ethanol and purified by dialyzing against distilled water. After evaporation of the solvent, CMD is obtained as white powder. For the benzophenone coupling, 1 g CMD was dissolved in dried DMSO and kept under argon atmosphere. The reaction was carried for 3 hours out at room temperature after the addition of 0.35g (0.00166mol) TFA-NHS and ~5 mL of 4-methylmorpholine (Merck). The obtained mixture was dialyzed against DMSO over night and was directly followed by the reaction with 0.4 g (0.0019 mol) / 0.22 g (0.00095 mol) 4-aminomethylbenzophenone in DMSO with 5 mL / 10 mL of 4-methylmorpholine at room temperature and under argon atmosphere. The obtained compound was purified by extensive dialyzing against DMSO and distilled water. As seen in Figure 5.1, the PCMD carried carboxylic groups for the anchoring of protein molecules via their amino groups and benzophenone groups for the crosslinking and attaching of the gel to a metallic surface that was modified with benzophenone moieties by UV light. In the following experiments, we used two PCMDs with the ratio of benzophenone and carboxylic groups to C-H groups of 1 : 6.5 : 34 and 1 : 4.4 : 23, respectively. The benzophenone-terminated thiol was synthesized at the Max Planck Institute for Polymer Research in Mainz as described previously.[20]

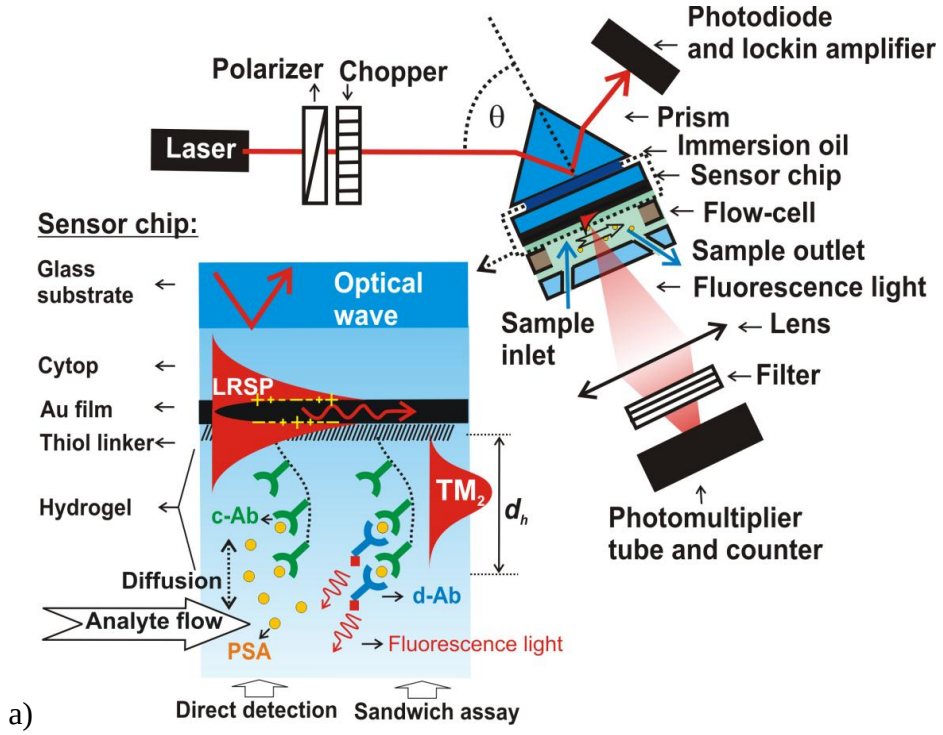

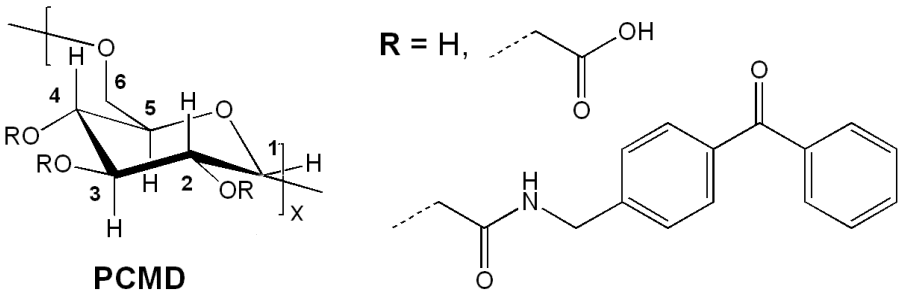

Figure 5.1 a) Scheme of the optical setup for the excitation of LRSPs on the sensor surface with PCMD hydrogel binding matrix and the f-PSA detection immunoassays. b) PCMD chemical structure.

5.2.2 Sensor instrument

As shown in Figure 5.1, an attenuated total reflection (ATR) method was used for the excitation of LRSPs on the sensor surface (see section 3.1.1). The monitoring of reflectivity changes ΔR at an angle of incidence θ set to the maximum slope of the dip associated with the resonant excitation of LRSPs allowed the measurement of refractive index changes with the resolution around 10^{-6} refractive index units (RIU). The thickness d_h and the refractive index n_h of the hydrogel binding matrix was determined by fitting

the resonant angles for the excitation of LRSP and hydrogel waveguide modes similar as described before.[19] In the further analysis, we assumed that the refractive index of the hydrogel n_h changes with the concentration of proteins and the hydrogel polymer as $\partial n/\partial c \approx 0.2$ μL mg^{-1}. From the refractive index contrast $n_h - n_b$ and the thickness d_h the surface mass density Γ of the hydrogel film was calculated as equation (2.51).

5.2.3 Functionalization of the sensor surface

The gold-coated substrates were immersed in ethanol containing 5 mM benzophenone-terminated thiol to allow the formation of a self assembled monolayer (SAM). After the overnight incubation, the gold surface was rinsed with ethanol and dried with a nitrogen stream. On the surface modified by the thiol-SAM, a PCMD layer was deposited by spin-coating with the thickness in the range of 210 - 280 nm (measured in contact with air) from an aqueous solution with the concentration of PCMD between 60 and 80 mg mL^{-1}. Afterwards, the PCMD film was dried at a temperature of T = 45 ℃ for 4 hours and exposed to UV-light (wavelength of λ = 254 nm, irradiation energy dose of 2 J cm^{-2}) for 90 min in order to establish its photo-chemical attachment to the surface and cross-linking. Then, the substrates were mounted to the sensor, the PCMD hydrogel was swollen in ACT buffer at pH = 5 and *in situ* c-Ab were immobilized according to the following recipe. Firstly, a mixture of 1-(3-dimethylaminopropyl)-3-ethylcarbodiimide hydrochloride (EDC, 37.5 mg mL^{-1}) and *N*-hydroxysuccinimide (NHS, 10.5 mg mL^{-1}) was flowed for 8 min in order to form terminal NHS ester moieties. Afterwards, the c-Ab dissolved in sodium acetate buffer (10 mM, pH 5.0) at a concentration of 50 μg mL^{-1} was injected for 30 min followed by rinsing with ACT buffer for 10 minutes. The unreacted NHS ester moieties were deactivated by the incubation in a 1 M ethanolamine hydrochloride solution for 7 minutes.

5.2.4 Detection assay

Series of samples were prepared by spiking HBS-EP buffer and human serum (volume of 800 μL) with f-PSA. Samples with f-PSA dissolved in HBS-EP at concentrations between 3 and 300 nM were used for the evaluation of the direct detection of f-PSA. For the SPFS-based detection, f-PSA was dissolved in human serum (with free PCMD at a concentration of 0.5 mg mL^{-1}) and HBS-EP buffer at concentrations ranging

from 100 fM to 10 pM. In the direct detection experiment, HBS-EP buffer was flowed for 10 minutes in order to establish a baseline followed by an the incubation of the sensor surface with of a sample for 30 min and rinsing by HBS-EP buffer for 10 minutes. Upon the binding of f-PSA to the PCMD hydrogel with c-Ab, the changes in reflectivity R were measured in time at a fixed angle θ set to the value providing the highest slope of the reflectivity LRSP dip. The direct sensor response was determined as the difference of the reflectivity signal ΔR before and after the f-PSA binding. In the SPFS-based detection, a sandwich immunoassay was employed. Firstly, a sample spiked with f-PSA was flowed through the sensor cell for 15 minutes. Afterwards, the hydrogel matrix was rinsed for 1 minute with HBS-EP buffer and d-Ab dissolved at a concentration of 1 nM was flowed through the sensor cell for 10 minutes followed by rinsing with HBS-EP buffer for 5 min. The fluorescence signal F was measured as a function of time at the resonant angle of incidence θ providing strong enhancement of the electromagnetic field due to the coupling to LRSPs. The fluorescence sensor response ΔF was evaluated as the difference between the fluorescence signal F before the injection of d-Ab and after the 4.5 min washout with HBS-EP (data points measured during 1 minute were averaged). The detection was performed in cycles. After each detection cycle, the sensor surface was regenerated by a 5-10 min pulse of glycine (pH = 1.5) and a 5-15 min pulse of 10 mM NaOH in order to release the captured f-PSA leaving free c-Ab binding sites.

5.3 Results and Discussion

5.3.1 Swelling properties

Firstly, the swelling properties of the PCMD hydrogel were evaluated. Figure 5.2 shows the reflectivity spectra measured for the bare gold surface, for the swollen hydrogel film attached to the gold surface and for the swollen hydrogel modified by the capture antibody c-Ab. These data reveal that after the attachment of the hydrogel film and its swelling in HBS-EP buffer, the resonance dip associated with the excitation of LRSP shifts to higher angles with respect to that on bare gold surface. In addition, the reflectivity curve is changed in the vicinity of the critical angle θ = 47.5 deg due to the appearance of an optical waveguide mode TM_2 supported by the thin hydrogel layer. In Figure 5.2a, reflectivity curves measured for the hydrogel film with the ratio of benzophenone to C-H group of 1:34 and thickness of d_h = 210 nm (in contact with air) are

shown. By fitting the spectrum measured after the swelling of the gel in HBS-EP buffer, its thickness and refractive index was determined as d_h = 0.98 μm and n_h = 1.346. Based on the effective medium theory,[32] we determined the polymer volume fraction as f = 7% by using the equation as (2.52), where $n_{h\text{-}dry}$ = 1.51[33] is the refractive index of dry dextran polymer. Figure 5.2b shows the reflectivity curves for the hydrogel with the higher ratio of benzophenone to C-H groups of 1:23 that was deposited with a higher thickness d_h = 280 nm (in contact with air). The fitting of the respective angular reflectivity spectra measured after the swelling in HBS-EP revealed that it exhibited larger thickness of d_h = 1.3 μm and a higher refractive index n_h = 1.352 corresponding to higher polymer volume fraction around 10%. Let us note that the optical thickness of this gel was high enough to support a TM_2 mode as can be seen from the additional resonance dip located at the angle of incidence θ = 47.6. Surface mass densities of Γ = 59 and 117 ng mm^{-2} were determined for two hydrogel films with thickness in the swollen state of d_h = 0.98 and 1.3 μm, respectively (measured in HBS-EP buffer). These data indicate that the higher concentration of benzophenone groups resulted in a higher gel density in swollen state. The immobilization of a capture antibody c-Ab into the hydrogel layer caused an increase in the refractive index of the gel as seen from the shifts of the resonant dips due to the excitation of LRSPs and TM_2 hydrogel waveguide modes. The fitting of the corresponding reflectivity spectra indicate that the refractive index increased to n_h = 1.355 and 1.372 for the hydrogels with a thickness of d_h = 0.98 and 1.3 μm, respectively, and that the thickness of the hydrogel films swollen in HBS-EP buffer did not change significantly. The surface mass density of the thicker hydrogel film (d_h = 1.3 μm) and of the thinner film (d_h = 0.98 μm) increased to Γ = 247 ng mm^{-2} and Γ = 103 ng mm^{-2}, respectively. The amount of anchored c-Ab molecules was estimated as the difference between the surface mass density before and after the c-Ab coupling as Γ = 130 and 44 ng mm^{-2} for the thicker and thinner film, respectively, that is up to order of magnitude higher than that reported for regularly used dextran brush exhibiting the thickness of about 100 nm (CM5 chip from Biacore, Sweden).[34] The prepared dextran hydrogel surfaces allowed for the immobilization of a large amount of c-Ab of which the surface mass density was close to that of the PCMD gel itself. In further experiments, we used the hydrogel with lower volume fraction around 7%.

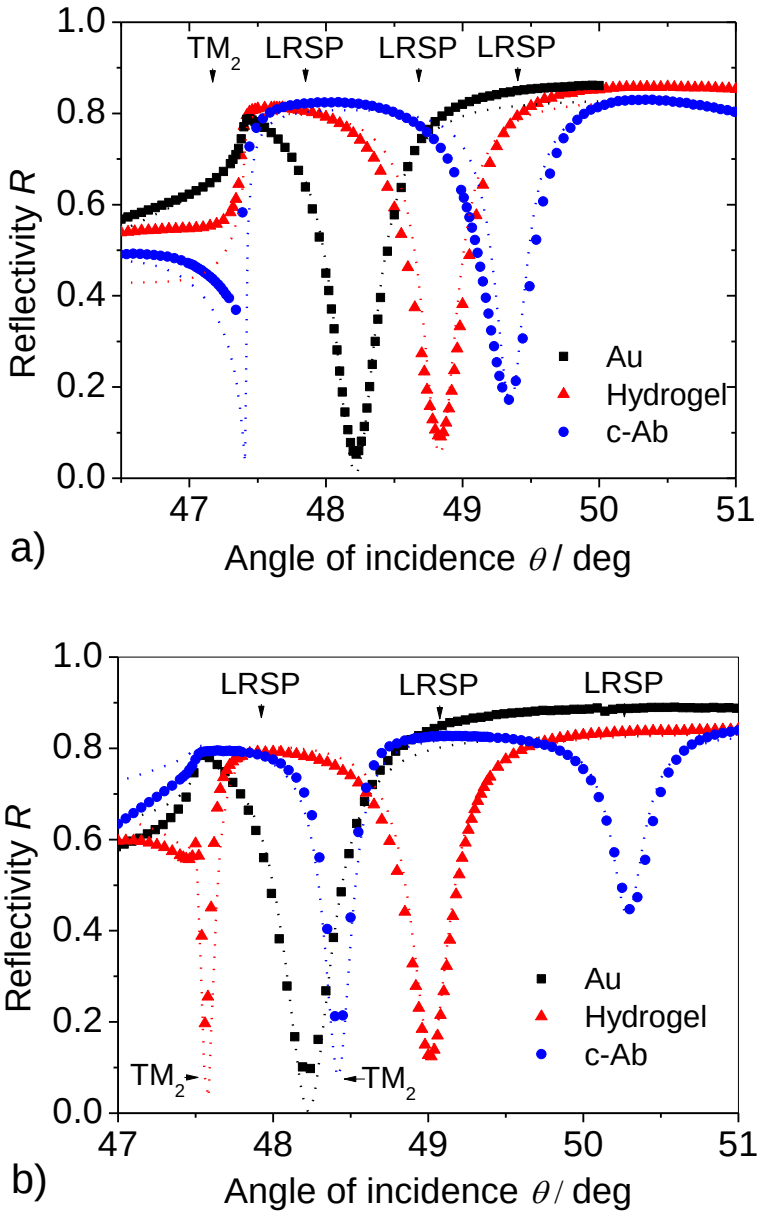

Figure 5.2 Angular reflectivity spectra for a hydrogel film a) with the ratio of benzophenone to C-H groups of 1:34 and the thickness of 210 nm (measured in the contact with air) and b) with the ratio of benzophenone to C-H groups of 1:23 and the thickness of 280 nm (measured in the contact with air). The squares show the spectra for bare gold surface, triangles show the spectra measured after the attaching and swelling of the gel and circles show the spectra measured after the immobilization of c-Ab (HBS-EP buffer was flowed along the sensor surface). The dotted lines show the corresponding fits of measured reflectivity curves.

5.3.2 Kinetic analysis of the affinity binding in the hydrogel matrix

The affinity binding of f-PSA to the c-Ab receptors immobilized in a PCMD hydrogel was observed by LRSP spectroscopy and by LRSP-enhanced fluorescence spectroscopy. In the following experiment, we used a hydrogel with the thickness and surface mass density of d_h = 0.95 and Γ = 66.5 ng mm^{-2}, respectively, measured prior to the modification by c-Ab. The gel was modified by c-Ab with the surface mass density of Γ = 48 ng mm^{-2}. Firstly, HBS-EP buffer was flowed over the sensor surface in order to establish a baseline of the reflectivity signal ΔR. Afterwards, a solution with f-PSA dissolved at a concentration of 300 nM was injected for 30 minutes and a gradual increase in the reflectivity was observed due to the refractive index changes induced by f-PSA binding, see Figure 5.3a. After this association phase, HBS-EP buffer was flowed through the sensor cell and an exponential decrease in the reflectivity R was observed due to the dissociation of the f-PSA from c-Ab. By fitting the measured kinetics with a Langmuir adsorption model,[35] the association and dissociation constants were determined as k_a = 4.8×10^3 M^{-1} s^{-1} and k_d = 2.4×10^{-4} s^{-1}, respectively. These values are comparable to those reported by Yu et al. (k_a = 2.2×10^4 M^{-1} s^{-1} and k_d = 3.2×10^{-4} s^{-1})[30] who analyzed the identical antigen-antibody pair by a SPR biosensor with c-Ab immobilized with a surface mass density of Γ = 1.8 ng mm^{-2} on the CM5 chip coated by a dextran brush (from Biacore, Sweden). The approximately 4-fold lower association constant k_a indicates that the diffusion of f-PSA through the PCMD hydrogel highly loaded with c-Ab did not hinder the binding kinetics dramatically. Moreover, we observed the affinity binding of the detection antibody d-Ab labeled with Alexa-Fluor 647 chromophore to the captured f-PSA molecules by LRSP-enhanced fluorescence spectroscopy. Figure 5.3b shows the time kinetics of the fluorescence signal upon a 15-minute flow of a solution with f-PSA dissolved at a concentration of 10 pM followed by a 2-minute rinsing by HBS-EP buffer, 10-minute flow of d-Ab at a concentration of 1 nM and final rinsing by the HBS-EP buffer for 30 minutes. After the time t = 0 when the d-Ab solution was injected, an increase in the fluorescence signal is observed due to the diffusion of d-Ab molecules into the gel and the affinity binding to the captured f-PSA molecules. During the flow of the HBS-EP buffer for time t > 10 min, a fast drop of the fluorescence signal F is observed owing to the washout of unbound d-Ab molecules. Afterwards, the fluorescence signal exponentially decreased due to the dissociation of the complex c-Ab/f-PSA/d-Ab. By

fitting the exponential decay of the signal with the Langmuir model, we determined the dissociation constant as $k_d = 5.5 \times 10^{-4}$ s^{-1}. This value is comparable to that measured for the dissociation of the f-PSA bound to c-Ab which indicates good stability of c-Ab, f-PSA and the d-Ab complex.

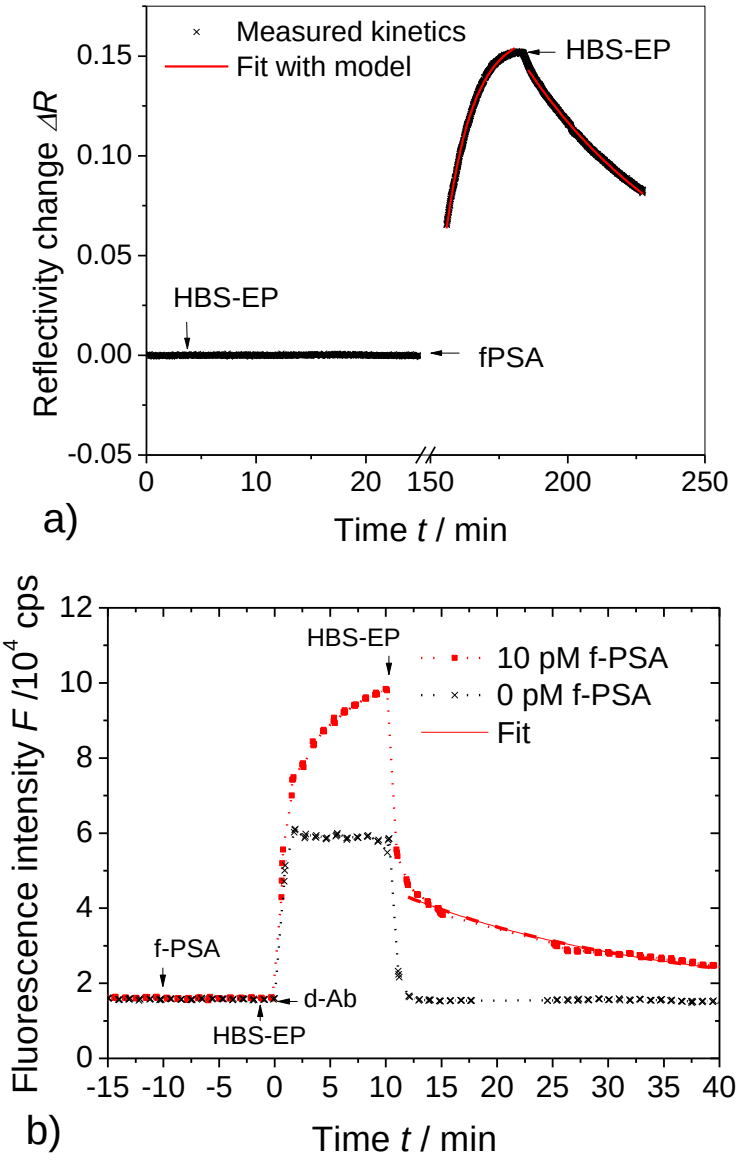

Figure 5.3 a) Time evolution of the reflectivity changes ΔR upon the dissociation and association of f-PSA to c-Ab. The concentration of f-PSA in HBS-EP was 300 nM and the c-Ab was immobilized with surface mass density of $\Gamma = 48$ ng mm^{-2} in the gel with the thickness of $d_h = 950$ nm (measured in HBS-EP). b) Fluorescence signal measured upon the successive flow of a solution with f-PSA (concentration of 10 pM in HBS-EP) and Alexa Fluor 647 chromophore-labeled d-Ab (dissolved of concentration 1 nM in HBS-EP).

5.3.3 Direct detection of f-PSA

By using a spectroscopy of LRSPs and a hydrogel matrix with thickness d_h = 950 nm and surface mass density of Γ = 66.5 ng mm^{-2}, direct detection of f-PSA in HBS-EP buffer was performed. As shown in Figure 5.4a, the sequential injection of samples with f-PSA at concentrations between 3 nM and 300 nM induced a gradual increase in the reflectivity ΔR. After the injection of the sample with the maximum f-PSA concentration of 300 nM, the increase in the reflectivity shift ΔR started to saturate and reached approximately the value ΔR = 0.16. The specificity of the f-PSA binding was verified in an experiment in which 30 nM f-PSA was flowed over the PCMD without c-Ab which showed no significant change in the reflectivity (Figure 5.4a). In addition to the specific binding of f-PSA, we investigated the interaction of PCMD hydrogel with human serum that was not spiked with f-PSA. As seen in Figure 5.4b, upon the injection of a serum sample a large increase in the reflectivity change ΔR occurs which indicates that the blood serum efficiently diffuses inside the gel. After the rinsing with HBS-EP for 5 minutes, the reflectivity stabilized at ΔR = 0.07 above the original value prior the incubation with serum. This change is due to the non-specifically bound serum components adhering within the hydrogel matrix possibly due to electrostatic and physical adsorption. The spectra in Figure 5.4c revealed that the mass density of non-specifically adsorbion reached a value of 5 ng mm^{-2}. The non-specifically bound serum can be fully washed out by applying the regeneration. In addition, the spiking of serum with free PCMD at a concentration of 0.5 mg mL^{-1} responded in an approximately 2.7 fold decrease of sensor response due to the adhered serum components. This behavior is similar to that in the dextran brush (CM5 chip from Biacore Inc., Sweden) reported by Yu et al.[30] and can be explained by the competitive binding of the substances contained in serum to free PCMD molecules which reduces their adsorption within the gel. The calibration curve for the direct detection of f-PSA in HBS-EP buffer is presented in Figure 5.5. From these data, we determined a LOD of 0.68 nM as the concentration for which linear fit of the calibration curve reaches three times the standard deviation of the baseline $3\sigma(\Delta R) = 8\times10^{-4}$.

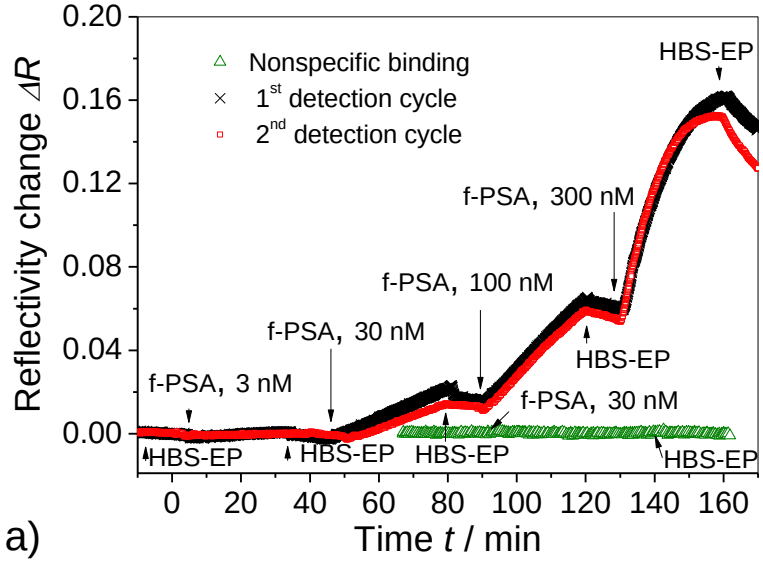
Reflectivity change ΔR
Time t / min
Nonspecific binding
1st detection cycle
2nd detection cycle
f-PSA, 3 nM
f-PSA, 30 nM
f-PSA, 100 nM
f-PSA, 300 nM
f-PSA, 30 nM
HBS-EP
HBS-EP
HBS-EP
HBS-EP
HBS-EP
HBS-EP
a)

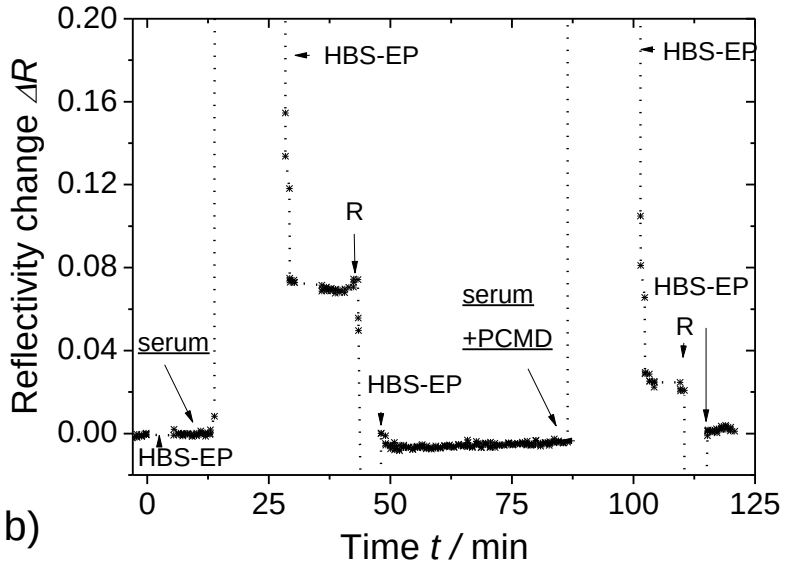
Reflectivity change ΔR
Time t / min
serum
HBS-EP
HBS-EP
R
HBS-EP
serum
+PCMD
HBS-EP
HBS-EP
R
b)

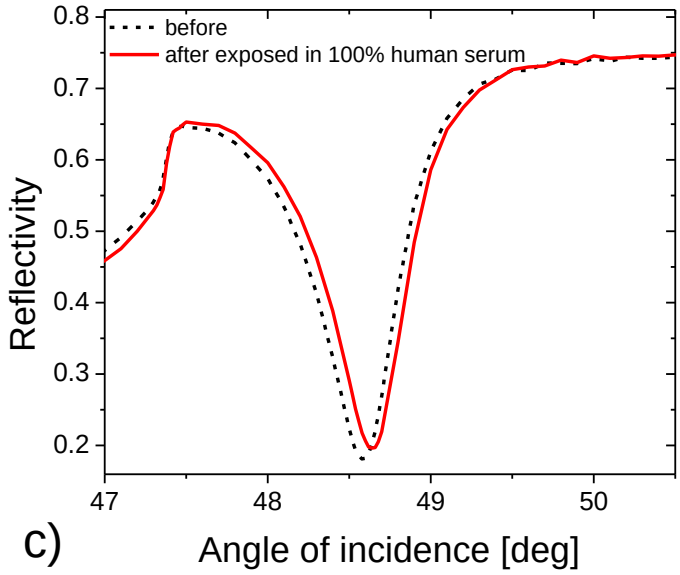

Figure 5.4 a) Changes in the reflectivity ΔR measured upon the specific (crosses and squares) and non-specific (triangles) binding of f-PSA dissolved at concentrations between 3 and 300 nM in PCMD binding matrix. b) Time evolution of changes in the reflectivity changes ΔR for two detection cycles with the 15-minute incubation in human serum with and without spiking with PCMD at the concentration of 0.5 mg mL^{-1} followed by the regeneration (R) and rinsing with HBS-EP buffer. c) Angular reflectivity measurement for the PCMD thin film before (dash) and after (solid) exposed in 100% human serum.

5.3.4 Detection of f-PSA by SPFS

For the SPFS detection of f-PSA in HBS-EP buffer and human serum, a hydrogel with a thickness of d_h = 1.32 μm and a surface mass density of Γ = 56 ng mm^{-2} was used. Into the gel, the capture antibody c-Ab was immobilized with a surface mass density of Γ = 41 ng mm^{-2}. In these experiments, buffer and human serum samples spiked with f-PSA were analyzed. As described before, the analysis was performed in cycles comprising the flow of the analyzed sample for 15 minutes followed by the 10-minute incubation of the d-Ab, 5-minute washout with HBS-EP buffer and regeneration. Figure 5.6a shows the time evolution of the fluorescence signal F measured during the five detection cycles for the HBS-EP samples spiked with f-PSA at concentrations of 0 - 10 pM. These data reveal that fluorescence sensor response ΔF increases with the concentration of f-PSA. For the concentration of f-PSA equal to zero, a rapid step-like increase and decrease in the

fluorescence signal F was observed at time t = 0 and 10 min, respectively, due to the diffusion of d-Ab in and out of the gel. No measureable change in the fluorescence signal ΔF was observed for the blank HBS-EP buffer sample, and the sample with the f-PSA at a concentration of 10 pM induced a sensor response of $\Delta F = 2.3 \times 10^4$ cps. After the flow of the detection antibody d-Ab, the angular fluorescence intensity spectra were measured for the concentrations of f-PSA 0, 0.4 and 10 pM, see Figure 5.6b. Strong fluorescence peaks were observed at the angle of incidence for which LRSPs were resonantly excited and their maximum intensity increases with the concentration of f-PSA. Moreover, an enhanced fluorescence signal was measured at angles close to the critical angle θ = 47.4 deg. This increase is due to the coupling of the incident light to the hydrogel waveguide mode TM_2 that provides an additional enhancement of the electromagnetic field intensity similar to LRSPs.

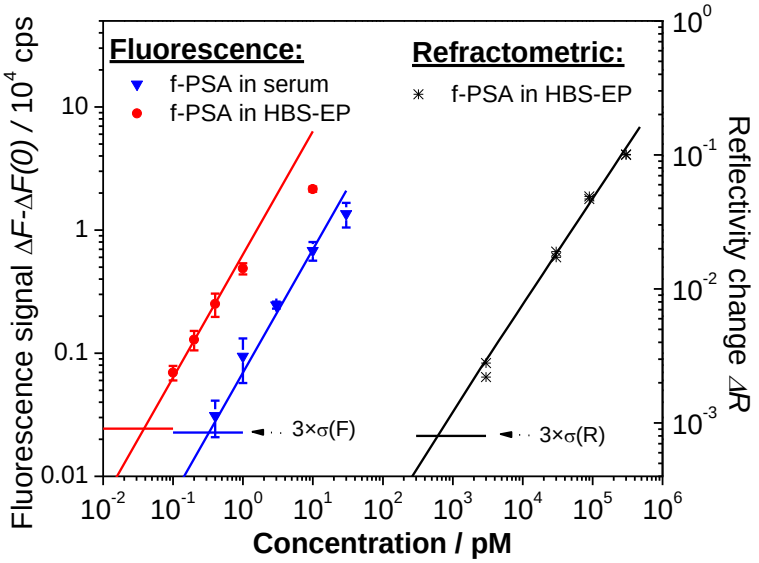

Figure 5.5 Calibration curves for the direct detection of f-PSA (refractometric - stars) compared to the sandwich immunoassay-based detection with fluorescence readout for f-PSA dissolved in HBS-EP (circles) and in human serum (triangles). Lines show the linear fit and the error bars show the standard deviation.

Similarly, we measured the sensor response ΔF for a series of human serum samples spiked with f-PSA. For the analysis of blank human serum sample not spiked with f-PSA, a significant increase in the senor response of $\Delta F(0) \sim 625$ cps was observed which was probably due to the non-specific adsorption of d-Ab to the blood plasma components

adhering to the sensor surface. The comparison of the calibration curve for the direct detection f-PSA in HBS-EP buffer (SPR) and for the fluorescence readout of sandwich immunoassay detection of f-PSA in HBS-EP and human serum (SPFS) is presented in Figure 5.5. The LOD for the SPFS readout was defined as the concentration for which the linear fit of the calibration curve reaches that for a blank sample $\Delta F(0)$ plus three times the standard deviation of the fluorescence signal $3\sigma(F)$ = ~230 cps. For the detection in HBS-EP buffer and human serum, the LOD of 34 and 330 fM was determined, respectively. The LOD of f-PSA in human serum is about one order of magnitude higher than that of PSA in buffer probably due to slower diffusion of f-PSA into the gel in the serum which exhibit higher viscosity and owing to the blocking the c-Ab antibody immobilized in the hydrogel matrix by means of non-specific sorption. The sensor surface showed good reproducibility with the relative standard deviation of the sensor response ΔF of 4% after 30 detection cycles and four days of operation. SPFS-based analysis of an individual sample was performed in 30 min including the 15-minute incubation of the sensor surface with a sample, 10-minute flow of the d-Ab and 5-minute washout of the sensor surface. Comparison with the regular SPFS and dextran brush surface architecture reported by Yu et al.[30], moderate improvement of LOD (approximately two-fold) and sample incubation time (two-fold) was achieved. In human serum, the LOD was significantly deteriorated. This effect was probably due to the non-specific interaction of the serum with the PCMD hydrogel matrix that was not observed for the dextran brush on the top of the CM5 chip (from Biacore, Sweden).

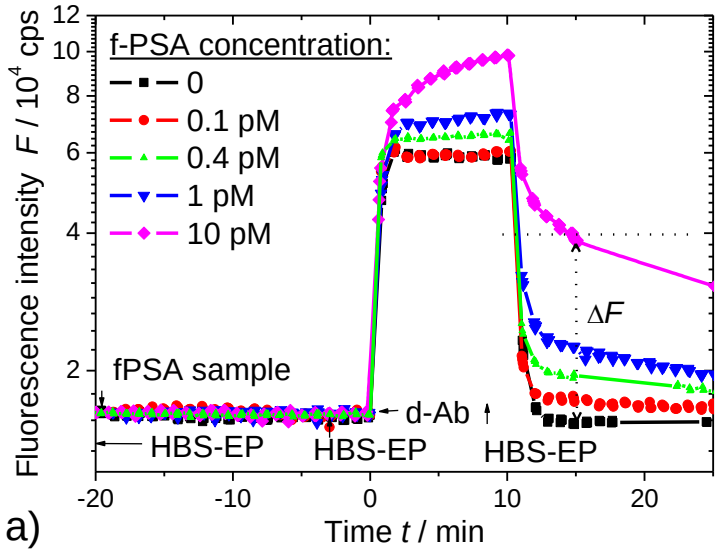

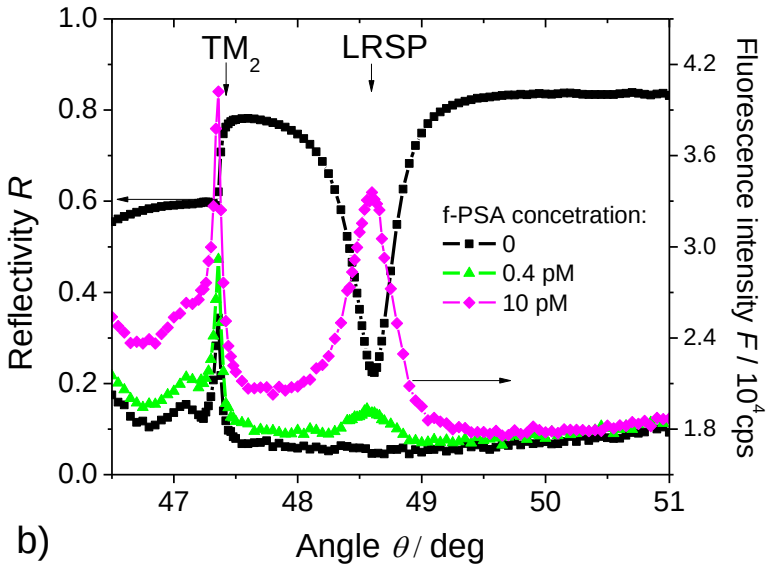

Figure 5.6 a) Time evolution of the fluorescence signal F upon the analysis of HBS-EP samples spiked with f-PSA at concentrations 0 - 10 pM. b) Angular fluorescence spectra measured after the flow of HBS-EP samples spiked with f-PSA at concentrations of 0, 0.4 and 10 pM.

We expect that the LOD can be further improved by the optimization of the hydrogel density and thickness in order to provide faster diffusion of target analyte and its binding closer to the surface where the LRSP field enhancement is stronger. In addition, compacting the captured analyte on the sensor surface through externally triggered collapse observed for "smart" gels can be used for more sensitive detection molecular binding.[36] For the thickness of the hydrogel matrix d_h larger than 1 μm, the excitation of an additional hydrogel waveguide mode was observed to provide enhancement of the fluorescence signal which may provide new, potentially more sensitive, means for the detection of biomolecular binding events.

5.4 Conclusions

A new biosensor platform exploiting the excitation of long range surface plasmons and a PCMD hydrogel binding matrix was developed and applied for the detection of f-PSA in human serum. The investigation of swelling properties of the PCMD hydrogel film with approximately micrometer thickness in the swollen state revealed that it exhibits a highly open structure in which protein catcher molecules can be immobilized with orders of magnitude larger surface mass density compared to *e.g.* the monolayer surface

architectures relying on thiol-SAM. The measurement of the kinetics of the binding of f-PSA to the immobilized catcher antibody showed that the target analyte can diffuse fast through the gel and the determined affinity binding constants were comparable to those obtained for other surface architectures. The direct detection of f-PSA by using the spectroscopy of LRSPs and sandwich immunoassay-based detection combined with SPFS were carried out. The LOD for the fluorescence-based detection of 34 fM was achieved in buffer, which was more than 4 orders of magnitude lower than that for the direct detection. In addition, the fluorescence readout combined with the sandwich immunoassay was less affected by the non-specific interaction of human serum with the PCMD hydrogel matrix and allowed for the analysis of f-PSA at concentrations down to 330 fM. We expect that further optimization of the hydrogel matrix and modifying the optical scheme for the readout of arrays of sensing spots will provide a generic biosensor platform for rapid and ultra-sensitive analysis with potential applications in a range of important areas including medical diagnostics.

References

1. Homola, J. (2008). Surface plasmon resonance sensors for detection of chemical and biological species, *Chem.Rev.*, **108**, 462-493.
2. Cao, C., Kim, J. P., Kim, B. W., Chae, H., Yoon, H. C., Yang, S. S. and Sim, S. J. (2006). A strategy for sensitivity and specificity enhancements in prostate specific antigen-alpha(1)-antichymotrypsin detection based on surface plasmon resonance, *Biosens. Bioelectron.*, **21**, 2106-2113.
3. Huang, L., Reekmans, G., Saerens, D., Friedt, J. M., Frederix, F., Francis, L., Muyldermans, S., Campitelli, A. and Van Hoof, C. (2005). Prostate-specific antigen immunosensing based on mixed self-assembled monolayers, camel antibodies and colloidal gold enhanced sandwich assays, *Biosens. Bioelectron.*, **21**, 483-490.
4. Wark, A. W., Lee, H. J., Qavi, A. J. and Corn, R. M. (2007). Nanoparticle-enhanced diffraction gratings for ultrasensitive surface plasmon biosensing, *Anal. Chem.*, **79**, 6697-6701.
5. Lee, H. J., Wark, A. W. and Corn, R. M. (2008). Enhanced bioaffinity sensing using surface plasmons, surface enzyme reactions, nanoparticles and diffraction gratings, *Analyst*, **133**, 596-601.
6. Mitchell, J. S., Wu, Y. Q., Cook, C. J. and Main, L. (2005). Sensitivity enhancement of surface plasmon resonance biosensing of small molecules, *Anal. Biochem.*, **343**, 125-135.
7. He, L., Musick, M. D., Nicewarner, S. R., Salinas, F. G., Benkovic, S. J., Natan, M. J. and Keating, C. D. (2000). Colloidal Au-enhanced surface plasmon resonance for ultrasensitive detection of DNA hybridization, *J. Am. Chem. Soc.*, **122**, 9071-9077.
8. Goodrich, T. T., Lee, H. J. and Corn, R. M. (2004). Direct detection of genomic DNA by enzymatically amplified SPR imaging measurements of RNA microarrays, *J. Am. Chem. Soc.*, **126**, 4086-4087.
9. Dostalek, J. and Knoll, W. (2008). Biosensors based on surface plasmon-enhanced fluorescence spectroscopy, *Biointerphases*, **3**, FD12-FD22.
10. Neumann, T., Johansson, M. L., Kambhampati, D. and Knoll, W. (2002). Surface-

plasmon fluorescence spectroscopy, *Adv. Funct. Mater.*, **12**, 575-586.
11. Liebermann, T. and Knoll, W. (2000). Surface-plasmon field-enhanced fluorescence spectroscopy, *Colloids Surf. A: Physicochem. Eng. Aspects*, **171**, 115-130.
12. Matveeva, E., Gryczynski, Z., Gryczynski, I., Malicka, J. and Lakowicz, J. R. (2004). Myoglobin immunoassay utilizing directional surface plasmon-coupled emission, *Anal. Chem.*, **76**, 6287-6292.
13. Yu, F., Persson, B., Lofas, S. and Knoll, W. (2004). Attomolar sensitivity in bioassays based on surface plasmon fluorescence spectroscopy, *J. Am. Chem. Soc.*, **126**, 8902-8903.
14. Kasry, A. and Knoll, W. (2006). Long range surface plasmon fluorescence spectroscopy, *Appl. Phys. Lett.*, **89**, 101106.
15. Dostalek, J., Kasry, A. and Knoll, W. (2007). Long range surface plasmons for observation of biomolecular binding events at metallic surfaces, *Plasmonics*, **2**, 97-106.
16. Wang, Y., Dostalek, J. and Knoll, W. (2009). Long range surface plasmon-enhanced fluorescence spectroscopy for the detection of aflatoxin M_1 in milk, *Biosens. Bioelectron.*, **24**, 2264-2267.
17. Sarid, D. (1981). Long-range surface-plasma waves on very thin metal-films, *Phys. Rev. Lett.*, **47**, 1927–1930.
18. Kasry, A., Dostalek, J. and Knoll, W. (2009) *Long range surface plasmon-enhanced fluorescence spectroscopy as a platform for biosensors*, in *Advanced surface design for biomaterial and life science applications*, A.T.A. Jenkins, R. Foersch, and H. Schoenherr, Editors. Wiley-VCH: Weinheim. p. 447-460.
19. Aulasevich, A., Roskamp, R. F., Jonas, U., Menges, B., J., D. and Knoll, W. (2009). Optical Waveguide Spectroscopy for the Investigation of Protein-Functionalized Hydrogel Films, *Macromol. Rapid Commun.*, **30**, 872-877.
20. Beines, P. W., Klosterkamp, I., Menges, B., Jonas, U. and Knoll, W. (2007). Responsive thin hydrogel layers from photo-cross-linkable poly(N-isopropylacrylamide) terpolymers, *Langmuir*, **23**, 2231-2238.
21. Knoll, W., Kasry, A., Yu, F., Wang, Y., Brunsen, A. and Dostalek, J. (2008). New concepts with surface plasmons and nano-biointerfaces, *J. Nonlinear Opt. Phys. Mater.*, **17**, 121-129.
22. Watt, K. W. L., P. J.; M'Timkulu, T.; Chan, W. P.; Loor, R. (1986). Human prostate-specific antigen: structural and functional similarity with serine proteases, *Proc. Nati. Acad. Sci. USA*, **83**, 3166-3170.
23. Acevedo, B., Perera, Y., Ruiz, M., Rojas, G., Benitez, J., Ayala, M. and Gavilondo, J. (2002). Development and validation of a quantitative ELISA for the measurement of PSA concentration, *Clin. Chim. Acta*, **317**, 55-63.
24. Radowicki, S., Kunicki, M. and Bandurska-Stankiewicz, E. (2008). Prostate-specific antigen in the serum of women with benign breast disease, *European Journal of Obstetrics Gynecology and Reproductive Biology*, **138**, 212-216.
25. Doherty, A. P., Bower, M., Smith, G. L., Miano, R., Mannion, E. M., Mitchell, H. and Christmas, T. J. (2000). Undetectable ultrasensitive PSA after radical prostatectomy for prostate cancer predicts relapse-free survival, *British Journal of Cancer*, **83**, 1432-1436.
26. Johnson, E. D. and Kotowski, T. M. (1993). Detection of Prostate Specific Antigen by Elisa, *Journal of Forensic Sciences*, **38**, 250-258.
27. Lind, K. and Kubista, M. (2005). Development and evaluation of three real-time immuno-PCR assemblages for quantification of PSA, *J. Immunol. Meth.*, **304**, 107-116.
28. Nam, J. M., Thaxton, C. S. and Mirkin, C. A. (2003). Nanoparticle-based bio-bar codes for the ultrasensitive detection of proteins, *Science*, **301**, 1884-1886.
29. Grubisha, D. S., Lipert, R. J., Park, H. Y., Driskell, J. and Porter, M. D. (2003). Femtomolar detection of prostate-specific antigen: An immunoassay based on surface-enhanced Raman scattering and immunogold labels, *Anal. Chem.*, **75**, 5936-5943.
30. Yu, F., Persson, B., Lofas, S. and Knoll, W. (2004). Surface plasmon fluorescence immunoassay of free prostate-specific antigen in human plasma at the femtomolar level, *Anal. Chem.*, **76**, 6765-6770.

31. Brunsen, A., Jonas, U., Dostalek, J., Menges, B. and Knoll, W. (2009). Synthesis and Characterization of a photocrosslinkable Dextran-based Hydrogel as Biosensor Matrix, In preparation.
32. Aspnes, D. E. (1982). Optical properties of thin films, *Thin Solid Films*, **89**, 249-262.
33. Piehler, J., Brecht, A., Hehl, K. and Gauglitz, G. (1999). Protein interactions in covalently attached dextran layers, *Colloids Surf. B*, **13**, 325-336.
34. Lofas, S., Johnsson, B., Edstrom, A., Hansson, G., Linquist, G., Muller, R. and Stigh, L. (1995). Methods for Site Controlled Coupling to Carboxymethyldextran Surfaces in Surface-Plasmon Resonance Sensors, *Biosens. Bioelectron.*, **10**, 813-822.
35. Schuck, P. (1997). Use of surface plasmon resonance to probe the equilibrium and dynamic aspects of interactions between biological macromolecules, *Annu. Rev. Biophys. Biomol. Struct.*, **26**, 541-566.
36. Huang, C. J., Jonas, U., Dostalek, J. and Knoll, W. (2009). Biosensor platform based on surface plasmon-enhanced fluorescence spectroscopy and responsive hydrogel binding matrix, *Proc. SPIE*, **7356**, 735625.

Chapter 6 Biosensor Based on Hydrogel Optical Waveguide Spectroscopy

Abstract

A novel label-free biosensor based on the measurement of binding-induced refractive index changes by hydrogel optical waveguide spectroscopy (HOWS) is reported. This biosensor is implemented by using a surface plasmon resonance (SPR) optical setup in which a carboxylated poly(*N*-isoproprylacrylamide) (PNIPAAm) hydrogel film is attached on a metallic surface and modified by protein catcher molecules through amine coupling chemistry. The swollen hydrogel with micrometer thickness serves both as a binding matrix and optical waveguide. We show that compared to regular SPR biosensor with thiol self-assembled monolayer (SAM), HOWS provides an order of magnitude improved resolution in the refractive index measurements and enlarged binding capacity owing to its low damping and large swelling ratio, respectively. A model immunoassay experiment revealed that HOWS allowed detection of IgG molecules (molecular weight 150 kDa) with a 10 pM limit of detection that was five-fold lower than that achieved for SPR with thiol SAM. For the high capacity hydrogel matrix, the affinity binding was mass transport limited. Therefore, we envisage that HOWS will provide further improved detection limit for low molecular weight analytes or for assays employing lower affinity catcher molecules.

6.1 Introduction

Rapid and sensitive detection of chemical and biological analytes becomes increasingly important in areas such as medical diagnostics, food control and environmental monitoring. Among various technologies, optical biosensors allowing direct detection of target analytes without the need of additional labels are pushed forward for the applications in these areas [1, 2]. Up to now, a wide range of refractometric-based biosensor platforms relying on the measurement of molecular binding-induced refractive index changes were developed including surface plasmon resonance (SPR) [3], grating-coupled integrated optical waveguides (grating coupler) [4, 5], spectroscopy of leaky dielectric waveguides (resonant mirror) [6-8] and integrated optical Mach-Zehnder interferometer [9]. These devices typically comprise a metallic or dielectric layer structure supporting an optical guided wave that probes the binding of target molecules contained in a sample to catcher molecules immobilized on a sensor surface. The molecular binding events are detected through the induced variations in the characteristics of the optical guided wave. The catcher molecules can be immobilized by using two-dimensional surface architectures such as those based on self-assembled monolayers (SAM) [10-12] or in three-dimensional matrices based on polymers [13, 14] or inorganic nanoscale porous dielectric films [15]. Three-dimensional hydrogel binding matrices in which catcher molecules are attached to flexible polymer chains offer an increased sensor response to the affinity binding of target molecules owing to the larger binding capacity and lower steric hindrance compared to the two-dimensional surface architectures.

Recently, carboxylated photocrosslinkable hydrogel polymer networks based on poly(*N*-isopropylacrylamide) (PNIPAAm) and dextran copolymers were synthesized in our laboratory for high capacity binding matrices in surface plasmon resonance (SPR) and surface plasmon-enhanced fluorescence spectroscopy (SPFS) biosensors [16-19]. These hydrogels highly swell in aqueous environment and form stable films with thicknesses up to several micrometers. If attached to a metallic surface, these films can serve as optical waveguides which exhibit more than an order of magnitude lower damping than surface plasmons [17, 20]. In this paper, we show that the hydrogel optical waveguide spectroscopy (HOWS) allows monitoring the variations of refractive index on the sensor surface with greatly increased accuracy compared to regular SPR. Moreover, a thin hydrogel film can serve both as a waveguide and as an affinity binding matrix and thus it provides full

overlap of the electromagnetic field of a probing wave with the region where molecular binding events occur. The performance of HOWS is characterized by means of a refractometric study and its implementation for label-free biosensing is demonstrated through a model immunoassay experiment. The obtained results are compared to those measured by regular SPR biosensor relying on thiol SAM surface architecture.

6.2 Materials and methods

6.2.1 Materials

All reagents were used as received without further purification. Mouse immunoglobulin G (IgG) and goat anti-mouse immunoglobulin G (a-IgG) were obtained from Invitrogen (Camarillo, CA). 1-ethyl-3-(3-dimethylaminopropyl)carbodiimide (EDC) and *N*-hydroxysuccinimide (NHS) were from Pierce (Rockford, USA). Phosphate buffered saline (PBS, 140 mM NaCl, 10 mM phosphate, 3 mM KCl, and a pH of 7.4) was purchased from Calbiochem (Darmstadt, Germany). 10 mM acetate buffer (ACT), pH 4, was prepared with sodium acetate and acetic acid by adjusting the pH with HCl and NaOH. Series of buffers with pH between 4 and 7 were prepared by adding HCl or NaOH to a solution of 1.25 mM citric acid, 1.25 mM potassium dihydrogen phosphate, 1.25 mM dipotassium phosphate, 1.25 mM tris-(hydroxymethyl)-aminomethane hydrochloride and 1.25 mM potassium chloride. PBS-Tween buffer (PBST) was prepared by adding Tween 20 (0.05%) in PBS buffer solution. Dithiolaromatic PEG6-carboxylate (thiol-COOH) and dithiolaromatic PEG3 (thiol-PEG) were purchased from SensoPath Technologies (Bozeman, USA). Sodium *para*-tetrafluorophenol-sulfonate (TFPS) and S-3-(benzoylphenoxy)propyl ethanthioate (thiol-benzophenone) were synthesized at the Max Planck Institute for Polymer Research in Mainz, Germany as described in the literature [17, 21]. All the other chemicals were purchased from Sigma-Aldrich (Schnelldorf, Germany).

6.2.2 Surface architecture

The synthesis and deposition of the PNIPAAm hydrogel that is composed of the terpolymer with N-isoproprylacrylamide, methacrylic acid, and 4-methacryloyl benzophenone was performed in our laboratories, as described elsewhere [17]. Briefly, a thin hydrogel film was spin-coated (from an ethanol solution with polymer dissolved at the concentration of 20 mg mL^{-1}) on a sensor chip surface with thin gold layer that was

modified by a thiol-benzophenone SAM. Afterwards, the polymer film was dried overnight in vacuum at 50 ℃ followed by irradiation with UV light (λ = 365 nm, irradiation dose of 2 J cm^{-2}) in order to cross-link and attach the polymer chains to the gold surface via benzophenone units. The immobilization of mouse IgG catcher molecules in the PNIPAAm hydrogel matrix was performed *in situ*. Firstly, the hydrogel was swollen in ACT buffer and the hydrogel carboxylic moieties were activated by 20-minute incubation in water solution with a mixture of TFPS (10.5 mg mL^{-1}) and EDC (37.5 mg mL^{-1}). Then, the surface was rinsed with ACT buffer for 5 minutes and mouse IgG dissolved in ACT buffer at a concentration of 50 μg mL^{-1} was flowed over the activated hydrogel film for 90 minutes. After the reaction of mouse-IgG with TFPS-activated carboxylic groups, the un-reacted TFPS ester moieties were blocked by 20-minute incubation in a solution with 1 M ethanolamine at pH 8.5. Finally, the functionalized hydrogel was successively washed with ACT and PBST buffers for 5 and 10 min, respectively. For comparison, a regular SPR sensor chip with a thin gold layer and mouse IgG molecules immobilized by using a mixed thiol SAM was used. The thiol SAM was formed on a gold surface during overnight incubation in a mixture of thiol-COOH and thiol-PEG (ratio of 1:9) dissolved in absolute ethanol at a total concentration of 0.5 mM. Afterwards, the gold surface was rinsed with ethanol and activated with EDC (37.5 mg mL^{-1}) and NHS (10.5 mg mL^{-1}) solution, and the mouse IgG molecules were immobilized similarly as described for the hydrogel binding matrix. In a control experiment, the carboxylic moieties of the hydrogel film and the SAM were activated as described above and directly deactivated with ethanolamine without binding of IgG molecules.

6.2.3 Spectroscopy of hydrogel waveguide modes

The HOWS biosensor was implemented by using an optical setup depicted in Figure 6.1, the same as the SPR setup as described in section 3.1.1. The sensor chip consisted of a glass slide coated with a gold layer (thickness between 37 and 45 nm) and a PNIPAAm hydrogel film. A cell with the volume 10 μL, length L = 10 mm and depth h = 0.1 mm was pressed against the sensor chip surface to flow liquid samples over the sensor surface at the flow rate of 200 μL min^{-1}. For the comparison study, the regular SPR sensor chip

with 45 nm gold and thiol SAM was loaded to the sensor. The assembly of the prism, sensor chip and flow-cell was mounted on a rotation stage to control the angle of incidence of a laser beam θ (measured outside the prism, see Figure 6.1). The reflectivity signal R was determined as a ratio of light intensity reflected from a sensor chip and from a reference blank glass slide. The variations in the reflectivity signal R were acquired with a typical standard deviation $\sigma(R)$ between 7×10^{-5} and 2×10^{-4}.

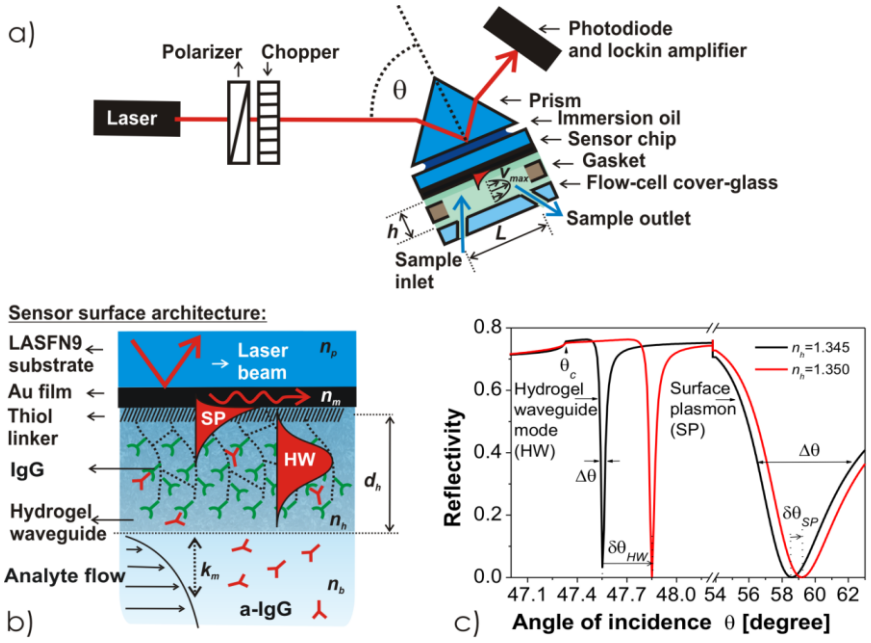

Figure 6.1 a) Optical setup for the excitation of hydrogel waveguide (HW) and surface plasmon (SP) modes, b) scheme of the sensor surface architecture and c) simulated changes in the angular reflectivity spectra for the resonant excitation HW and SP modes due to the refractive index increase $\Delta n_h = 5\times10^{-3}$ for a hydrogel film with the thickness d_h = 1.7 μm and refractive index n_h = 1.345.

The evanescent field of a laser beam that is totally internally reflected at the sensor surface penetrates through the gold layer and can couple to surface plasmon (SP) and hydrogel waveguide (HW) modes propagating along the outer metal interface. As Figure 6.1 shows, the excitation of SP and HW modes is manifested as two distinct dips in the angular reflectivity spectrum. These dips are located at angles θ for which the propagation constant of the mode β matches the component of the reflected laser beam propagation constant that is parallel to the interface as the equation (2.15). The propagation constant β of SP and HW can be determined from the analytical dispersion relation as the equation (2.13). Further, the resonance coupling angle for HW mode is noted as θ_{HW} and the one for surface plasmons as θ_{SP}. Both coupling angles increase when increasing the refracting

index of the dielectric adjacent to the gold surface n_h. In the further time resolved experiments, the angle of incidence θ was set to the location with highest slope $\partial R/\partial\theta$ at the edge of the HW or SP reflectivity dip below the resonant angles θ_{HW} and θ_{SPR}, respectively. A shift in the resonant dips due to the refractive index variations δn_h was measured from induced changes in the reflected intensity δR. In order to determine the thickness d_h and the refractive index n_h of the hydrogel film binding matrix, the angular reflectivity spectrum exhibiting SP and HW resonance dips was fitted by transfer matrix-based model (implemented in the software Winspall developed at the Max Planck Institute for Polymer Research in Mainz, Germany). The diffusion rate k_m of molecules contained in a sample to the sensor surface was estimated by using the two compartment model [22]. For a flow-cell with the depth h and length L through which a sample flows with the maximum velocity v_{max}, the diffusion rate k_m can be expressed as (2.24). By using Stokes formula (2.22), the diffusion constant for the IgG protein in water was determined as $D = 2 \times 10^{-5}$ mm^{2}s^{-1} [23].

6.3 Results and discussion

6.3.1 Characterization of hydrogel thin film

Firstly, a hydrogel film attached to the gold surface was characterized by the spectroscopy of HW and SP modes. The angular reflectivity spectra $R(\theta)$ were measured for a hydrogel film in contact with air and after its swelling in PBS (see Figure 6.2). By fitting the two distinct resonances at θ_{HW} = 21.9 deg and θ_{SP} = 76 deg that are associated with the excitation of HW and SP modes in a dry polymer layer, respectively, its thickness d_h = 230 nm and refractive index $n_{h\text{-}dry}$ = 1.48 was determined. After the swelling in PBS buffer, the HW and SP coupling angles shifted to θ_{HW} = 47.75 deg and θ_{SP} = 58.20 deg, respectively. The fitting of corresponding reflectivity spectrum revealed that the thickness of the swollen gel increased to d_h = 1.86 μm and the refractive index decreased to n_h = 1.3454. This refractive index is very close to that of the PBS buffer n_b = 1.3340 and it corresponds to the polymer volume fraction of 8 % and swelling ratio 12.5 as estimated by using the effective medium theory [24], equation (2.52). Let us note that for the HOWS the thickness of the hydrogel film needs to be higher than so called cut-off thickness (typically $d_h > 1$ μm) below which the hydrogel waveguide modes cease to exist.

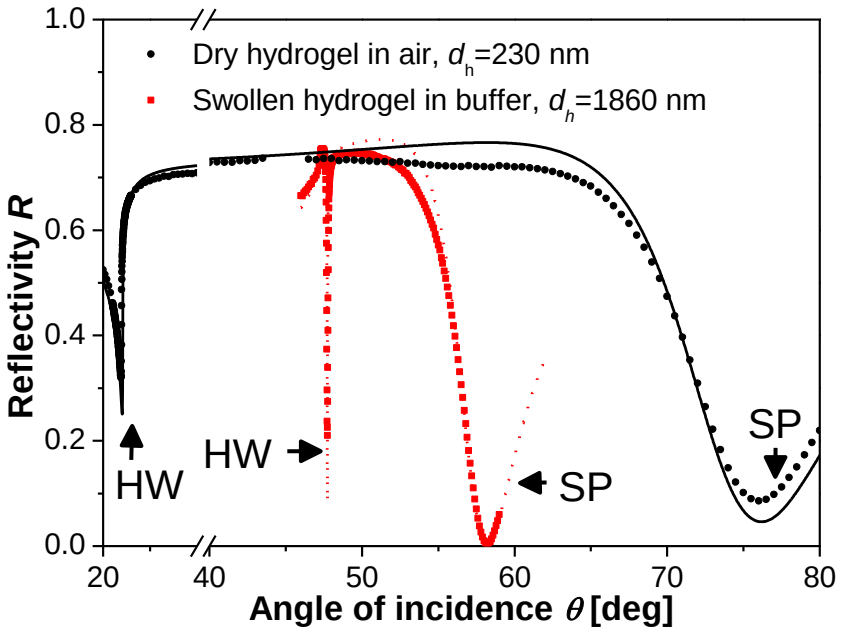

Figure 6.2 Angular reflectivity spectra measured for the hydrogel film in contact with air (black circles) and swollen in PBS (red squares). The spectra were fitted with transfer matrix-based model as indicated by lines.

6.3.2 Refractometric study of HOWS sensor

A refractometric study was performed in order to compare the accuracy with which the refractive index changes on the sensor surface can be measured by HOWS and SPR. In this experiment, changes in the reflectivity spectra were measured upon flowing a series of liquid samples with increasing n_b. These samples were prepared by spiking the PBS buffer (n_b = 1.3334) with ethylene glycol (refractive index n = 1.4314) at concentrations between 0 and 8% (refractive index changes linear with the concentration of EG with the slope $\delta n_b = 9.8 \times 10^{-4}$ RIU per % at the wavelength λ = 633 nm and room temperature). As seen in Figure 6.3a, resonant dips associated with the excitation of HW and SP modes shift towards higher angles of incidence when the refractive index n_b of a liquid at the sensor surface increases. The fitting of the measured reflectivity spectra with a transfer matrix-based model revealed that the hydrogel thickness d_h was between 1.86 and 1.91 μm and its index n_h linearly increased with the bulk refractive index of the sample with a slope of dn_h/dn_b = 0.89. These results indicate that approximately 90% of the hydrogel volume was accessible for EG molecules diffusing from the aqueous phase into the hydrogel film which is in agreement with the lower maximum shift of HW resonance

angle (0.64 deg) compared to the corresponding critical angle shift (0.68 deg) (see Figure 6.3a). The sensitivity to bulk refractive index changes δn_b was determined as equation (2.38) $S = \delta\theta/\delta n_b$, where $\delta\theta$ is the angular shift of the reflectivity dip. The HOWS exhibited a sensitivity of S = 81 deg RIU^{-1} that is 1.3-fold lower than the one measured for SPR S = 106 deg RIU^{-1}. However, the full width in the half minimum (FWHM) of the HW resonance dip was of $\Delta\theta$ = 0.1 deg which is approximately 50-fold lower compared to that of the SP dip of $\Delta\theta$ = 5.1 deg. In refractometric sensors based on spectroscopy of guided waves, the figure of merit defined as $\chi = S/\Delta\theta$ is inversely proportional to the resolution with which the refractive index variations can be measured [25]. By comparing the figure of merit of HOWS (χ = 810) with that of SPR (χ = 20.8), we estimated that HOWS can allow measurement of the refractive index variations on the sensor surface with an accuracy improved by a factor of about 40 with respect to regular SPR. Figure 6.3b shows the time evolution of HOWS and SPR reflectivity signal R measured upon the successive flow of PBS samples spiked with EG at concentrations of 0 %, 0.125 % (δn_b = 1.23×10^{-4} RIU), 0.25 % (δn_b = 2.45×10^{-4} RIU), 0.375 % (δn_b = 3.68×10^{-4} RIU) and 0.5% (δn_b = 4.9×10^{-4} RIU). These data show that the reflectivity signal changed with a slope of dR/dn_b of 78 and 5.6 per RIU for HOWS and SPR-based measurements, respectively, which translated to 10 fold higher refractive index resolution provided by HOWS (1.3×10^{-6} RIU) compared to that of SPR (1.3×10^{-5} RIU) (defined as the ratio of standard deviation $\sigma(R)$ and the slope dR/dn_b, as equation (2.43)). This factor is lower than that predicted by the previous comparison of figure of merit due to the lower coupling efficiency to HOW modes and due to the non-symmetrical SPR resonance dip which exhibited higher slope below the resonant angle θ_{SPR} than that above it.

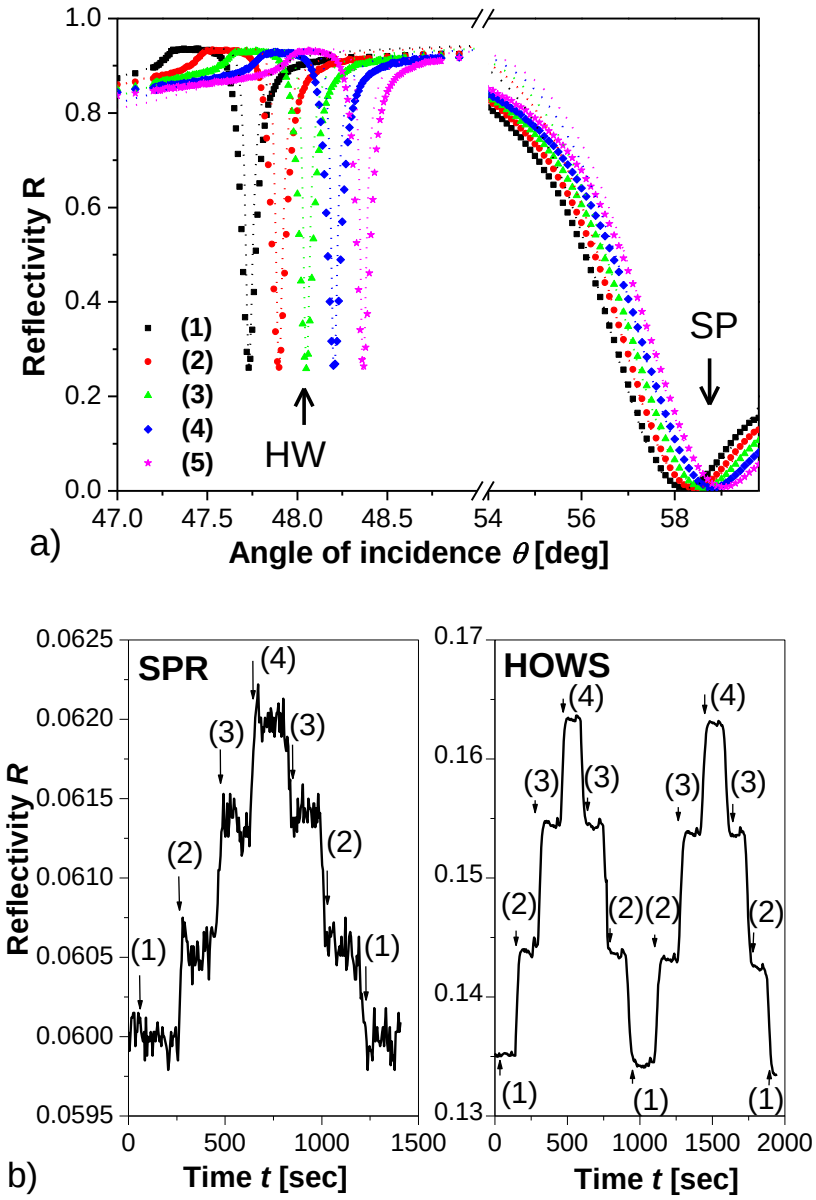

Figure 6.3 a) Measured angular reflectivity spectra for a hydrogel waveguide film in contact with PBS buffer spiked with ethylene glycol (EG) at the concentration from (1) 0, (2) 2%, (3) 4%, (4) 6% and (5) 8%. The fitted spectra are shown as dotted line. b) Comparison of the time evolution of the sensor signal measured by SPR and HOWS upon the successive injections of the PBS buffer spiked with EG at concentrations of (1) 0.125%, (2) 0.25%, (3) 0.375%, (4) 0.5%.

6.3.3 Sensitivity to swelling changes of HOWS sensor

As shown in previous studies, changes in swelling of PNIPAAMm hydrogel films occur

upon the binding of biomolecules [16, 19] as well as due to variations in the ionic strength and pH [17, 19, 26] which may interfere with the response due to the specific capture of target analyte [27]. In general, the binding of target molecules as well as the swelling variations alter the thickness d_h and consequently refractive index n_h of the hydrogel film leading to a shift of the angular position of resonant dip associated with the excitation of hydrogel waveguide and surface plasmon modes. The sensitivity of HOWS and SPR to swelling changes of a binding matrix was investigated in an experiment in which buffers with pH between 4 and 7 were flowed over the hydrogel film. As seen in Figure 6.4a, decreasing the pH causes an increase of the resonant angle θ_{SP} and a decrease of the resonant angle θ_{HW}. The fitting of measured angular reflectivity spectra presented in Figure 6.4a revealed that the decrease of pH caused a collapse of the gel upon which the thickness decreased from d_h = 2600 nm (pH = 7) to d_h = 1400 nm (pH = 4). Let us note that in this experiment the surface mass density of the gel (Γ = 105 ng mm^{-2}) did not change upon the swelling and that the increased coupling efficiency observed for HW mode propagating along the hydrogel film with the lower thickness is caused by a stronger overlap of the field of the excitation incident wave and HW. In Figure 6.4b, the experimental dependence of the resonant angles θ_{HW} and θ_{SP} on the thickness of the gel is compared to simulations based on transfer matrix model. These data reveal good agreement between theory and experiment and show that changes in θ_{HW} due to the swelling variations are an order of magnitude lower than those for θ_{SP}. In addition, the simulations show that the derivation $\partial\theta_{HW}/\partial d_h$ can reach zero for the certain thickness d_h which illustrates that the sensitivity of θ_{HW} to small swelling variations can be totally eliminated by a design of the hydrogel binding matrix. This is an important feature of HOWS as the regular SPR exploiting a three dimensional binding matrix does not allow distinguishing between the surface mass density and swelling changes.

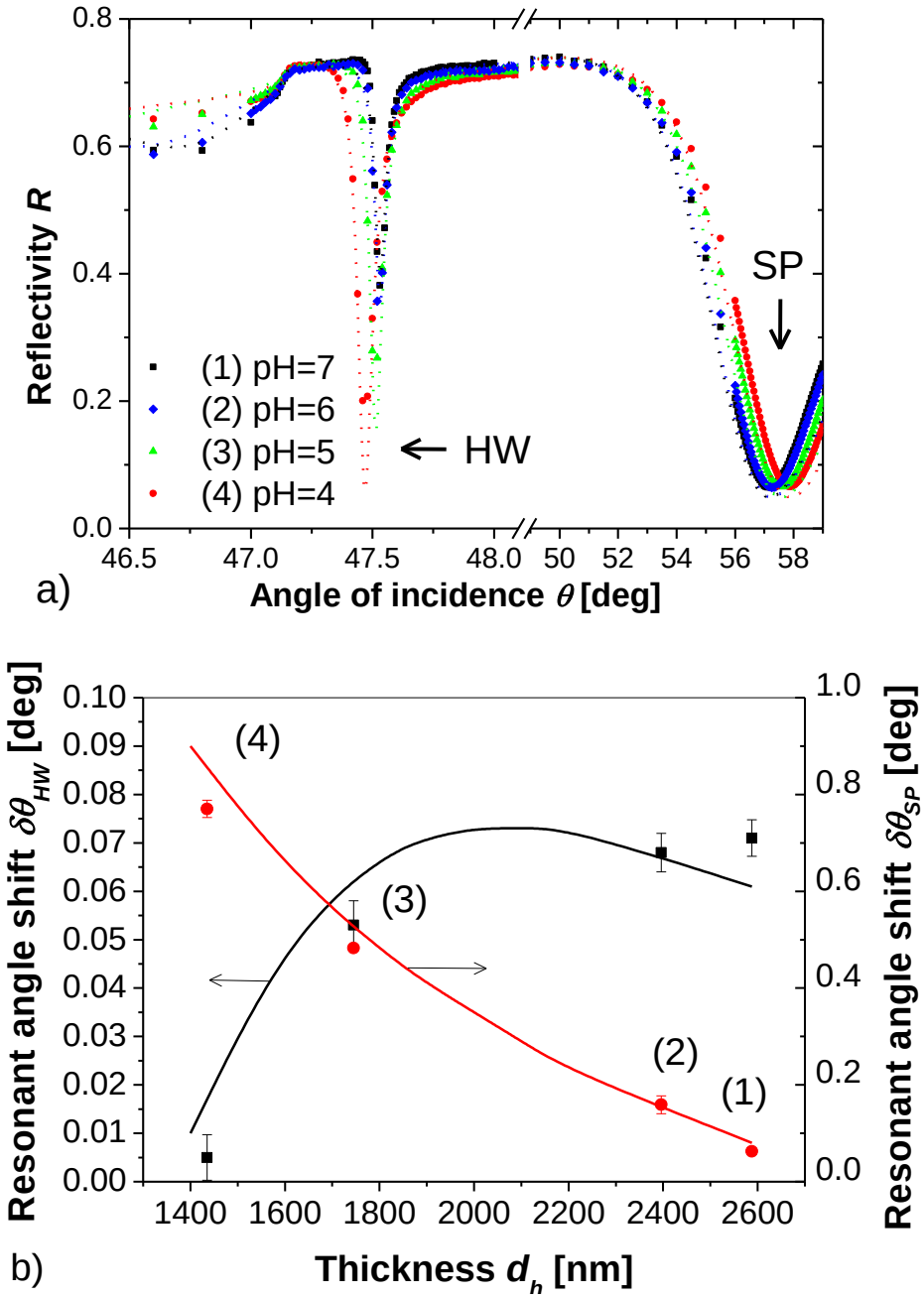

Figure 6.4 a) Angular reflectivity spectra for a hydrogel film measured in buffer with pH value of (1) 7, (2) 6, (3) 5, (4) 4. b) The dependence of the resonance angle for the excitation of HW and SP modes on the thickness of the hydrogel observed experimentally (dots) and obtained from transfer matrix-based simulations (line).

6.3.4 Immobilization of catcher biomolecules

In order to demonstrate the application of HOWS for the monitoring of molecular binding events, IgG catcher molecules were firstly immobilized to the PNIPAAm

hydrogel. As seen in Figure 6.5a, the covalent coupling of IgG to the gel shifted the angular position of the resonant dip from θ_{HW} = 47.68 deg to 47.80 deg. By fitting the changes in the angular reflectivity spectra, we determined that the surface mass density increased due to the loading of IgG molecules in the hydrogel from Γ = 98 ng mm^{-2} to 118 ng mm^{-2}. After the blocking the un-reacted TFPS groups by ethanolamine and rinsing with PBS, the surface mass density decreased to Γ = 114 ng mm^{-2}. This decrease can be attributed to the release of loosely bound polymer chains and IgG molecules from the hydrogel film. By comparing the surface mass density before and after the loading with IgG molecules, the surface coverage of the immobilized IgG can be estimated as $\Delta\Gamma$=16-20 ng mm^{-2}. The immobilization of IgG on a gold surface by using thiol SAM with carboxylic moieties resulted in the surface coverage of $\Delta\Gamma$=1.7 ng mm^{-2} as determined by the analysis of the angular reflectivity spectra in Figure 6.5b.

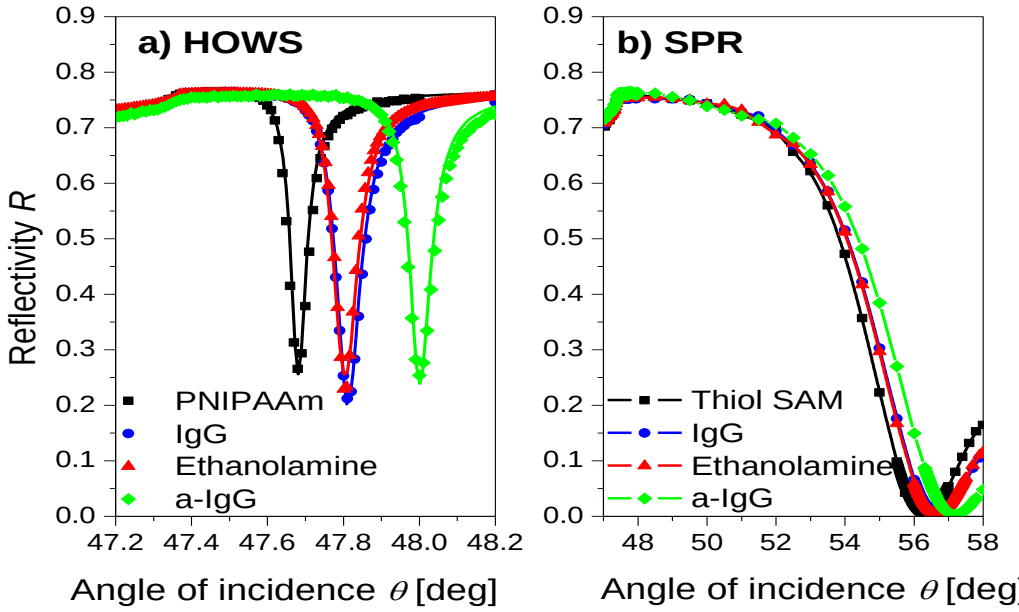

Figure 6.5 Angular reflectivity spectra of a) a hydrogel film and b) thiol SAM in contact with PBST buffer (black squares), after the immobilization of catcher molecules (blue circles, IgG), incubation in ethanolamine (red triangles) and saturation of affinity binding of analyte molecules (green diamonds, a-IgG), measured by a) HOWS and b) SPR, respectively.

6.3.5 Immunoassays-based HOWS biosensing

The affinity binding of a-IgG molecules was observed upon a sequential injection of a series of samples with a-IgG dissolved in PBST at concentrations ranging from 0.6 nM to 0.6 μM. Each sample was flowed over the sensor surface with immobilized catcher molecules for 30 minutes followed by a 10-minute rinsing with PBST buffer. As seen in the Figure 6.6a, the capture of a-IgG molecules during a sample flow was manifested as a gradual increase in the HOWS and SPR reflectivity signal δR due to the affinity binding-increased refractive index on the surface. In a control experiment, no measurable increase signal δR was observed for a flow of 6 and 60 nM a-IgG over the surfaces that were not modified with IgG molecules. The calibration curve showing the dependence of the reflectivity changes on the concentration of a-IgG in a sample is presented in Figure 6.6b. The results show that the LOD for the detection of a-IgG on the SAM-based SPR is 50 pM, which is comparable to the calculated results (17 pM) as described in section 2.2.3.2. These data reveal that the reflectivity changes δR observed by HOWS were larger compared to SPR and allowed for the detection of a-IgG with 5-fold improved limit of detection (LOD) of 10 pM. The limit of detection was determined as the concentration for which the calibration curve reaches the three-time standard deviation of reflectivity signal baseline $3\sigma(R)$. To observe the binding capacity of the sensor, a solution with a-IgG molecules at the concentration of 0.6 μM was flowed over the sensor surface until the sensor response was stabilized. The sensor response stabilized much slower for hydrogel binding matrix (the slope $\partial R/\partial t$ decreased 50-fold after 200 minutes) compared to SPR with monolayer surface architecture (after 17 minutes). From the induced shifts $\delta\theta_{SPR}$ = 0.55 deg measured by SPR and $\delta\theta_{HW}$ = 0.19 deg obtained by HOWS (Figure 6.5), the amount of captured a-IgG was determined as 2.6 and 36 ng mm^{-2} on the thiol SAM and in the hydrogel, respectively. The HOWS angular shift was too large to be measured by tracking the reflectivity change δR. Therefore, the corresponding reflectivity change was estimated as $\delta R_{HW} = \delta\theta_{HW} \times \partial R/\partial\theta$ = 1.72 which is 14.3-fold larger than that measured by SPR of δR_{SPR} = 0.12. The reason for the slow saturation of the HOWS signal and for only five-fold improvement of LOD is owing to the slow diffusion of the analyte to the sensor surface. The mass transport coefficient of the a-IgG molecules to the hydrogel surface was calculated as $k_m \sim 3 \times 10^{-3}$ mm s^{-1} by using the equation (3). By fitting the measured SPR kinetics $R(t)$ with the Langmuir adsorption model (data not shown), the association

rate constant for the a-IgG/IgG pair was estimated as $k_a > 10^5$ M^{-1} s^{-1}. For the receptor surface coverage in the hydrogel of $\Delta\Gamma \sim 1.3\times10^{-13}$ mol mm^{-2} (corresponding to IgG surface mass density of $\Delta\Gamma$ = 20 ng mm^{-2} determined previously and to the molecular weight of IgG 150 kDa), the affinity binding rate of $k_a\Delta\Gamma > 10^{-2}$ mm s^{-1} is obtained that is more than three times higher than k_m and which confirms that the molecular binding was diffusion controlled.

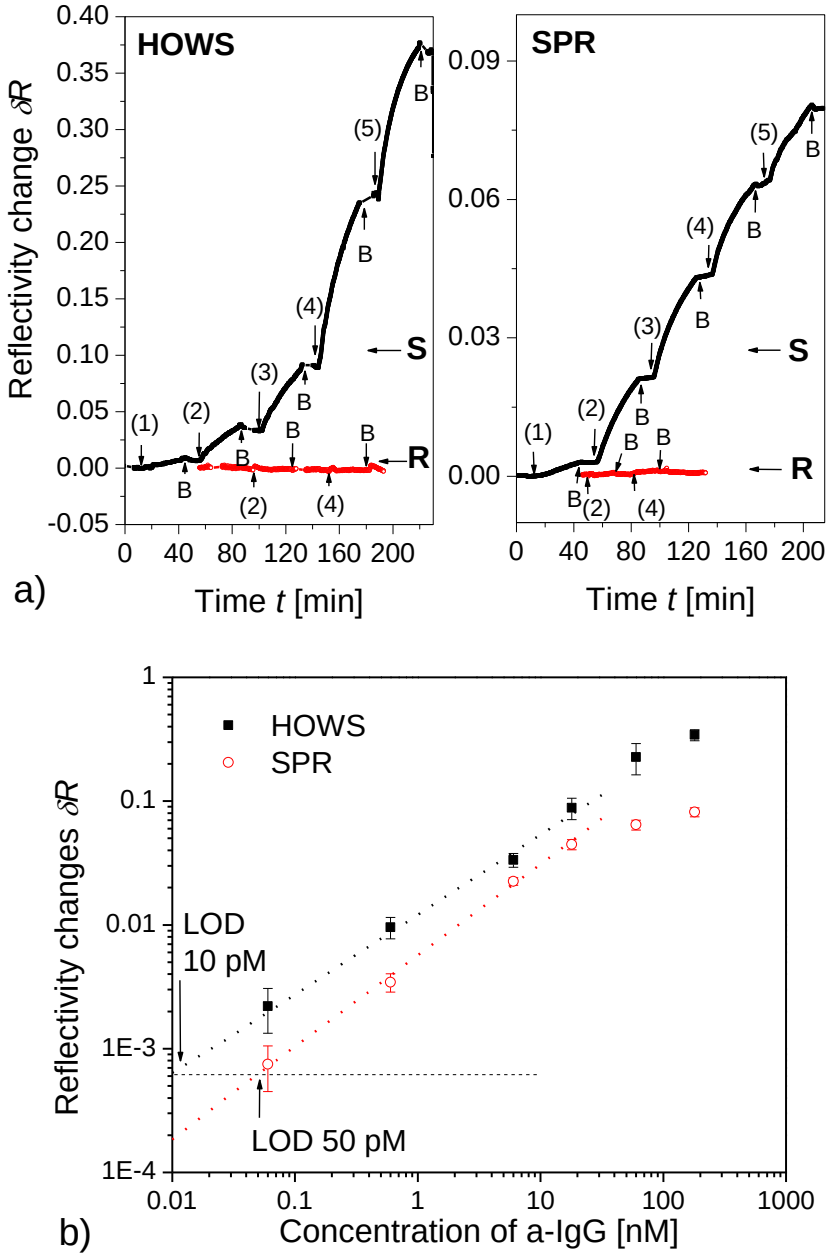

Figure 6.6 a) The time kinetics of the SPR and HOWS reflectivity changes ΔR due to the affinity binding of analyte a-IgG molecules dissolved at the concentration of (1) 0.6, (2) 6, (3) 18, (4) 60 and (5) 180 nM flowed over the sensor surface, modified with IgG catcher molecules (S) and a reference

surface without IgG molecules (R). In between injections of samples, the sensor surface was rinsed with PBST buffer (B). b) The calibration curves for the detection of anti-IgG measured by HOWS (black squares) and SPR (red circles) fitted with linear function (correlation coefficients 0.9913 (n = 4) and 0.9961 (n = 4), respectively).

6.4 Conclusions

A new biosensor for direct label-free detection of molecular analytes based on a three-dimensional hydrogel binding matrix and the spectroscopy of hydrogel waveguide modes was presented. This biosensor was implemented by using an optical setup for angular spectroscopy of guided waves and UV-crosslinkable carboxylated PNIPAAm hydrogel in which catcher molecules were immobilized by amine coupling chemistry. With respect to regular SPR biosensor, HOWS was demonstrated to provide an order of magnitude enhanced resolution in the measurement of refractive index changes, binding capacity, and equilibrium sensor response due to the affinity binding of target molecules. For immunoassay-based observation of affinity binding of 150 kDa IgG target molecules, HOWS allowed a 10 pM limit of detection that was improved by a lower factor of five due to diffusion-limited mass transport to the surface. We expect that HOWS will enable higher sensitivity enhancement for detection of small molecules that can diffuse faster to the surface or for assays that exploit low affinity catcher molecules e.g. for continuous monitoring of target analytes [28]. The future work will include employing more advanced optical schemes and data processing methods for tracking of the angular resonance position [29]. In addition, the presented method can be straightforward extended for multi-analyte and reference-compensated measurements on arrays of sensing spots defined on the sensor chip by crosslinking of the hydrogel by UV through appropriate mask.

References

1. Fan, X. D., White, I. M., Shopoua, S. I., Zhu, H. Y., Suter, J. D. and Sun, Y. Z. (2008). Sensitive optical biosensors for unlabeled targets: A review, *Analytica Chimica Acta*, **620**, 8-26.
2. Gauglitz, G. (2005). Direct optical sensors: principles and selected applications, *Analytical and Bioanalytical Chemistry*, **381**, 141-155.
3. Liedberg, B., Nylander, C. and Lundstrom, I. (1983). Surface-Plasmon Resonance for

Gas-Detection and Biosensing, *Sensors and Actuators*, **4**, 299-304.
4. Clerc, D. and Lukosz, W. (1997). Direct immunosensing with an integrated-optical output grating coupler, *Sensors and Actuators B-Chemical*, **40**, 53-58.
5. Tiefenthaler, K. and Lukosz, W. (1989). Sensitivity of Grating Couplers as Integrated-Optical Chemical Sensors, *Journal of the Optical Society of America B-Optical Physics*, **6**, 209-220.
6. Buckle, P. E., Davies, R. J., Kinning, T., Yeung, D., Edwards, P. R., Pollardknight, D. and Lowe, C. R. (1993). The Resonant Mirror - a Novel Optical Sensor for Direct Sensing of Biomolecular Interactions .2. Applications, *Biosensors & Bioelectronics*, **8**, 355-363.
7. Skivesen, N., Horvath, R., Thinggaard, S., Larsen, N. B. and Pedersen, H. C. (2007). Deep-probe metal-clad waveguide biosensors, *Biosensors & Bioelectronics*, **22**, 1282-1288.
8. Zourob, M., Mohr, S., Brown, B. J. T., Fielden, P. R., McDonnell, M. B. and Goddard, N. J. (2005). Bacteria detection using disposable optical leaky waveguide sensors, *Biosensors & Bioelectronics*, **21**, 293-302.
9. Heideman, R. G. and Lambeck, P. V. (1999). Remote opto-chemical sensing with extreme sensitivity: design, fabrication and performance of a pigtailed integrated optical phase-modulated Mach-Zehnder interferometer system, *Sensors and Actuators B-Chemical*, **61**, 100-127.
10. Jung, L., Nelson, K., Stayton, P. and Campbell, C. (2000). Binding and dissociation kinetics of wild-type and mutant streptavidins on mixed biotin-containing alkylthiolate monolayers, *Langmuir*, **16**, 9421-9432.
11. Knoll, W., Liley, M., Piscevic, D., Spinke, J. and Tarlov, M. (1997). Supramolecular architectures for the functionalization of solid surfaces, *Adv Biophys*, **34**,
12. Knoll, W., Zizlsperger, M., Liebermann, T., Arnold, S., Badia, A., Liley, M., Piscevic, D., Schmitt, F. J. and Spinke, J. (2000). Streptavidin arrays as supramolecular architectures in surface-plasmon optical sensor formats, *Colloid Surf. A*, **161**, 115-137.
13. Lofas, S. and Johnsson, B. (1990). A Novel Hydrogel Matrix on Gold Surfaces in Surface-Plasmon Resonance Sensors for Fast and Efficient Covalent Immobilization of Ligands, *Journal of the Chemical Society-Chemical Communications*, 1526-1528.
14. Lofas, S., Johnsson, B., Edstrom, A., Hansson, G., Linquist, G., Muller, R. and Stigh, L. (1995). *Biosensors & Bioelectronics*, **10**, 813-822.
15. Rong, G., Najmaie, A., Sipe, J. E. and S.M., W. (2008). Nanoscale porous silicon waveguide for label-free DNA sensing, *Biosensors & Bioelectronics*, **23**, 1572-1576.
16. Aulasevich, A., Roskamp, R. F., Jonas, U., Menges, B., Dostalek, J. and Knoll, W. (2009). Optical Waveguide Spectroscopy for the Investigation of Protein-Functionalized Hydrogel Films, *Macromol. Rapid Commun.*, **30**, 872-877.
17. Beines, P. W., Klosterkamp, I., Menges, B., Jonas, U. and Knoll, W. (2007). Responsive thin hydrogel layers from photo-cross-linkable poly(N-isopropylacrylamide) terpolymers, *Langmuir*, **23**, 2231-2238.
18. Knoll, W., Kasry, A., Yu, F., Wang, Y., Brunsen, A. and Dostalek, J. (2008). New concepts with surface plasmons and nano-biointerfaces, *J. Nonlinear Opt. Phys. Mater.*, **17**, 121-129.
19. Wang, Y., Brunsen, A., Jonas, U., Dostalek, J. and Knoll, W. (2009). Prostate specific antigen biosensor based on long range surface plasmon-enhanced fluorescence spectroscopy and dextran hydrogel binding matrix, *Anal. Chem.*, **81**, 9625-9632.
20. Kuckling, D. and Pareek, P. (2008). Bilayer hydrogel assembly, *Polymer*, **49**, 1435-1439.
21. Gee, K. R., Archer, E. A. and Kang, H. C. (1999). 4-Sulfotetrafluorophenyl (STP) esters: New water-soluble amine-reactive reagents for labeling biomolecules, *Tetrahedron Letters*, **40**, 1471-1474.
22. Edwards, D. A., Goldstein, B. and Cohen, D. S. (1999). Transport effects on surface-volume biological reactions, *Journal of Mathematical Biology*, **39**, 533-561.
23. Stepamel, J., Vaisocherova, H. and Piliarik, M. (2006) *Molecular Interactions in SPR*

sensors, in *Surface Plasmon Resonance Based Sensors*, J. Homola, Editor. Springer: Heidelberg. p. 69-91.

24. Ghosh, S. K. and Pal, T. (2007). Interparticle coupling effect on the surface plasmon resonance of gold nanoparticles: From theory to applications, *Chem. Rev.*, **107**, 4797-4862.
25. Homola, J., Koudela, J. and Yee, S. S. (1999). Surface plasmon resonance sensors based on diffraction gratings and prism couplers: sensitivity comparisons, *Sensors and Actuators B-Chemical*, **54**, 16-24.
26. Huang, C. J., Jonas, U., Dostalek, J. and Knoll, W. (2009). Biosensor platform based on surface plasmon-enhanced fluorescence spectroscopy and responsive hydrogel binding matrix, *Proc. SPIE*, **7356**, 735625.
27. Xu, F., Persson, B., Lofas, S. and Knoll, W. (2006). Surface plasmon optical studies of carboxymethyl dextran brushes versus networks, *Langmuir*, **22**, 3352-3357.
28. Ohlson, S., Jungar, C., Strandh, M. and Madenjus, C. F. (2000). Continuous weak-affinity immunosensing, *Trends Biotechnol.*, **18**, 49-52.
29. Nenninger, G. G., Piliarik, M. and Homola, J. (2002). Data analysis for optical sensors based on spectroscopy of surface plasmons, *Measurement Science & Technology*, **13**, 2038-2046.

Chapter 7 Magnetic Nanoparticle-Enhanced Surface Plasmon Resonance Biosensing

Abstract

We present an approach for enhancing sensitivity of SPR biosensors based on magnetic iron oxide nanoparticles. The magnetic nanoparticles (MNPs) were modified with antibodies against a target analyte and served as a label enhancing the binding-induced refractive index changes and "vehicles" for rapid delivery of target analyte from a sample to the sensor surface by applied magnetic field. An optical setup based on grating-coupled SPR was employed with a magnet mounted bellow the sensor chip in order to collect magnetic nanoparticles on the sensor surface. Immunoassay for the detection of β human chorionic gonadotropin (βhCG) was implemented to investigate the sensitivity of grating-coupled SPR with MNPs. The sensitivities of detection formats including a) direct detection, b) sandwich immunoassay, c) MNPs immunoassay without and d) with applied magnetic field were compared. The role of mass transport of analyte to the sensor driven by diffusion (free analyte) and magnetic field gradient (analyte bound to MNPs) was studied. The results show that the MNPs enabled to improve the LOD of βhCG by 5 orders of magnitude with respect to the regular SPR sensor.

7.1 Introduction

Surface plasmon resonance (SPR) biosensors are intensively researched for rapid detection of analytes in applications of medical diagnostics, food control and environmental monitoring[1, 2]. This method offers the advantage of direct and label-free detection. However, SPR biosensors can typically analyze large and medium-size molecules at concentrations higher than nanomolar which is not sufficient for many applications. Therefore, approaches for increasing the sensitivity were pursued including those relying on antibodies-based bioassays with nanoparticles[3-7] and enzymes[8, 9]. For instance, gold nanoparticles offer an enhancement of refractive index changes[10] which can significantly amplify SPR signal and allowed achieving the detection limit of DNA strands at femtomolar level[11]. Recently, magnetic nanoparticles (MNPs) [5, 12] have been shown to improve the detection sensitivity of SPR[16] and other various analytical technologies relying on electrochemistry [13-15], fluorescence spectroscopy[16], magnetic resonance imaging (MRI)[17, 18] and bio-bar-code[19]. MNPs have desirable properties for SPR detection as they can serve for concentration/purification of analytes such as DNA[19] and RNA, protein, cells, bacteria[20, 21] and virus from complex samples, as well as for an enhancement of the refractive index changes[22].

In this chapter, a new approach is described based on grating-coupled SPR and MNPs immunoassay that allow manipulating the analyte on the sensor chip with applied magnetic field. Magnetic iron oxide nanoparticles coated by a shell layer with carboxylic groups were modified with antibodies and employed in an SPR biosensor. The antibody-conjugated MNPs served both as labels for enhancing refractive index changes as well as "vehicles" to rapidly deliver analyte from sample solution to the sensor surface by applying a gradient magnetic field. In this experiment, the detection of β human chorionic gonadotropin (βhCG) has been carried out in order to demonstrate the performance characteristics. Different detection formats including direct detection and sandwich assay with MNPs labels have been employed to investigate the contributions of MNPs to the limit of detection (LOD) and signal response. The implementation of MNPs to overcome the diffusion-limited mass transfer of analyte to the surface is discussed.

7.2 Materials and methods

7.2.1 Materials

Magnetic iron oxide nanoparticles modified with polysaccharide layer (fluidMAG-ARA with diameter of ~200 nm, magnetic core diameter of ~175 nm) were purchased from Chemicell (Berlin, Germany). βhCG monoclonal antibody (MAF05-627), βhCG monoclonal antibody (MAF05-043) and βhCG (A81455M) were obtained from Meridian Life Science (US). 1-ethyl-3-(3-dimethylaminopropyl)carbodiimide (EDC) and N-hydroxysuccinimide (NHS) were from Pierce (Rockford, USA). Dithiolaromatic PEG6-carboxylate (thiol-COOH) and dithiolaromatic PEG3 (thiol-PEG) were purchased from SensoPath Technologies (Bozeman, USA). 2-(N-Morpholino)ethanesulfonic acid (MES), PBS buffer tablets and Tween-20 were purchased from Sigma-Aldrich. PBS-Tween buffer (PBST) was prepared by adding Tween 20 (0.05%) in PBS buffer solution. Cylindrical magnets (NdFeB) with diameter of 10 mm and length of 25 nm were purchased from Neotexx (Berlin, Germany).

7.2.2 Optical setup and sensor chip

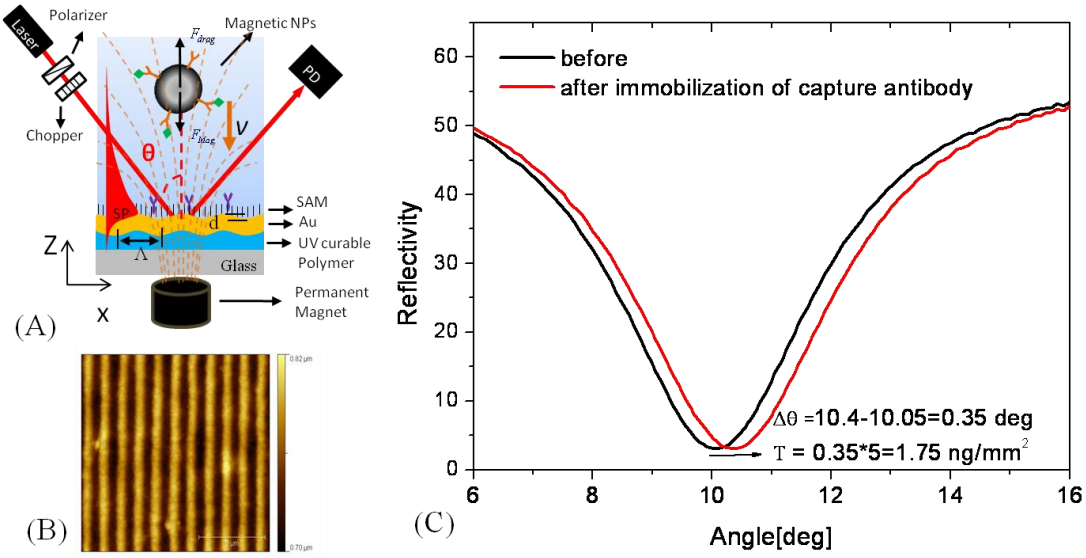

Figure 7.1 (A) Scheme of an optical setup and a sensor chip for the diffraction excitation of SPs. (B) AFM topography of a gold diffraction grating for the excitation of surface plasmon with period of Λ=520 nm and depth d= 58-64 nm (scale bar of 2 µm). (C) The angular spectra for the measurement of the gold diffraction grating modified with SAM before and after the immobilization of antibody.

There was used an SPR biosensor setup that is depicted in Figure 7.1A, which was described in detail in section 3.1.2. A cell with the volume 10 μL, length L=10 mm and depth h=0.1 mm was attached against the sensor chip to flow liquid samples at the flow rate of 503 μL min^{-1}. For the MNPs immunoassay, an external magnetic field with a gradient perpendicular to the surface dB/dz= 0.10 T mm^{-1} was applied by using a cylindrical magnet. The sensitivity of resonant angle to the changes of bulk refractive index was measured as $S_{\theta b}$ = 92 deg RIU^{-1}, and the slope $\delta R/\delta\theta$ = 15 at the angle of incidence θ from 8.5 to 9.5 deg deduced the reflectivity sensitivity S_{Rb} = 1380 RIU^{-1}.

7.2.3 Surface architecture

A grating master (sinusoidal relief modulation grating with period of Λ=520 nm and depth of d=58-64 nm) was prepared on a silicon substrate by using a holography (see section 3.2.1.1), and the grating replicas were made by soft lithography (see section 3.2.1.2). A thin gold layer with the thickness of 60 nm was deposited on polymer replica by using magnetron sputtering (see section 3.2.2). Thiol SAM was formed on the gold covered substrate by overnight incubating in a mixture of thiol-COOH (see **3** in Figure 3.8) and thiol-PEG (see **2** in Figure 3.8) dissolved at molar ratio of 1:9 in absolute ethanol (total concentration of 1 mM). Afterwards, the gold surface was rinsed with ethanol and dried in a stream of N_2. The capture antibody (MAF05-627) was immobilized on the sensor surface by EDC/NHS coupling as described previously. The reflectivity spectra before and after the immobilization of antibodies are presented in Figure 7.1. The resonant angle shifts ($\Delta\theta$=0.35 deg) indicated the surface coverage of antibody $\Delta\Gamma_{ab}$ =1.75 ng mm^{-2} (i.e. 0.012 pmol mm^{-2}) as estimated according to equation (2.45), where the penetration depth L_{pd} = 180 nm. The affinity binding constants between βhCG and capture antibody were determined by fitting the association and dissociation binding kinetics of βhCG to sensor surface.

7.2.4 Modification of magnetic nanoparticles with antibodies

MNPs were modified with the βhCG detection antibodies according to the protocol specified in section 3.4.2. The antibody-to-MNP ratio was estimated as 10:1, assuming 90% of antibodies were immobilized on the MNPs surface during the labeling process[23].

7.2.5 Detection formats

As illustrated in Figure 7.2, five different detection formats were investigated. In direct detection format **a**, βhCG was flowed over the sensor surface for 15 min followed by 3-min rinsing with PBST. The sensor response was determined as reflectivity change ΔR before and after the βhCG binding. In detection formats **b**, **c** and **d**, the sensor surface was afterwards incubated with the detection antibody (67 nM in PBST) (format **b**) or MNP-antibodies (MNP-abs, 0.6 nM) (format **c** and **d**) for 10 min, respectively. In detection format **c**, the magnetic field gradient was $\nabla B = 0$. In detection format **d**, the gradient magnetic field $\nabla B = 0.10$ T mm^{-1} was applied during the 10-min incubation of MNP-abs. In the detection format **e**, MNP-abs were preincubated with βhCG for 20 min, followed by 10-min flow of the mixture over the sensor surface with magnetic field gradient $\nabla B = 0.10$ T mm^{-1}. After 1-min rinsing with PBST, the magnet was removed from the sensor surface. After the analyte binding, water and 10 mM NaOH were flowed sequentially for around 10 min in order to regenerate the sensor surface. The LOD was determined as the concentration at which the response ΔR is equal to 3 times of the standard deviation of reflectivity signal $3\sigma_R$.

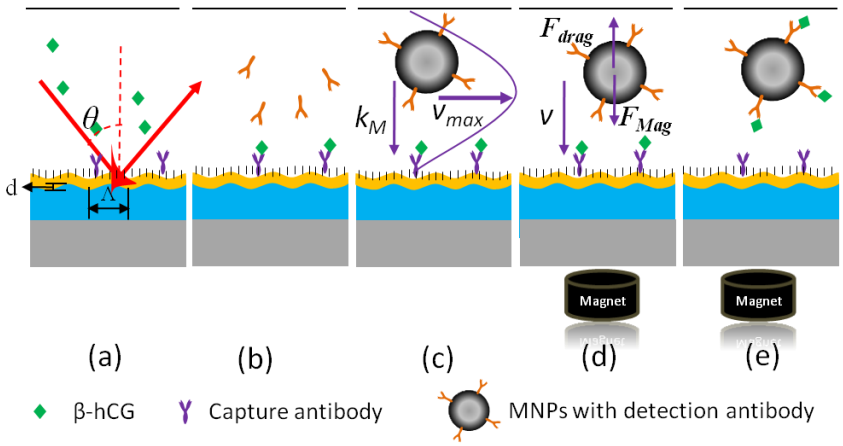

Figure 7.2 Scheme for the detection of βhCG by (a) direct detection, (b) antibody amplification, (c) MNP-antibodies (MNP-abs) amplification without and (d) with applied magnetic field, and (e) the detection of βhCG by incubating MNP-abs with βhCG sample solution prior to the detection.

7.2.6 MNPs and magnetic force

The magnetic force attracting magnetic particles to the sensor surface can be expressed as:

$$F_{Mag} = (1/6)\pi d^3 B_{sat}(\nabla B / \mu_0), \quad (6.1)$$

where, d is the diameter of the MNPs, B_{sat} is the saturation magnetization of the magnetic nanoparticles (B_{sat} = 0.01 T was estimated for used MNPs[16]), ∇B is the magnetic field gradient and μ_0 is the permeability of free space.

The drag force that slows MNPs motion, F_{drag} can be described as follows:

$$F_{drag} = 3\pi\mu dv, \quad (6.2)$$

where, μ is the kinematic viscosity of the solution, and v is the particle velocity in stagnant fluid. Therefore, in a magnetic field gradient ∇B the MNPs reach a steady state velocity equal to:

$$v = F_{Mag} / 3\pi\mu d. \quad (6.3)$$

7.3 Results

7.3.1 Sensor performance

Figure 7.3 shows the kinetics of the SPR reflectivity R upon the analysis of sample with 4.5 nM of βhCG by using detection formats **a**-**d**. At this concentration, reflectivity change of 0.06 was observed for direct detection of βhCG (format **a**). With the binding of detection antibody (format **b**), the reflectivity was changed to 0.18 (see curve i in Figure 7.3), which is 3 times higher than that for detection format **a**. With the MNPs immunoassay (format **c**), the reflectivity change was increased up to 1.02 (curve ii in Figure 7.3), indicating an enhancement by a factor of 17 with respect to detection format **a**. In addition, the immunoassay with magnetically driven MNPs (format **d**) leads to reflectivity change of 7 (as shown in curve iii in Figure 7.3), which is ~2 orders of magnitude higher than that for detection format **a**. The angular spectra (Figure 7.4B) for the detection of 45 nM βhCG also showed that the resonant angle shifts 0.45 deg when magnetic field was applied, which is about 5 times higher than that without the magnetic field gradient (curve iii in Figure 7.4B).

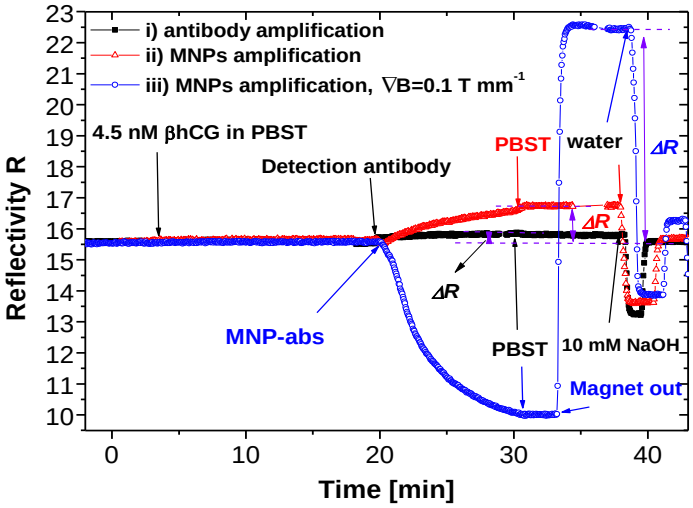

Figure 7.3 Comparison of the time evolution of the sensor signal measured on the sandwich assay for the detection of 4.5 nM βhCG with i) antibody amplification (format **b**), ii) MNP-abs amplification (format **c**) and iii) MNP-abs amplification with magnetic field gradient ∇B= 0.10 T mm^{-1} (format **d**).

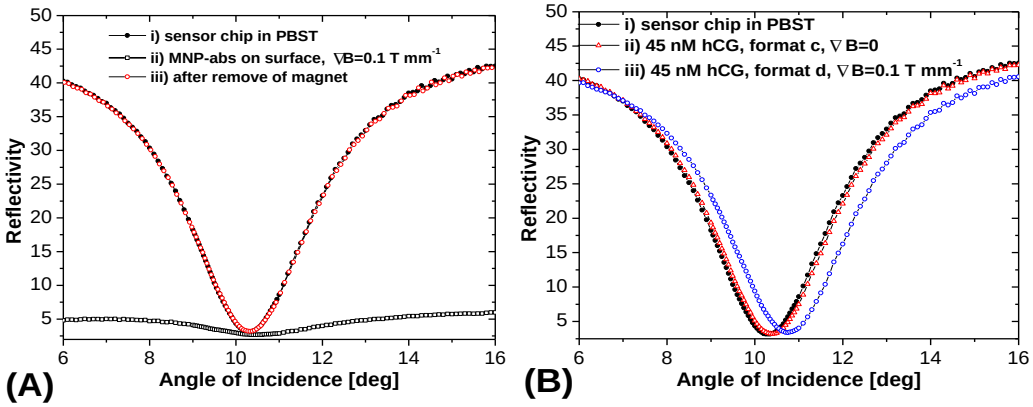

Figure 7.4. (A) Angular reflectivity spectra of (i) a sensor chip immobilized with capture antibodies measured in PBST, (ii) control experiment for the capture of MNP-abs to the sensor surface under magnetic field ∇B = 0.1 T mm^{-1}, measured in PBST (format **d** without βhCG), and (iii) after remove of magnet from the sensor chip, measured in PBST. (B) Angular reflectivity spectra of (i) a sensor sensor chip used for the detection of 45 nM βhCG with MNPs immunoassay by using (ii) format **c** without and (iii) format **d** with magnetic field graident.

7.3.2 Limit of detection (LOD)

The calibration curves for the detection of βhCG are plotted for concentrations of βhCG between 0.45 pM and 45 nM (Figure 7.5). The LOD for the label-free direct detection (**a**) was determined as 6 nM. Through the amplification by detection antibody binding (format **b**), LOD was improved by ~2 orders of magnitude to 45 pM. With MNPs amplification (**c**), the LOD was further decreased to 4.5 pM, around 3 orders of magnitude lower than that for direct detection (**a**). The enhanced mass-transfer of MNPs through applied magnetic field (format **d**) allowed to reach even lower LOD of 450 fM which is ~5 orders of magnitude lower than that for direct detection (**a**). Additionally, we observed that the LOD was ~900 fM for the detection of βhCG with format **e** which is two times higher than that for detection format **d**. The detection times and LODs for detection format **a**-**e** are summarized in Table 7.1.

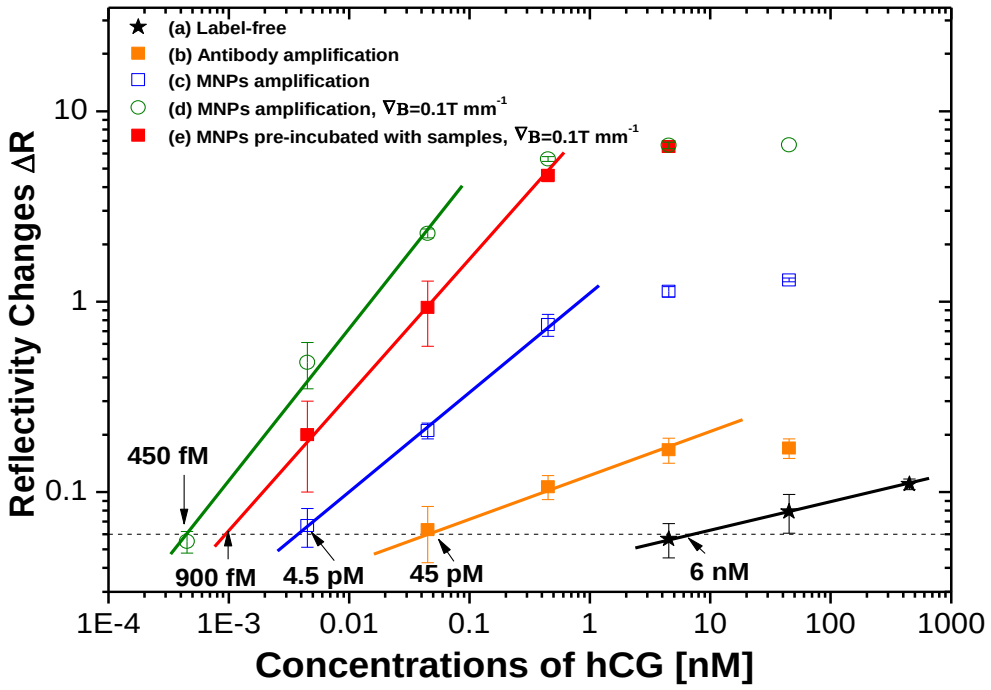

Figure 7.5 The calibration curves for the detection of βhCG by format **a**) label-free direct detection, **b**) antibody amplification, **c**) MNPs immunoassay without and **d**) with external magnetic field, ∇B = 0.1 T mm^{-1}, and format **e**) by incubating MNPs with βhCG prior to the detection with external magnetic field, ∇B=0.1 T mm^{-1}.

Table 7.1 The detection time and LOD for each detection format.

Detection format	βhCG, direct detection, format **a**	Antibody amplified, format **b**	MNP-abs amplified, ∇B=0, format **c**	MNP-abs amplified, ∇B = 0.1 T m^{-1}, format **d**	MNP-abs pre-incubated with βhCG, ∇B = 0.1 T m^{-1}, format **e**
Detection time, min	15	25	25	25	30
LOD	6 nM	45 pM	4.5 pM	450 fM	900 fM

7.4 Discussion

7.4.1 Specificity of sensor surface and surface regeneration

The kinetics measured upon the collecting of MNPs at the sensor surface showed a decreased reflectivity (Figure 7.3iii). This is ascribed to the aggregation of MNPs settled on the sensor surface, and enhanced scattering of light that passes through these aggregates. The measured angular reflectivity for a control experiment confirmed the decreasing of the overall reflected intensity (curve ii in Figure 7.4A). The reflectivity spectrum was measured after the flow of MNP-abs over the sensor surface without captured βhCG. It shows that after the removing of magnet from the sensor surface, the reflectivity spectrum raised back to the original level (curve i and iii in Figure 7.4A), indicating negligible nonspecific absorption of MNP-abs on the sensor surface. The specifically bound MNPs on the sensor surface could be removed (more than 90%) by rinsing the surface with water and 10 mM NaOH (as shown in curves ii and iii in Figure 7.3).

7.4.2 Response enhancement without magnetic field

For the detection of βhCG by using format **b**, we observed the reflectivity response equilibrated after 10-min flow of detection antibody. Thus, we can assume that all βhCG molecules on the sensor surface were bound with detection antibody. The molecular

weight of antibody (M_{ab} = 150 kDa) is around 7 times higher than that of βhCG ($M_{\beta hCG}$ = 22.2 kDa). However, the SPR reflectivity response was increased only by a factor of 3. This can be ascribed to the dissociation of βhCG from the surface during the incubation of detection antibody (according to equation (2.33) 30% of βhCG molecules were remained on the sensor surface after 10-min rinsing). The LOD was decreased by 2 orders of magnitude for detection format **b** compared to that of detection format **a**. This is ascribed to the fact that the slope of calibration curve **a** and **b** is lower than one in the log/log scale (see Figure 7.5) due to the saturation of binding kinetics (k_d=2×10^{-3} s^{-1}, see Table 7.2). For the MNPs-enhanced assay **c**, about 5 times higher SPR signal response was observed compared to that for format **b** due to the higher mass of MNPs.

Table 7.2 The key characteristics of amplified molecules and MNPs.

	βhCG	Antibody	MNP-abs,
M.W., kDa	22.2 kDa	150 kDa	~3 ×10^5 kDa
Diameter, d	4 nm	14 nm	~220 nm
Association rate constant between βhCG and capture antibody	$k_a \cong 5\times10^5$ M^{-1} s^{-1}, $k_d \cong 2\times10^{-3}$ s^{-1}		
Damköhler number (Da)	2.0	4.7	29.5
k_M, mm s^{-1}	4.77×10^{-3}	2.07×10^{-3}	3.3×10^{-4}

7.4.3 Magnetic field enhanced-sensor response

The magnetic field gradient in format **d** enables the response enhancement by a factor of 6, compared to detection format **c** for the detection of high concentration of βhCG (e.g. 4.5 nM). The reason is that a higher amount of MNPs were attracted on the sensor surface in detection format **d** under magnetic field. The velocity of MNPs was estimated as $v_m \cong 2.14\times10^{-3}$ mm s^{-1} according to the equation (6.3), which is 6.5 times higher than the diffusion rate of MNPs, i.e. $k_{m\_MNPs} \cong 3.3\times10^{-4}$ (see Table 7.2). At high concentration of βhCG, we assumed the binding of MNP-abs to the surface was mass-transport limited (Da>>1, see Table 7.2). As the response is proportional to the mass-transfer rate, therefore, the estimated response ratio of 6.5 is consistent with the experiment results.

For the detection of βhCG at low concentration by using detection format **e**, the response was lower than that for detection format **d**. This can be ascribed to the fact that the velocity of MNPs v_m was lower than the diffusion rate of βhCG k_M (see Table 7.2). Therefore, the sensor response and LOD may be improved if larger magnetic moment or higher gradient of magnetic field is applied to capture MNPs on the sensor surface. It also indicates that MNPs immunoassay can offer higher efficiency for the detection of larger analytes with lower diffusion rate such as bacteria.

7.5 Conclusions

We have combined grating-coupled SPR biosensor with magnetic nanoparticles (MNPs) immunoassay. We show that this approach enables actively manipulating with target analyte on the sensor surface through applied gradient magnetic field and advance the sensitivity of SPR biosensors. Particularly, enhancing of refractive index changes associated with analyte capture on the surface and increasing of analyte mass-transfer from a sample to the surface was investigated. The performance characteristics of the sensor were demonstrated by an experiment in which the βhCG was detected by direct and sandwich immunoassay formats. The results show greatly improved sensitivity (by around 5 orders of magnitude) with respect to regular SPR utilizing direct detection format. The achieved limit of detection (0.9 pM) is comparable to that demonstrated by more complex surface plasmon-enhanced fluorescence spectroscopy (0.6 pM)[24] and around 3 order of magnitude better than that for regular SPR with sandwich assay (0.13 nM[25]) and SP-enhanced diffraction detection scheme (0.2 nM[26]). The investigation of the mass-transfer of MNPs-captured analyte that is driven by magnetic field gradient indicates that this approach is particularly suited for detecting of large analytes such as bacterial pathogens that diffuse slow to the surface. In addition, we believe that grating-coupled SPR with MNPs assays will be advantageous for lateral manipulating with analytes in SPR biosensors with 2-D microarray detection format.

References

1. Knoll, W. (1998). Interfaces and thin films as seen by bound electromagnetic waves, *Annual Review of Physical Chemistry*, **49**, 569-638.
2. Homola, J. (2008). Surface plasmon resonance sensors for detection of chemical and biological species, *Chem.Rev.*, **108**, 462-493.

3. He, L., Musick, M. D., Nicewarner, S. R., Salinas, F. G., Benkovic, S. J., Natan, M. J. and Keating, C. D. (2000). Colloidal Au-enhanced surface plasmon resonance for ultrasensitive detection of DNA hybridization, *J. Am. Chem. Soc.*, **122**, 9071-9077.
4. Lee, H. J., Wark, A. W. and Corn, R. M. (2008). Enhanced bioaffinity sensing using surface plasmons, surface enzyme reactions, nanoparticles and diffraction gratings, *Analyst*, **133**, 596-601.
5. Mitchell, J. S., Wu, Y. Q., Cook, C. J. and Main, L. (2005). Sensitivity enhancement of surface plasmon resonance biosensing of small molecules, *Anal. Biochem.*, **343**, 125-135.
6. Wark, A. W., Lee, H. J., Qavi, A. J. and Corn, R. M. (2007). Nanoparticle-enhanced diffraction gratings for ultrasensitive surface plasmon biosensing, *Anal. Chem.*, **79**, 6697-6701.
7. Frasconi, M., Tortolini, C., Botre, F. and Mazzei, F. (2010). Multifunctional Au Nanoparticle Dendrimer-Based Surface Plasmon Resonance Biosensor and Its Application for Improved Insulin Detection, *Analytical Chemistry*, **82**, 7335-7342.
8. Goodrich, T. T., Lee, H. J. and Corn, R. M. (2004). Direct detection of genomic DNA by enzymatically amplified SPR imaging measurements of RNA microarrays, *J. Am. Chem. Soc.*, **126**, 4086-4087.
9. Lee, H. J., Li, Y., Wark, A. W. and Corn, R. M. (2005). Enzymatically amplified surface plasmon resonance imaging detection of DNA by exonuclease III digestion of DNA microarrays, *Anal Chem*, **77**, 5096-5100.
10. Fang, S. P., Lee, H. J., Wark, A. W. and Corn, R. M. (2006). Attomole microarray detection of MicroRNAs by nanoparticle-amplified SPR imaging measurements of surface polyadenylation reactions, *Journal of the American Chemical Society*, **128**, 14044-14046.
11. Wark, A. W., Lee, H. J., Qavi, A. J. and Corn, R. M. (2007). Nanoparticle-enhanced diffraction gratings for ultrasensitive surface plasmon biosensing, *Analytical Chemistry*, **79**, 6697-6701.
12. Wang, J. L., Munir, A., Zhu, Z. Z. and Zhou, H. S. (2010). Magnetic Nanoparticle Enhanced Surface Plasmon Resonance Sensing and Its Application for the Ultrasensitive Detection of Magnetic Nanoparticle-Enriched Small Molecules, *Analytical Chemistry*, **82**, 6782-6789.
13. Hsing, I. M., Xu, Y. and Zhao, W. T. (2007). Micro- and nano-magnetic particles for applications in biosensing, *Electroanalysis*, **19**, 755-768.
14. Katz, E., Weizmann, Y. and Willner, I. (2005). Magnetoswitchable reactions of DNA monolayers on electrodes: Gating the processes by hydrophobic magnetic nanoparticles, *Journal of the American Chemical Society*, **127**, 9191-9200.
15. Willner, I. and Katz, E. (2003). Magnetic control of electrocatalytic and bioelectrocatalytic processes, *Angewandte Chemie-International Edition*, **42**, 4576-4588.
16. Tseng, P., Di Carlo, D. and Judy, J. W. (2009). Rapid and Dynamic Intracellular Patterning of Cell-Internalized Magnetic Fluorescent Nanoparticles, *Nano Letters*, **9**, 3053-3059.
17. Perez, J. M., Josephson, L., O'Loughlin, T., Hogemann, D. and Weissleder, R. (2002). Magnetic relaxation switches capable of sensing molecular interactions, *Nature Biotechnology*, **20**, 816-820.
18. Perez, J. M., Simeone, F. J., Tsourkas, A., Josephson, L. and Weissleder, R. (2004). Peroxidase substrate nanosensors for MR imaging, *Nano Letters*, **4**, 119-122.
19. Nam, J. M., Thaxton, C. S. and Mirkin, C. A. (2003). Nanoparticle-based bio-bar codes for the ultrasensitive detection of proteins, *Science*, **301**, 1884-1886.
20. Gu, H. W., Ho, P. L., Tsang, K. W. T., Wang, L. and Xu, B. (2003). Using biofunctional magnetic nanoparticles to capture vancomycin-resistant enterococci and other gram-positive bacteria at ultralow concentration, *Journal of the American Chemical Society*, **125**, 15702-15703.
21. Gu, H. W., Ho, P. L., Tsang, K. W. T., Yu, C. W. and Xu, B. (2003). Using biofunctional magnetic nanoparticles to capture Gram-negative bacteria at an ultra-low concentration,

Chemical Communications, 1966-1967.

22. Soelberg, S. D., Stevens, R. C., Limaye, A. P. and Furlong, C. E. (2009). Surface Plasmon Resonance Detection Using Antibody-Linked Magnetic Nanoparticles for Analyte Capture, Purification, Concentration, and Signal Amplification, *Anal. Chem.*, **81**, 2357-2363.
23. Koh, I., Wang, X., Varughese, B., Isaacs, L., Ehrman, S. H. and English, D. S. (2006). Magnetic iron oxide nanoparticles for biorecognition: Evaluation of surface coverage and activity, *Journal of Physical Chemistry B*, **110**, 1553-1558.
24. Vareiro, M. L. M., Liu, J., Knoll, W., Zak, K., Williams, D. and Jenkins, A. T. A. (2005). Surface plasmon fluorescence measurements of human chorionic gonadotrophin: Role of antibody orientation in obtaining enhanced sensitivity and limit of detection, *Analytical Chemistry*, **77**, 2426-2431.
25. Boozer, C., Yu, Q. M., Chen, S. F., Lee, C. Y., Homola, J., Yee, S. S. and Jiang, S. Y. (2003). Surface functionalization for self-referencing surface plasmon resonance (SPR) biosensors by multi-step self-assembly, *Sensors and Actuators B-Chemical*, **90**, 22-30.
26. Yu, F. and Knoll, W. (2004). Immunosensor with self-referencing based on surface plasmon diffraction, *Analytical Chemistry*, **76**, 1971-1975.

Chapter 8 Summary

The key results of this work include the development of new platforms for ultra-sensitive optical biosensors based on long range surface plasmon (LRSP) optics, optimization of hydrogel materials and their modification with recognition elements for large capacity binding matrices, implementation of magnetic nanoparticles for SPR-based sensing and successful applications of developed schemes for detection of biomolecular analytes at as low as femtomolar concentrations. With respect to conventional SPR biosensor technologies, these limit of detection (LOD) are approximately 3-4 orders of magnitude lower. Model as well as realistic samples were analyzed and achieved LOD matched the levels required in specifically chosen challenging applications in the area of medical diagnostics and food control. The results of each of the project are summarized.

An inhibition immunoassay for the detection of aflatoxin M_1 (AFM_1) in milk with the LOD at fM level was developed based on LRSP-enhanced fluorescence spectroscopy (LR-SPFS). The analysis time including sample pre-treatment was lower than one hour. The sensor was shown to be regenerable for more than 30 times. The demonstrated LOD was about two orders of magnitude lower than the maximum residue level required by the European Commission for dairy products. Such highly sensitive devices can be, for instance, used for early detection of rising AFM_1 concentration in milk products prior to it reaches levels for which the whole production has to be discarded.

In order to take advantage of large penetration depth of LRSPs, the previous biosensor platform was combined with a PCMD hydrogel binding matrix that exhibit around micrometer thickness. The binding matrix provided highly open network in which antibody catcher molecules were immobilized with surface mass larger than 45 ng mm^{-2}. This value corresponds to tens of full packed monolayers. The investigation of swelling properties and binding capacity of the PCMD hydrogel film shows that the binding capacity is related to the density of the PCMD hydrogel which is dependent to the amount of crosslinker (i.e. benzophenone groups) and functional groups (carboxylic groups). The measurement of the binding kinetics of f-PSA to the immobilized catcher antibody showed that the target analyte can diffuse fast through the gel and the determined affinity

binding constants were comparable to those obtained for other surface architectures. The nonspecific interaction of the PCMD hydrogel with blood serum was observed. The data revealed that the mass density of nonspecifically adsorbed serum constituents reached relatively high value of 5 ng mm^{-2}. The LRSP-FS with this large binding capacity matrix was applied for detection of f-PSA with the LOD of 34 and 330 fM for buffer and human serum samples.

Hydrogel matrix can serve not only as a binding matrix (as discussed above), but also can be used as an optical waveguide. The probing of hydrogel binding matrix with such guided wave offers the advantage of full overlap of the electromagnetic field with the region where molecular binding events occur. Hydrogel optical waveguide (HOW) layer based on a PNIPAAm hydrogel was deposited on a gold surface for the detection of biomolecules. With respect to regular SPR biosensors with thiol SAM, the spectroscopy of HOW modes was demonstrated to provide an order of magnitude better resolution in the measurement of refractive index changes, and more than one order of magnitude higher binding capacity. The LOD of IgG biomolecules was improved by a lower factor of five due to the effect of diffusion-limited mass transport through the hydrogel film. This new method is expected to be particularly beneficial for detecting of small molecules that diffuse fast and for which the binding-induced refractive index changes are too small to be sensitively detected by regular SPR.

SPR biosensors (similar to other surface-based biosensors) rely on diffusion driven transfer of target analyte from a sample to the surface with immobilized recognition elements. In this thesis, we implemented magnetic nanoparticles (MNPs) assays to SPR biosensor platform by using a setup with diffraction grating coupling to SPs. It offers the advantage of straightforward applying a gradient magnetic field through a sensor chip. This approach was shown to allow for rapid collecting of MNPs on the SPR sensor surface. The results showed that the diffusion–driven mass transfer to the sensor surface was faster than that via used MNPs for molecules with the size lower than 4 nm. In addition, sensitivity of the SPR sensor was advanced through increased binding-induced refractive index changes when MNPs were used as labels. With respect to regular direct SPR detection the sensitivity improvement by 5 orders of magnitude was demonstrated for βhCG assay. The study suggests that presented approach holds potential to improve the detection of particularly large analytes such as bacterial pathogens.

List of Figures

List of Tables

Publication List

1. Wang Y., Dostalek J.*, Knoll W., Magnetic Nanoparticle Enhanced Surface Plasmon Resonance Biosensors: for the Detection of Bacteria. (In preparation)
2. Wang Y., Dostalek J.*****, Knoll W., Magnetic Nanoparticle Enhanced Surface Plasmon Resonance Biosensors: on the Role of Mass Transport and Response Amplifications. (In preparation)
3. Wang Y., Dostalek J.*, Knoll W., Magnetic Nanoparticle-enhanced Surface Plasmon Resonance Biosensor. ***Proc. Eurosensors*** *XXIV*, 2010.
4. Sinner E.K., Ritz S., Wang Y., Dostalek J., Jonas U., Knoll W., Molecular Controlled Functional Architectures. ***Materials Today*** 2010, 13, 46-55.
5. Wang Y., Huang C.J., Jonas U., Wei, T., Dostalek J.*****, Knoll W., Biosensor Based on Hydrogel Optical Waveguide Spectroscopy. ***Biosensors and Bioelectronics*** 2010***,*** 25, 1663-1668.
6. Wang Y., Brunsen A., Jonas U., Dostalek J.*****, Knoll W., Prostate Specific Antigen Biosensor based on Long Range Surface Plasmon-Enhanced Fluorescence Spectroscopy and Dextran Hydrogel Binding Matrix. ***Analytical Chemistry*** 2009, 81, 9625–9632.
7. Wang Y., Dostalek J.*****, Knoll W., Long Range Surface Plasmon-Enhanced Fluorescence Spectroscopy for Detection of Aflatoxin M_1 in Milk. ***Biosensors and Bioelectronics*** 2009, 24, 2264–2267.
8. Knoll W.*****, Kasry A., Yu F., Wang Y., Brunsen A., Dostalek J., New Concepts with Surface Plasmons and Nano-biointerfaces. ***Journal of Nonlinear Optical Physics & Materials*** 2008, 17 (2), 121-129.
9. Wang Y., Qian W.P.*****, Tan Y., Ding S.H., A Label-free Biosensor Based on Gold Nanoshell Monolayers for Monitoring Biomolecular Interactions in Diluted Whole Blood. ***Biosensors and Bioelectronics*** 2008, 23, 1166-1170.
10. Wang Y., Qian W.P.*****, Tan Y., Ding S.H., Zhang H.Q., Direct Electrochemistry and Electroanalysis of Hemoglobin Adsorbed in Self-Assembled Films of Gold Nanoshells. ***Talanta*** 2007, 72, 1134-1140.
11. Wang Y., Tan Y., Ding S.H., Li L., Qian W.P.***,** Fabrication and Characterization of Multishell Structures Based on Au and SiO_2. ***Acta Chimica Sinica*** 2006, 64 (22), 2291-2295.
12. Jing A.H., Tan Y., Wang Y., Ding S.H., Qian W.P.*, Interfacial Construction of Gold Nanoshells on 3-Aminopropyl triethoxysilane (APTES) Modified ITO Electrode Surface for Studying Cytochrome b_{562} Electrochemistry. ***Journal of Nanoscience and Nanotechnology*** 2006, 7, 440-446.
13. Ding S.H., Qian W.P.*****, Tan Y., Wang Y., In-situ Incorporating Gold Nanoparticles with Desired Sizes into Three-dimensionally Macroporous Matrices. ***Langmuir*** 2006, 22, 7105-7108.
14. Tan Y., Qian W.P.***** Ding S.H., Wang Y., Gold-Nanoparticle-Infiltrated Polystyrene Inverse Opals: A Three-Dimensional Platform for Generating Combined Optical Properties. ***Chemistry of Materials*** 2006, 18, 3385-3389.
15. Tan Y., Ding S.H., Wang Y., Jing A.H., Qian W,P.***,** Regenerating optical properties of individual gold nanoparticles in alcoholic solvents without any surfactant. ***Journal of Nanoscience and Nanotechnology*** 2006, 6 (1), 262-264.
16. Tan Y., Ding S.H., Wang Y., Qian W.P.*****. Fabrication of Gold Nanoshells and Their Potential Applications to Biology. ***Acta Chimica Sinica*** 2005, 63: 929-933.

BOOK CHAPTER

1. Wang Y., Huang CJ., Dostalek J., Evanescent Wave Biosensors with Hydrogel Binding Matrix, in ***Biofunctional Surface***. Pan Stanford (In press).

CONFERENCES

1. Wang Y., Dostalek J., Knoll W., Grating-coupled SPR for magnetic nanoparticle immunoassay. ACS, Boston, August 22-26th 2010. **(Poster)**
2. Wang Y., Dostalek J., Knoll W., Immunosensor based on long range-surface Plasmon enhanced fluorescence spectroscopy. *MPIP-IMTEK-JÜLICH*, Ebernburg, May 5-7th 2008. **(Talk)**
3. Wang Y., Dostalek J., Knoll W., Novel biosensors based on long range-surface Plasmon enhanced fluorescence spectroscopy. IMPRS School "Polymer Synthesis", Kloster Kirchberg, April 2-8th 2008. **(Talk)**
4. Wang Y., Dostalek J., Knoll W., Immunosensor based on long range-surface Plasmon enhanced fluorescence spectroscopy for the detection of aflatoxin M_1 in milk. *MPIP Conference*, Naurod, April 24-28th 2008. **(Poster)**
5. Dostalek J., Wang Y., Huang C.J., Chulia-Jordan R., Aulasevich A., Roskamp R., Brunsen A., Knoll W., Advanced biosensing based on surface plasmon-enhanced fluorescence spectroscopy, *Nanosens*, Vienna, September 29-30th 2008, Book of abstracts pp. XX.
6. Dostalek J., Wang Y., Brunsen A., Roskamp R., Knoll W., Biosensor based on long range surface plasmon-enhanced fluorescence spectroscopy, *Europtrode IX*, Dublin, March 30th 2008, Book of abstracts pp. 66.